Università degli Studi di Ferrara

DOTTORATO DI RICERCA IN
FISICA

CICLO XXIV

COORDINATORE Prof. Filippo FRONTERA

DEVELOPMENT OF THE INNOVATIVE LEPECVD REACTOR FOR

EPITAXIAL GROWTH OF SILICON – GERMANIUM HETEROSTRUCTURES

Settore Scientifico Disciplinare FIS/01

Dottorando
Dott. GUALDI Federico

_____
(firma)

Tutore
Prof. GUIDI Vincenzo

_____
(firma)

Anni 2009/2011

Abstract

The semiconductor materials both in the form of heteropitaxial and homoepitaxial structures, offer huge potentialities due to a large variety of band energy structures which can be exploited in microelectronics (FET, HBTs) and optoeletronic (lasers, LEDs) devices. However, epitaxial integration of different semiconductors for device development present several issues regarding mainly the minimization of the defects within the heterostructures. To achieve this, materials with similar lattice constant should be used, so that the induced elastic strain in the overgrown film is minimized. Other than the physical constraints however, the choice of the high quality substrate must yield to a cost-effective solution to develop the devices. In the field of microelectronics, the silicon has remained the unparallel material of choice for complementary metal-oxide-semiconductor (CMOS) devices due to its large availability and relative low cost of the raw material. Born in the late 1950s and having since grown into an industry with annual revenues currently in excess of $200 bilion, the modern Si-based semiconductor microelectronics industry is an amazing technical and financial accomplishment. The continuous increase in devices performance requirements have highlighted the main limitation of the silicon device employment. The carrier mobility for both electrons and holes is relatively small respect to the III V alloys, which instead combine high electrical performance with equally high radiation interaction efficiency. Furthermore, the maximum velocity that these carriers can attain under high electric fields is also small, and this limits the cut off frequency of the Si-based microelectronic devices. Due to indirect bandgap also, light emission and absorption is fairly inefficient, making impractical its employment in optoelectronics devices. On the other hand, the higher physical and electrical properties of the III V alloys respect to silicon, are also coupled with relatively high costs. Furthermore, these compounds offer an high application flexibility as the relative composition of these alloys can be also tuned in order to obtain a specific optical or electrical properties.

By employment of the Germanium however, the properties of the silicon can be enhanced drastically. SiGe compounds infact exhibit higher electron and hole mobility even if small relative Ge fraction is added to the silicon. Moreover, the application of strain engineering in microelectronic devices using strain-relaxed SiGe buffer layer have brought a drastic enhancement in electrical properties of silicon. These alloys offers in addition the possibility to integrate the high efficiency III V alloys with low cost silicon substrate. The generally large lattice mismatch between these materials and the silicon, give rise to several issue regarding epitaxy integration. High mismatched heterostructure infact, relax plastically the elastic strain by an uncontrollable process which lead to a high density of induced defects in the grown layers. Several methods have been developed to growth high quality Ge layers

onto silicon substrate with only a small dislocation content, such as constant composition thin buffer layers, linearly graded buffer layer and terrace graded buffer layers. On the other hand, in case a pure Ge can be directly integrated into the silicon wafer, a subsequent overgrown of III V alloys can be performed generating a low density of induced dislocations. Also the technique employed for deposition play a determinant role on the final quality of the grown layer. Classical CVD techniques, are able to growth high quality epitaxial layers but suffers generally of a low growth rate. Furthermore, the high thermal budgets required for precursor cracking can lead to several defect generation processes which finally degrade the electrical properties of the grown layer.

In this work, high quality pure Ge virtual substrate (VS) have been grown onto silicon substrate using the low energy plasma enhance chemical vapor deposition (LEPECVD) technique. The innovative epitaxial reactor have been developed at the Physics Department of the University of Ferrara in collaboration with Dichroic Cell, and have been installed in the clean room facilities. A very high growth rates, as high as 3 nm/s, can be obtain while maintaining an high crystallographic quality of the epilayers. Furthermore, the substrate temperature have been proved to play a determinant role on the epitaxial processes. Thus a numerical approach have been developed to assess the temperature profile during the epitaxial process within the LEPECVD reactor. The finite element analysis have highlighted several feature useful for the design improvement of the LEPECVD heating stage. Finally, pure Ge VS buffer layers have been obtain with a induced TDD as low as 10^5 cm^{-2}. The low surface roughness and the high relaxation of the VS buffer layers obtained, put the basis for a cost-effective integration of the high efficient III-V alloys with Silicon substrates.

Abstract

I materiali semiconduttori sia sotto forma di strutture omoepitassiali e eteropitassiali, offrono enormi potenzialità grazie alla grande varietà di propietà elettriche e fisiche, che possono essere sfruttate per lo sviluppo di dispositivi microelettronici (FET, HBTs) e optoelettronici (laser, LED). Tuttavia, l'integrazione epitassiale di differenti materiali presenta diversi aspetti critici riguardanti soprattutto la minimizzazione dei difetti cristallografici. Per ottenere questo, l'integrazione epitassiale dovrebbe riguardare l'utilizzo di substrati con costante reticolare simile a quello dello strato epitassiale, in modo tale che la deformazione elastica indotta nel film risulti minimizzata. Oltre ai vincoli fisici tuttavia, la scelta del substrato di alta qualità deve inoltre tenere conto del costo complessivo. Nel campo della microelettronica, il silicio è rimasto il materiale fondamentale per lo sviluppo di dispositivi CMOS grazie alla elevata disponibilità di materiale grezzo in natura e al basso costo della materia prima. La moderna industria microelettronica basata sul Silicio è nata alla fine degli anni '50 ed è cresciuta nel corso degli anni fino a diventare un settore con un fatturato annuo di 200 bilioni di dollari. Il continuo aumento della richiesta di prestazioni dei dispositivi elettronici ha però messo in evidenza i principali limiti del silicio. La mobilità degli elettroni e delle lacune è decisamente bassa rispetto alle leghe V III, le quali invece combinano elevate prestazioni elettriche ad un'alta efficienza di interazione con la radiazione visibile. Inoltre, la velocità massima di trasporto dei portatori raggiungibile in caso di alti campi elettrici nel silicio è relativamente bassa, e questo limita la massima frequenza di lavoro dei dispositivi microelettronici basati su questa tecnologia. A causa della bandgap indiretta, l'emissione e l'assorbimento di radiazione risulta inefficiente, rendendo impraticabile il suo impiego per dispositivi optoelettronici. D'altra parte, le proprietà fisiche ed elettrica delle leghe III V rispetto al silicio, sono anche legate ai costi relativamente elevati di questi materiali. Questi composti offrono una elevata flessibilità applicazione dato che le propietà ottiche e di trasporto elettrico possono essere variate modulando le composizione della lega stessa.

Con impiego del Germanio tuttavia, le proprietà del silicio possono essere migliorate drasticamente. In più, i composti basati su leghe Silicio-Germanio mostrano propietà fisiche ed elettriche decisamente superiori al semplice silicio, e questo risulta valido anche per composti in cui la concentrazione di Ge risulta relativamente bassa. Queste leghe possono essere anche impiegate come substrati vistuali (VS) al di sopra dei quali vengono depositati sottili strati in silicio. Allora lo strato in silicio subisce uno stress elestico tensile proporzionale alla concentrazione di germanio nello strato. Leghe in Silicio-Germaniuo offrono inoltre la possibilità di integrare composti del III V gruppo con substrati in silicio a basso costo. Il mismatch reticolare in genere elevato tra questi materiali e il silicio, danno luogo ad un rilassamento plastico incontrollato in quale genera un'alta densità di difetti all'interno dello strato.

Diversi metodi sono stati sviluppati per l'integrazione di strati di alta qualità in Ge cresciti sul substrato di silicio in cui siano presente una bassa densità di dislocazioni, come ad esempio sottili strati a composizione costante, strati graded, ovvero in cui la concentrazione di Ge varia linearmente nello strato, e strati buffer con variazioni non lineare di Ge. D'altra parte, l'integrazione diretta di strati in Ge può essere direttamente su substrati di silicio, può porre le basi per una successiva integrazione dei composti III V con substrati in Silicio. Anche la tecnica usata per la deposizione gioca un ruolo determinante sulla qualità finale dello strato. Le classiche tecniche di deposizione CVD, sono in grado di crescere strati epitassiali di alta qualità ma con un tasso di crescita in effetti molto basso. Inoltre, l'elevate temperature del substrato richieste per la scissione delle molecole dei precursori causano l'insorgere di difetti o fratture nello strato epitassiale, dovuti ad esempio ai differenti valori del coefficiente di espansione termica fra germanio e silicio, riducendo le performance elettriche dello strato epitassiale.

In questo lavoro, substrati virtuali (VS) in Ge puro sono state cresciuti epitassialmente su substrati di silicio utilizzando la tecnica deposizione chimica da fase vapore mediante plasma a bassa energia (LEPECVD). L'innovativo reattore epitassiale è stato sviluppato presso il Dipartimento di Fisica dell'Università di Ferrara in collaborazione con Dichroic Cell s.r.l., ed installato presso le Camere Pulite del dipartimento di Fisica. I tassi di crescita degli strati epitassiali cresciuti tramite il reattore LEPECVD superano 3 nm/s, mantenendo nel contempo un'elevata qualità cristallina. La temperatura del substrato gioca un ruolo determinante nei processi epitassiali, modificando ad esempio la mobilità delle specie atomiche adsorbite sulla superficie del wafer. E' stato quindi sviluppato un approccio numerico ad elementi finiti per valutare il profilo di temperatura del substrato e degli altri componenti all'interno del reattore LEPECVD coinvolti durante il processo di deposizione epitassiale. L'analisi agli elementi finiti ha messo in evidenza vari punti critici nell'attuale sistema di riscaldamento radiativo dei substrati per cui è necessario intervenire. Infine, tramite crescita epitassiale LEPECVD sono stati ottenuti substrati virtuali in Ge la cui densità di dislocazioni superficiale (TDD) ha un valore inferiore a 10^5 cm^{-2}. La bassa rugosità e l'alto grado di rilassamento degli strati cresciuti pongono le basi per una efficace integrazione delle III-V leghe ad alte efficienza con i substrati di silicio.

Acknowledgments

I would like to thank first dott. Donato Vincenzi, whose expertise, patience and understanding added considerably to my experience in Ferrara. I would like to thank also prof. Vincenzo Guidi for providing guidance and support through these years. A special thank to ing. Carlo Ferrigno and Federico Allamprese Manes Rossi of *Dichroic Cell S.r.l.* for giving me the chance to work on the LEPECVD reactor and providing support during the preparation of this work.

A special thanks also to the prof. Alberto Quaranta and dott. Francesco Roca for their patience and support during the thesis review process.

A special thanks to all the co-workers Matteo, Luana, Ilaria, Gabriele and to Stefano and his life lessons, for the support and help especially during the last period. I would like also to thank prof. Antonio Parretta for all the suggestions, the assistance and interesting debates.

I want to express my gratitude to my family for all the support they give me during my entire life, especially through these years in Ferrara. I want to express my deepest gratitude to Lisa who literally support and encourage me during the preparation of this work. Without her effort, love and editing support, I would have not finished this thesis.

The research activity has been founded by Dichroic Cell S.r.l., EU project APOLLON (grant agreement n. 213514), and FIRB national project Fotoenergia (RBIP06N57B).

Contents

CHAPTER 1
Introduction

1.1 Ge virtual substrate (VSs)

The heteropitaxy of highly mismatched structures involve many physical aspects which influence the growth mode of the epilayer. The different surface energies between the film and the substrate mainly determines the behavior of the growing film mode. The presence also of the elastic strain inducted by the lattice mismatch f and the kinetic processes involved during non-equilibrium epitaxial growth, cause the growth to deviate from ideal equilibrium conditions. In case of Ge/Si heteroepitaxy, the difference in thermal expansion coefficient α_T between Silicon (2.6 x 10^{-6} $°C^{-1}$) and Germanium (5.8 x 10^{-6} $°C^{-1}$) cause the wafer to bend and eventually cracks within the epilayer which can compromise the subsequent overgrowth of electronic devices onto the layer surface. This effect in particular is enhanced in thermally driven CVD epitaxial processes, in which high growth temperature are require in order to overcome the activation energy for precursor scission. Thus development of low temperature epitaxial processes are mandatory, in order to suppress temperature effects and kinetic growth processes and thereby obtain high-quality strain-relaxed epilayers with abrupt interfaces. The high effort in controlling the epi-growth of highly mismatched superlattice structures is justified by the huge potentiality which these structures can offer.

In the field of Silicon – Germanium compounds, one of these potential implications is represented by the creation of high-quality strain-relaxed intermediated Ge layers buffer which can accommodates the lattice mismatch between the underlying silicon substrate and the final epitaxial layer. The idea is to concentrate the MD consequent to plastic strain

relaxation within the intermediate Ge epilayer, while suppressing the TDD at the surface. The goal is thus to create a buffer layer which exhibit structural properties closer to a bulk material, acting thus a virtual substrate (VS) for the subsequent film overgrowth. In the last few years. strain-relaxed $Si_{1-x}Ge_x$ VS have been employed into strain-engineered microelectronic devices (HFET, BiCMOS) in order to enhance the electrical transport properties of Si. The most important application for pure Ge VS is represented by a cost-effective integration of III-V alloys with silicon substrate. In the optoelectronics field this would allows for example the integration of complex optoelectronic devices onto single silicon chip enabling system-to-system communication. In the work of Liu *et al.* [1.1] a InAs/GaAs quantum dot laser diode grown monolithically onto a Ge VS, shows performances closer an equivalent homoepitaxial laser diode. On the other hand, this can enable the integration of high-efficient III-V concentrator solar cell using low-cost silicon substrate for low-end application.

To be effective, the intermediate layer should exhibits several structural properties which can ensure high-quality film overgrowth. First, the buffer VS must be ideally fully strain-relaxed in order to match as closely as possible the lattice spacing of the overgrown film and avoid elastic strain which would eventually result in either plastic relaxation or surface corrugation. Furthermore, the TDD at the surface must be as low as possible in order to avoid the worsening effect of TD minority carrier recombination on the electrical performance of the device. The electrical transport properties of overgrown GaAs film onto Ge substrate are not sensibly influenced below a threshold value which is a function of dopant concentration of the GaAs layer and generally has a value in the range 10^4 – 10^5 cm^{-2}. Finally, the VS buffer film should exhibit low surface roughness in order to achieve abrupt interface between the buffer layer and the overgrown film. Contrarily, the electron scattering and recombination at the interface can reduce the electrical performances of the overgrown device.

In this work, Ge virtual substrate have been grown onto Silicon wafer using the innovative reactor LEPECVD, which has been developed at the University of Ferrara in collaboration with Dichroic cell S.r.l. Several technical advantages have been exploited in order to obtain high quality intermediate Ge buffer layer with a cost effective solution. Contrarily to other epitaxial techniques, the low energy plasma enhanced CVD reactor shows a high growth rate independent from the temperature of the substrate while maintaining a high uniformity and high crystal quality of the epilayer.

1.2 Organization of the thesis

The reminder of this dissertation is organized as follow. In Chapter 2 the most important aspects of the SiGe and Ge heteroepitaxy are reviewed. In Chapter 3 are discussed the main aspects of the plasma deposition process are reviewed. Since the critical aspect of the substrate temperature play a determinant role during epitaxial process, in Chapter 4 are discussed the main aspects of the radiative heating of the wafers, and a theoretical approach to the radiative modeling of silicon wafer have been followed. Finally, in Chapter 5 and 6 are discussed respectively the results of the numerical approach developed in order to improve the LEPECVD heating stage and the results of deposition processes of Ge virtual substrates.

Reference

[1.1]] Y. Chen, J.W. MacKay, *Phil. Mag.,* **vol.** 19 (1969), p. 357

CHAPTER 2
Silicon – Germanium epitaxy

2.1 $Si_{1-x}Ge_x$/Si heterostructures

Silicon and Germanium are completely miscible for any concentration value. The product is a $Si_{1-x}Ge_x$ alloy which have the same zincblende crystalline structure of the two components, but with a lattice constant a_{SiGe} that monolitically increasing from that of Silicon ($a_{Si} = 0.5431$ nm) to that of Germanium ($a_{Ge} = 0.56575$ nm). The lattice constant of Ge is 4.18 % larger than that of Si, and for $Si_{1-x}Ge_x$ alloys it does not exactly follow the linear approximation of the Vegard's law. The relative change of the lattice constant as a function of the atomic Ge content x is given by [2.1]

$$a_{SiGe} = (0.00501x^2 + 0.03675x)a_{Si} + a_{Si} \tag{2.0}$$

while the application of Vegard's law overestimate the lattice parameter up to 12% for low x contents [2.2]. Due to larger lattice constant, a $Si_{1-x}Ge_x$ layer with $x > 0$ grown onto a silicon substrate experiences a compressive stress which depends both on the mismatch between the two lattice constants and the thickness t_s of the layer. In this conditions the film structure is *pseudomorphic*, i.e. with the in-plane lattice constant $a_{||}$ of the film fitted to that of the substrate by a biaxial film stress which results in a tetragonal distortion of the cubic lattice cell of the film along the direction perpendicular to interface. Pseudomorphic film are also called *strained film* or *coherent films.* Supposing an isotropic properties of the substrate surface, the strain components ε of the pseudomorphic film can be expressed as

$$\varepsilon_{||} = \varepsilon = -f = -\frac{a_l - a_s}{a_s} \tag{2.1}$$

$$\varepsilon_z = -\varepsilon \frac{2\nu}{1-\nu} \tag{2.2}$$

where f is the lattice mismatch between the layer and the substrate, and ν is the Poisson's number which varies between the value for pure Ge $\nu_{Ge} = 0.273$ and that for pure Si $\nu_{Si} = 0.28$. The main challenge in the optimization of the epitaxial process of $Si_{1-x}Ge_x$ alloys, especially in high Ge content layers, is represented by the non-linear increasing of the energy content of highly strained films. The energy E_h of a homogeneous strained pseudomorphic film can be infact expressed as

$$E_h = 2\mu \frac{1+\nu}{1-\nu} t_s \varepsilon^2 \tag{2.3}$$

where μ is the shear modulus expressed in energy per unit square. Thus a pure pseudomorphic Ge film delivers 100 times the energy compared to a 10% Ge content $Si_{1-x}Ge_x$ films. Upon a critical thickness $\bar{t}_s$, the strain energy reaches a valued for which it become energetically convenient to release the strain plastically through the formation of misfit dislocations (MDs) which reduce the in-plane stress. For zinblende and diamond crystalline structure materials, the strain is relaxed by the generation of a 60° MD dislocation in the (110) direction and a threading dislocation (TD) arms which extent along the (111) glide plane up to the film free surface, which is schematically show in Fig. (2.1). The orientation of the Burger vector for TDs indicates that while the TD itself does not relieve strain, TD glide and lengthening of the MD segment at the interface does provide strain relaxation. The relaxation degree R of the layer defined as the reduction of the in-plane stress can be expressed for a network of MDs with parallel line vectors as

$$R = 1 - \left(\frac{-\varepsilon}{f}\right) = \frac{b'}{pf} \tag{2.4}$$

where b' is the effective Burger vector length, which in a typical Si(100) surface with 60° dislocations in (111) glide planes results $b' = b/2$, and p is the mean MD distance. The parameter value ranges from $R = 1$ for complete relaxed layer to $R = 0$ for pseudomorphic layers ($1/p \to 0$) and results directly proportional to the sum of the MD length at the interface. The value of residue elastic strain results infact approximately the

same in layers with a high density of sessile 'short' MDs and layers with a low density of extended MDs [2.3]. Obviously, the threading dislocation density (TDD) is lower in the second case. The relaxation process also depends strictly both by the epitaxial deposition processing and the lattice mismatch. Direct epitaxy of large mismatched systems, such as $Si_{1-x}Ge_x$/Si with a high Ge content, results in uncontrolled lattice relaxation, such as three-dimensional growth and the introduction of large number of immobile MD and TDs. The results is a near completely relaxed film containing TD density (TDDs) of greater than 10^9 cm^{-2} [2.4]. However, for lower mismatch systems ($f <$ 1-1.5%), the incorporation of strain is more controlled and predominately results in the formation of 60° misfit dislocations at the interface and the associated TDs [2.5, 2.6].

2.1.1 TDD influence on layer electrical performance

The high effort toward obtain relaxed epitaxial heterostructures with low TDD is due to their strong influence on the electrical performance of the grown layer. Since the TD penetrate the epitaxially grown device layer, it acts as a site of localized recombination for the free-carrier reducing the minority carrier diffusion length and minority carrier lifetime. The reduction in the diffusion length and carrier lifetime as a function of the TDD can be calculated using the work of Yamaguchi *et al.* [2.7], in which it is evaluated the influence of the TDD on the single-crystal thin-films AlGaAs/GaAs/Si double heterostructures (DHs) solar cells performances. First, the process of carrier diffusion toward the TD can be expressed using the differential diffusion equation for the carrier concentration $n(x,t)$. The diffusion coefficient D is related to the minority carrier mobility using the Einstein relation

$$\frac{D}{\mu} = \frac{kT}{q} \tag{2.5}$$

where k is the Boltzmann constant and q is the carrier electrical charge. It is also assumed that the single TD has an occupation volume given by $\pi x_c^2 = (TDD)^{-1}$, where x_c represents the radius at which the TD have influence on the carrier concentration. Within this radius also, it is also assumed a zero carrier concentration, i.e. no spatial concentration gradient is present from the centre of the dislocation to the radius x_c. Finally, the carrier concentration at distance x_c is assumed being independent from the time and has a value of n_0 . Using these approximations, the differential equation of

diffusion can be solved by means of the separation of variable and the resulting excess minority carrier concentration can be expressed as

$$n(x,t) = n_0 \sin(x/L_{TDD}) e^{-t/\tau_{TDD}} \tag{2.6}$$

$$L_{TDD} = \frac{2x_c}{\pi} = \frac{2}{\pi^{3/2}(TDD)^{1/2}} \tag{2.7}$$

$$\tau_{TDD} = \frac{L_{TDD}^2}{D} = \frac{4}{\pi^3 D(TDD)} \tag{2.8}$$

Since they are characteristic values, it is possible to express the total diffusion length and lifetime including the maximum values L_{max} and τ_{max} for a particular semiconductor material at a given doping concentration from all other contribution (Shockley-Read-Hall, Auger, band-band, etc.) in absence of TDs

$$\frac{1}{L^2} = \frac{1}{L_{max}^2} + \frac{1}{L_{TDD}^2} \tag{2.9}$$

$$\frac{1}{\tau} = \frac{1}{\tau_{max}} + \frac{1}{\tau_{TDD}} \tag{2.10}$$

Based on this model, a decrease in τ and L is expected with increasing the TDD. In Fig.(2.2) are presented the calculated carrier diffusion length and lifetime for different diffusion constant of pure Germanium and GaAs as a function of the TDD dislocation density. The calculation have been performed assuming a minority carrier lifetime value $\tau_{max,Ge} = 2.5$ x 10^{-3} s^{-1} and $\tau_{max,GaAs} = 5$ x 10^{-9} s^{-1} [2.67], a minority electron mobility $\mu_{Ge} = 3.9$ x 10^3 $cm^2V^{-1}s^{-1}$ (i.e. dopant concentration 2x10^{15} cm^{-3} at 300 K) [2.68] and $\mu_{GaAs} = 7450$ $cm^2V^{-1}s^{-1}$ (i.e. dopant concentration 3x10^{15} cm^{-3} at 300K). As expected, the both the minority carrier lifetime diminishes as the TDD increase following an exponential behavior. Within the TDD range of 10^4 – 10^7 cm^{-2}, the Ge minority carrier lifetime is strongly influenced by the TDD, experiencing a drastic reduction of the τ_{Ge} value from about 100 ns to 0.1 ns. Within the same TDD range instead, the GaAs carrier lifetime τ_{GaAs} reaches an asymptotic value for TDD lower than about 10^5 cm^{-2}, which means that the electrical properties of GaAs epilayers with a TDD lower than the threshold value are not influenced by the presence of dislocations. Below that TDD limits, the electrical properties of a heteropitaxial GaAs layer can be thus assumed equivalent to that of bulk GaAs. In the field of concentrator photovoltaics (CPV) solar cells for example, a strain-relaxed Ge virtual substrate with low TDD can be thus in principle to integrate high efficiency III-V alloys with low-cost silicon substrate. A DH GaAs/SiGe/Si solar cell have been developed with a TDD of a about 10^6 cm^{-2}, in which the GaAs

layer is grown onto a strain-relaxed graded SiGe virtual substrate (VS) layer [2.69]. In this work is infact proved that a suppression of the TDD in the GaAs layer below the threshold value can lead the solar cell performances to approach closely to these of homoepitaxial GaAs solar cells.

2.2 Critical thickness

2.2.1 Equilibrium theoretical formulations

The growth of coherent tin layers on the rigid crystalline substrate is possible when biaxial compressive or tensile strain in the layer accommodates the lattice mismatch between the film and the substrate material. When the stored strain energy exceed a certain threshold, the heterostructures become metastable and the film strain may give way to MDs. Various theoretical approach have been developed in order to predict the critical thickness $\bar{t}_s$ as a function of the lattice mismatch and most of them are derived at equilibrium conditions [2.8]. The model developed by Matthews and Blakeslee [2.9, 2.10] is the most often used theoretical approach for critical thickness calculation of heteropitaxy structures. Here it is considered that a preexisting TD in the substrate replicates in the growing epilayer and can bend over to create a length of a MD in the interface once the critical thickness is reached. As the growth of the layer proceed, the dislocation line tension increase and the same does contemporary the resolved force on the glide plane. Thus, the critical thickness is derived by equating the two opposite force and solving for the layer thickness

$$\bar{t}_s = \frac{b(1-\nu\cos^2\alpha)[\ln(\bar{t}_s/b)+1]}{8\pi|f|(1+\nu)\cos\lambda} \tag{2.11}$$

where b is the Burger vector, α is the angle between the Burger vector and the line vector for the dislocations and λ is the the angle between the Burger vector and the line in the interface plane that is perpendicular to the intersection of the glide plane with the interface. Applied to the $Si_{1-x}Ge_x$/Si heteropitaxy, it is assumed $\cos\lambda = \cos\alpha = 1/2$ and $b = a_{SiGe}/2 < 110 >$ which correspond to 60° dislocations with (111) glide systems. For a $Si_{0.9}Ge_{0.1}$ epilayer grown onto a silicon substrate, Eq. (2.11) delivers a critical thickness $\bar{t}_s = 21$ nm, which is high enough to allow SiGe base layer in an HBT. In Fig. (2.4) are summarized the calculation results for the SiGe/Si (100) superlattice obtained by Eq.

(2.11) and two other equilibrium models developed by People and Bean [2.11] and van der Merwe [2.12] which are briefly presented below, compared to experimental data retrieved from SiGe/Si (100) heteropitaxy from different works [2.13, 2.14]. The Matthews-Blakeslee model is in good agreement with the most reliable experimental results. The experiments however present a small scattering and some of the results agree with the People and Bean model. This last and the van der Merwe models derived the critical thickness value by comparing the energy gained from a epilayer expressed by Eq. (2.3), and the energy of a dense network of MDs at the interface, differing each other by the assumption of the mean distance between the MDs. Both assumption made are however not physical. In the People and Bean model for example, is assumed a MD spacing of $2\sqrt{2}a$ which corresponds to a fully relaxed layer of $|f| \approx 0.067$ and so this model should overestimate the $\bar{t}_s$ value for heteropitaxial systems with a mismatch less than 6.7%. Thus the agreement of this model with some experimental results can be addressed to the finite experimental resolution, which cause an overestimation of the critical thickness value due to onset sluggish lattice relaxation [2.8].

2.2.2 Experimental evidences

Otherwise, the pioneer works of Kasper [2.15] and Bean [2.16] in the field of SiGe systems, shows that under some growth conditions strain in the films above a critical thickness predicted by equilibrium theories is not measurably relieved. They can prove infact with molecular beam epitaxy (MBE) at rather low temperatures of about 550°C, that the experimentally obtained value of the critical thickness are far larger than the equilibrium ones. Only above a second critical thickness does measurable relief occur and even then, the amount of relief is not in accord with the equilibrium theory. They undergo a transition from brittle material at room temperature to a ductile material at temperatures higher than 900°C. At these high temperatures it is possible to find the equilibrium values but at lower values with increasing of brittleness of the material the onset of plastic deformation shift to higher thickness because of kinetic limitations to dislocation nucleation and movement [2.21]. The *metastable* regime is roughly limited by an experimentally fitted curve on the values found by several measurements [2.17]

$$\left(\frac{\bar{t}_{s,p}}{b}\right) f = 5x10^{-3} \ln\left(\frac{\bar{t}_{s,p}}{b}\right) \tag{2.12}$$

Even higher critical thickness are possible with growth temperatures below 550°C. This region is called *ultrametastable* regime [2.18]. Metastable layers capped with silicon withstand temperature treatments during device processing and allow the design of SiGe-HBTs with the frequency limits beyond 200 MHz [2.19]. On the other hand, the works of Fritz [2.20] and Dodson and Tsao [2.21] suggests that the observed metastability can be explained by sluggish plastic deformation rates accompanied by a finite experimental resolution and that the second critical thickness is that for which strain relief is just sufficient to be observable. Vogg *et al.* [2.22] report also a slight increase the critical thickness of the $Si_{0.77}Ge_{0.23}$/Si (100) heterostructure by a chemical treatment of the Silicon substrate surface with gaseous HCl at temperature up to 800°C before the CVD deposition process. In Fig.(2.5) are compared the $2\theta/\omega$ XRD scan curves retrieved for different layer thicknesses with and without the pre-process chemical etching. The thickness range have been choose in order to be compared to the equilibrium critical thickness $\bar{t}_{s0}$ for this epitaxial system, i.e. about 170 nm. The non-etched sample start the relaxing process at 178 nm, slight after the predicted equilibrium critical thickness, while the XRD scan for the etched ones shows interference fringes up to 216 nm, which result about 27% larger than the $\bar{t}_{s0}$ value. The presence of the interference fringes in the measured suggest that negligible incoherent scattering due to the presence of MD and TD in the layer have occurred, and thus it can considered as pseudomorphic. Furthermore, the diffuse scattering evaluated with the XRD In particular, the etched 259 nm thick sample show a degree of relaxation which is comparable with that of 174 nm non-etched sample. The evaluation also of the etch pit density on treated sample show a TDD lower than $1.7x10^{-4}$ cm^{-2}, which confirms the retarded relaxation in case the chemical treatment is applied.

2.2.3 Kinetic theoretical formulation

The equilibrium theoretical formulation results described in Section 2.2.1 are thus capable to predict the critical thickness value in heteroepitaxial systems as function of the lattice mismatch, only if the epitaxial deposition is performed at temperatures high enough to activate the dislocation glide processes. However, measured critical thickness for epilayers grown using lower temperatures show that it is possible to obtain metastable heterostructure with thicknesses far larger than the predicted ones. Beanland [2.23] proposes a modified model of the Matthews-Blakeslee approach in which different dislocation generation processes are taken into account. In particular, the Frank-Read and the spiral dislocation multiplication processes, which have been experimentally observed

in $Si_{1-x}Ge_x$/Si system by LeGuoes [2.24] and Capano *et al.* [2.25], are included into the model. In Fig.(2.6) is presented a possible configuration for the Frank-Read source in a heteropitaxial layer. First, a TD pinned between the two point A and B is considered. With applied stress, the dislocation bows out between A and B, until it reaches the free surface of the epilayer. At this point, the bowing loop break into two dislocations and finally the interaction of the two dislocation results in the formation of a half-loop as shown in Fig.(2.6)d. This process leaves the original dislocation intact, and it can participate in further multiplication. For this mechanism, the critical thickness calculation is performed balancing the resolved stress on the pinned dislocation and the dislocation line tension, depending thus by the position of the pinned points and the orientation of the pinned segment. Assuming that the AB pinned segment lies along the <112> direction, the minimum thickness for which the Frank-Read source may operate $\bar{t}_f$ is given by

$$\bar{t}_f = \bar{t}_s + 2\bar{t}_p \tag{2.13}$$

$$\bar{t}_p = \frac{(2+\nu)b}{4\pi|f|(1-\nu)}\left[\ln\left(\frac{4\sqrt{6\bar{t}_p}}{b}\right) + \frac{(\nu-2)}{(\nu+2)}\right] \tag{2.14}$$

where $\bar{t}_s$ is the Matthews-Blakeslee contribution calculated using Eq. (2.11). Similar considerations can be derive for the dislocation spiral multiplication processes. It is assumed that a TD is pinned at a single point A and a stress is applied. In Fig.(2.7) are presented the schematical representations of the spiral multiplication process. With the applied stress, the dislocation may bow out above the pinning point. The bowed section continue to expand and may glide to the interface to relieve the mismatch strain. Further expansion of the bowed portion may lead to production of a half-loop if the bow reaches the surface and split in two as in Fig. (2.7)d. In this case the calculation of the critical thickness have similar expression of Eq. (2.13) but with the $\bar{t}_p$ factor substituted by the $\bar{t}_{sp}$ term, which depends by the height of the pinned point within the epilayer. In Fig. (2.8) are plotted the results using the equations of the two generation contributions. The Frank-Read contribution results in general four to seven times the Matthews-Blakeslee critical thickness values while the spiral source can become active at two to four time the $\bar{t}_s$ term. It is therefore likely that both mechanisms are active in relaxing SiGe/Si heteroepitaxial layers.

On the other hand, Dodson and Tsao [2.21] propose an explanation of extended metastability of SiGe epilayers by means of a strain excess, which is necessary for the film

relaxation. Similar to the Matthews-Blakeslee theoretical approach, a balancing of the force action on the dislocation and the consequent opposite force due to elongation in performed. However in this case, the opposite term has been evaluated as

$$\sigma_D \approx \frac{\mu}{2\pi}\left(\frac{1-\nu\cos^2\beta}{1-\nu}\right)\frac{\ln(4t/b)}{h/b} \tag{2.15}$$

which is balanced with the resolved shear stress σ_M resulting in a excess stress which can be expressed as

$$\sigma_{exc} = 2\mu e\frac{1+\nu}{1-\nu} - \frac{\mu}{2\pi}\left(\frac{1-\nu\cos^2\beta}{1-\nu}\right)\frac{\ln(4t/b)}{h/b} \tag{2.16}$$

which represent the measure of the driving force for strain relief and hence both for the deviation from equilibrium and for the degree of metastability. Thus the experimentally fitted Eq. (2.12) can be explained as a ' isobar ' of excess stress σ_{exc}/μ. So if this excess stress is greater than zero, then there is a net force for dislocation motion. In case is less or equal to zero, there is not net force driving dislocation motion, and the excess stress isobar curve equals the Matthews-Blakeslee curve derived with Eq. (2.11). Even in case of positive stress however, the dislocations do not necessary move freely. On a give experimental time scale, there must be enough excess stress to lead to observable plastic deformation. In Fig.(2.9) are presented the theoretical results of this approach and the measured critical thickness for different samples with increasing lattice mismatch and same growth temperature of 494 °C. In the case of $Si_{1-x}Ge_x/Ge$, the authors identify the $\sigma_{exc}/\mu = 0.026$ as the maximum excess stress for metastability at the 494 °C growth temperature. The transition also from metastability region to the partially relaxed state is well defined by the 'isobar' curve. Furthermore, the excess stress for a particular heteoropitaxial system depends strongly for the temperature of wafer processing. In Fig. (2.10), the excess stress σ_{exc}/μ for the $Si_{1-x}Ge_x/Ge$ have been plotted as a function of the growth temperature. Films grown at temperatures comparable to the 494 °C value, show a critical stress very similar to the $\sigma_{exc}/\mu = 0.026$ value derived earlier, with a definite trend towards higher critical excess stresses at lower temperatures. This trend is consistent with the expectation of generation of sessile MD and TD at lower temperatures, and so they require a greater driving force in order to move at comparable rates. At higher growth temperature instead, films shows a significantly lower σ_{exc}/μ

values, which suggest that a change in the plastic relaxation mechanism have been happened. The plot in Fig.(2.10) can also be used as a deformation-mechanism map [2.26].

2.3 $Si_{1-x}Ge_x$/Si growth modes

In heteroepitaxy deposition processes, an adsorbate material is deposit on the substrate which is a chemically different material. At equilibrium, the stability of the epitaxial layer free surface depends mainly on the balance of the free energies of the surface and interfaces for the substrate and epitaxial layer [2.27]. A planar surface is stable if it minimizes the free energy. Alternatively, the minimization regards the difference between the free-energies of a state with deformed surface and of the with planar surface, and the same mass of adsorbate and substrate. The difference must be positive for all deformations in case the plane surface is to be stable [2.28]. If the elasticity is ignored, the stability condition of a plane interface is given by the well known Young's relation $\bar{\sigma}_{sg} > \bar{\sigma}_{sa} + \bar{\sigma}_{ag}$, where $\bar{\sigma}_{sg}$ is the free energy per surface area at the substrate-gas interface, $\bar{\sigma}_{sa}$ is the free energy per surface area of the substrate-adsorbate interface and $\bar{\sigma}_{ag}$ is the free energy per surface area of the adsorbate-gas interface. During the lattice mismatched epitaxial deposition processes otherwise, the elastic energy and the other processes due to the kinetic altered the equilibrium state causing 3D growth even in case of wetting epitaxial layer. In Fig. (2.11) are schematized the three main typologies in which the epitaxial layer can growth. The 2D Frank van der Merwe (FM) growth on a flat substrate is characterized by the nucleation of successive monolayers which cover the substrate surface. The 3D Volmer-Weber (WB) growth instead involves the development of isolated island on the substrate, followed by their growth and coalescence. Finally, the 2D-3D Stranski-Krastanov (SK) growth, the process proceeds in 2D growth but becomes 3D in nature after the growth of a certain critical layer thickness.

2.3.1 The Asaro-Tiller-Grinfeld (ATG) instability

Once the $Si_{1-x}Ge_x$ epilayers is grown onto the lattice mismatched silicon substrate, the elastic strain energy gained through the deposition process can be release plastically by the introduction of a dislocation or elastically by tetragonal distortion along the direction perpendicular to the interface. However, even if the layer growth is coherent and in equilibrium state, it is found experimentally that the mismatched epitaxial film can stand

the elastic energy by deforming the free surface and thus moving from 2D to 3D growth mode, named ' 2D – 3D transition '. If the misfit is moderate, this deformation leads to alternating hills and valleys, while for stronger misfit as in the case of Ge/Si heterostructure, the adsorbate film split into clusters. The quantitative calculation of the deformation of the epilayer surface at the equilibrium have been developed by Asaro and Tiller [2.29] and later in detailed by Grinfeld [2.30]. In this theoretical approach, the free energy of a sinusoidal modulation of the film surface is evaluated compare to a flatted one. The modulation height of the surface can be described as

$$z(x,y) =< z > +\delta h \cos(qx) \tag{2.17}$$

where $< z >$ is the height in case of flat surface and δh and q the amplitude and phase of the modulation. The terms regarding the free-energy change due to the elastic energy can be expressed as

$$\delta\varphi_{el} = -\frac{q\delta h^2 C_1^2}{4C_2} f^2 E_s \cdot A \tag{2.18}$$

where C_1 and C_2 are two elastic constant of the epilayer, E_s is the Young module of the film and A is the surface area. Thus the elastic free energy change resulting from the sinusoidal deformation is negative. However, the increase of the surface area due to modulation opposes to the elastic free energy gain. This component can be expressed as $\delta\varphi_{sur} = A\tilde{\sigma}\delta h^2 q^2/4$, where the $\tilde{\sigma}$ is coefficient of surface stiffness. By minimizing the total free energy, expressed as the sum of the elastic and surface tension component, it is possible to derive the wavelength λ^* of the surface modulation above which the surface is stable

$$\lambda^* = \frac{2\pi C_2}{C_1^2}\frac{\tilde{\sigma}}{E_s}\frac{1}{f^2} \tag{2.19}$$

The instability of coherent epitaxial films have observed in the growth of pure Ge on Si(111) and [2.31] and and on $Si_{1-x}Ge_x$ on Si (100) systems [2.32], while pure Ge on Si (100) this process lead to split in cluster for thickness larger than three-monolayers [2.33].

2.3.2 $Si_{1-x}Ge_x/Si$ kinetical growth modes

At equilibrium, the growth modes phase diagrams can be derived as function of the lattice mismatch, and in case of SiGe heteroepitaxy systems, as a function of the stechiometric composition of the epilayers. In Fig.(2.12) are presented the phase diagrams for the $Si_{1-x}Ge_x/Si$ systems calculated by Nakajima *et al.* [2.34] in case plastic relaxation by dislocation is either considered or not. The calculations are performed at the equilibrium, and thus it results from the comparisons of the assessed strain, surface and interface energies for the three different growth modes as a function of the Ge content. Since kinetics processes are neglected, the diagrams are derived supposing a ambient temperature of 27 °C as a the temperature increase does not affect significantly both the strain and the free energies [2.34]. From the results it is clear that when the concentration in small, namely under the value $x < 0.5$, the FM mode is dominant up to the maximum calculated value of 8 ML. As the mismatch increases, both the strain and the interface energy increase also and the 3D growth modes are favored. For the pure Ge onto Silicon, the SK growth mode is energetically favored even after 1 ML adsorbed. In case the plastic relaxation is considered, the SK and VW growth modes regions shrink due to a reduction of the strain energy, and thus the FM modes is favored at slight increased mismatch values.

However the conditions experienced in crystal growth by Plasma Enhanced CVD processes are far from being at equilibrium. The most kinetic factors which influence the growth mode and surface morphology are the surface diffusivity and the flux of impinging adatoms. During epitaxy, these two processes can be tuned by modulating the temperature and the growth rate respectively. In addition to that controllable factors, the presence of terraces due to substrate surface off-cut and the Ehrlich-Schwoebel (ES) [2.35] barrier to diffusion step can play a determinant role on the growth mode. Furthermore, the presence of a surfactant can modify the free energy of the surface, promoting thus either 2D or 3D island growth [2.8]. In considering the kinetic parameters in order to obtain a FM or step-flow (SF) growth, Tersoff, Denier van der Gon and Tromp (TDT) [2.36] developed a theoretical model which relate the growth modes to temperature, adatom flux and substrate miscut parameters. In particular, for a given values of temperature and adatom flux, the theoretical approach assess their influence on the island nucleation processes on the substrate surface. After the incoming adatoms are adsorbed on the substrate surface, they can diffuse, re-evaporate or eventually interact

with other adatoms creating clusters. The formed cluster are stable as soon as the critical dimension d_c which minimize the surface energy has been reached [2.8]. From this point, the subsequent adsorbed adatoms which impinge on substrate surface can diffuse and combine with the stable clusters increasing the island dimension, while adatoms which impinge on the top of the first island layer can either surpass the ES barrier or create a new stable cluster. Thus, in case the first monolayer clusters coalesce before new cluster are created on the second monolayer the growth proceed as layer-by-layer. Otherwise, the epilayer growth experiences a kinetic roughening.

Based on an atomistic approach, the model assumes a nucleation rate expressed as $\omega \approx DN_0^2\gamma^i$ where D is the diffusivity for surface atoms, N_0 is the surface atomic density expresses as atoms per unit area, γ is the normalized dimensionless adatom density and i is the number of adatoms by which is composed the critical cluster. Then the differential diffusion equation is evaluated at the first monolayer and upon the fist monolayer island, for which the probability α of overcome the ES barrier at the boundaries is expressed as $\alpha = C_1 \exp(-(E_s - E_d)/kT)$, where C_1 is a constant, E_s is the ES barrier and E_d is the activation energy for surface diffusion on the top of the island. Afterward, it is then possible to calculate the fraction of islands f which have nucleated a second layer on their top by solving a first-order time-differential equation in which the total nucleation rate upon a island, assessed integrating the rate ω over the island surface, is taken into account. The solved expression can be expressed as

$$f = 1 - \exp[(-R/R_c)^m] \tag{2.20}$$

where R is the radius of the island, m is a dimensional parameter which depends on the critical cluster size, and R_c is the critical radius for a second layer nucleation for the transition from FM to SK growth. Two expressions can be derived for the R_c in case the influence of the ES barrier is either neglected or not. The derived expressions can be described as

$$R_{c1} = \left[A_1\left(\frac{2L_n^2}{\pi}\right)\left(\frac{4D}{F}\right)^{i-1} N_0^{i-3}\right]^{A_2} \qquad for\ \alpha \to 0 \tag{2.21}a$$

$$R_{c2} = \left[B_1\left(\frac{2L_n^2}{\pi}\right)\left(\frac{4D}{F}\right)^{i-1} L_\alpha^{-i} N_0^{i-3}\right]^{B_2} \qquad for\ \alpha > 0 \tag{2.21}b$$

where F is the impinging adatoms flux, L_n is the separation between the nucleated islands, L_α is a length that characterized the diffusion barrier at the edge of the islands and A_1, A_2, B_1, B_2 are constants function of i. In Fig.(2.13)a is plotted the Eq. (2.20) as a function of the medium island radius for different values of the m parameter. Essentially, if $R > R_c$ there is an high probability of new nucleation on the islands before they coalescence. This give rise to undesirable surface roughening in the homoepitaxy or heteroepitaxy and thus the epilayer experience a SK growth. Otherwise, the island can coalesce and the growth results FM. The model can be also used to understand the growth behavior as a function of the temperature, as the L_n and L_α can be expressed as a function of the temperature.

The model takes into account also of the offcut by the L_s parameter which depends on the miscut angle θ and the height of the vincinal steps. With a sufficiently high temperature or step density $L_n < L_s$ and in this case adatom can diffust to the surface steps before nucleating new islands. The grwth thus proceed as step-flow (SF). At lower temperature, $L_n > L_s$ so the growth mode will be layer-by-layer (FM), whereby islands nucleated and then coalescence. At still lower temperatures, $L_\alpha < L_n$ so that multilayer (SK) growth will result. The model also can explain qualitatively the observation of reentrant layer-by-layer growth [2.37], in which the growth mode at high and low temperature differs from that at medium temperature range. The model results describe well the STM observation of pure Ge growth onto an off-cut Silicon substrate [2.38] almost qualitatively as it does not take into account the surface reconstruction as a function of the temperature which generate a anisotropical diffusion of Ge adatoms on the surface, or the presence of a surfactant which modify the free energy of the surface. Anyway, the TDT model is useful in order to understand qualitatively the behavior of lattice growth during the epitaxy processes.

2.4 Ge/Si integration

A real challenge is represented by the integration of high content $Si_{1-x}Ge_x$ layers onto Silicon (100) substrates. As describe earlier, the high lattice mismatch of $f \cong 4.18\%$ for pure Ge results in a critical thickness than is less than 1 nm and in an uncontrolled plastic relaxation characterized by a high number of dislocations which interact and cause an high TDDs at the interface. The high elastic energy gained even after few MLs, induce the epilayer to split into clusters whose dimension and orientation depends on the cluster

volume and the growth temperature [2.39]. This change in creating an high density of localized nanostructures (10^9 – 10^{11} cm^{-2}) are gaining much attractiveness as they can be used as quantum dots (QDs) or seed for self-organized device classes [2.15]. A stacked sequence of Ge islands have been successfully employed as intermediate layer into a p-i-n Silicon solar cell in order to enhance the performance of the cell in the near-infrared regime [2.40]. On the other hand, relaxed Ge epilayer with low TDDs can be used as a virtual substrate (VS) for III-V alloys integration with low cost silicon substrate in the field of the optoelectronics [2.41] and high-efficiency concentrator photovoltaic (CPV) solar cell [2.42]. Below, a brief review of the issues and literature works on the Ge/Si epitaxy is presented.

2.4.1 H_2 influence

It has been recognized the function of the atomic H_2 in the Ge/Si heteroepitaxy system as surfactant [2.43 – 2.44]. Surfactants are surface-segregated impurities, which have a number of applications in heteroepitaxy and engineered hererostructures. Surfactants may alter the growth mode for heteroepitaxy by modification of the surface energies for the substrate or the epitaxial layer, if the growth mode is determined by thermodynamics. Alternatively, a surfactant may change the surface diffusivities or the energy barriers at the edge of the islands, if the growth mode is determined by kinetics [2.8]. During CVD processes, molecular or atomic hydrogen is naturally generated by the scission of the gas precursors, such as GeH_4 or SiH_4, or either injected into the reactor as surfactant. By using UHV-CVD deposition at temperatures lower than 400°C, the introduction of a relative low partial pressure of H_2 results in a great enhancing of the surface diffusivity and thus an extended layer-by-layer growth at thickness for which 3D growth are expected [2.43]. In Fig. (2.15) the RHEED analysis are presented as function of the temperature and H_2 partial pressure. Best enhancing is found at lower temperature of 100 – 300 °C, in which the extended RHEED oscillations indicates a FM growth, while at higher temperatures, no difference can be found by the comparison with sample grown without the H_2 inclusion. This effect can be addressed to a higher desorption rate of hydrogen which limits the surface coverage. The RHEED analysis confirm a nearly flat surface up to 55 MLs in these conditions, characterized by a 1x1 surface reconstruction. A flatterning effect on Ge(100) surface at 300 - 400 °C have been also reported by Kahng [2.44]. On the other hand, an excess of H_2 can generates pin holes within the epilayer as the hydrogen bond more

strongly with silicon than germanium [2.44]. The use of hydrogen also have been proved to strongly suppress the Ge surface segregation during Si/Ge/Si overgrowth [2.45].

2.4.2 Defect induced relaxation

In order to avoid uncontrolled plastic relaxation of the pure Ge epilayer, a very thin buffer layer grown at particular epitaxial conditions or treated employing a particular procedure is often used [2.46-2.48]. The idea is to create a thin layer, commonly called *seed layer,* with a characteristic high vacancy or interstitial defectivity density which accommodate the mismatch and thermal strain between the epilayer and the substrate while suppressing the extending of TDD segment through the epilayer by interaction with the layer defectivities [2.46]. It is infact proved that a high concentration of induced *point defects* within the lattice structure can efficiently suppress the extending of the line defects by pinning during the onset stage of relaxation [2.49]. Once the TD is pinned, the gliding can proceed only if the TD climbs the point defect, and this process promotes the mutual annihilation of TD arms. [2.50]. The introduction of point defects supersaturation within the buffer layer, reduces also the kinetic barrier against dislocation generation, shorten the metastable pseudomorphic growth and provoke relaxation of thinner layers [2.50]. Furthermore, the planar condensation of point defects cause the nucleation of prismatic dislocation loops inside the layer, which may reduce the need for nucleation of dislocation half-loops at the surface [2.51].

Supersaturation of point defects within the buffer layer can be produced by 1 kV Si^+ ion bombardment of the layer suface during the metastable pseudomorphic growth stage [2.50] and by a 25keV implantation of Ar ions onto the Silicon substrate [2.52]. The subsequent overgrowth of a $Si_{0.8}Ge_{0.2}$ at 500°C and annealing at 900°C allows a very low TDD density within the epilayer as a dense network of dislocation which generates at the interface promote the relaxation of the epilayer. In this way, the defectivity caused by the plastic relaxation is mostly confined within the volume regions near the silicon substrate surface, thus reducing strongly the TD arms which propagates through the epilayer.

On the other hand, a drastic reduction of the growth temperature can give rise to epilayers with an ordered crystal structure but with a high density of vacancy point defects. This process is mainly due to a strong reduction of the surface diffusivity of the adatoms which impinges on the substrate surface [2.53]. This process is effective only if the temperature substrate is low enough to favor the generation of vacancies in the lattice, but high enough

to avoid the amorphous growth of the epilayer. Studies base on Si homoepitaxy also indicate a narrow temperature process window for crystalline epitaxial layer grown at temperature lower than 200 °C [2.54]. This process is also strongly influenced by the adatom flux and thickness of deposited epilayer due to the kinetic growth considerations described in Section 2.3.2. The real challenge is thus a very tight control of the key parameters during deposition, with particular attention to the substrate temperature profiles. After the thin low temperature (LT) seed layer is grown, a subsequent overgrowth step at high temperature (HT) is then performed. Comparing to a constant temperature epitaxial process, the lattice mismatch between the HT layer and the substrate is accommodated by the LT layer, which acts as a VS for the subsequent overgrowth while confining within its volume the plastic relaxation induced dislocations. The drastic reduction of the TDD and in-plane strain also play a decisive role in reduction of the surface roughness. The multi-step growth have been applied successfully by Bauer *et al.* [2.46] to the SiGe/Si system in order to obtain strain-relaxed VS with thickness under 0.1 μm. The first step growth parameters are calibrated as a function of the Ge content, while the thickness slight exceed the equilibrium critical thickness predicted by the Matthews-Blakeslee theory. The subsequent HT growth is performed at 550°C until the People metastability thickness defined by Eq.(2.12) is reached. In Fig.(2.16) are presented a TEM imaged comparison between a standard constant temperature and LT-HT combination growth. While the standard growth creates strain pseudomorphic layers, the temperature modulation growth allows to obtain epilayers with a relaxation $R \sim 90 –$ 100% and virtually free of TDDs. Zhou *et al.* [2.55] uses a LT Ge seed layer grown at 350 °C onto Silicon (100) substrate and a subsequent HT at 600°C. By this way, a thin VS with a relaxation factor of about 99% and a TDD of $5x10^5$ cm^{-2}. The root mean square (RMS) roughness of the epilayer surface has been evaluated as 0.7 nm. Although the good results, the growth rate is lower than 1.17 nm/min for the HT layer, while it results as low as 0.58 nm/min for the LT seed layer. This results in a overall deposition time of about 4h. A similar processes have been used by Shin *et al.* [2.56] and Olubuyide *et al.* [2.57] which studies the impact of a LT seed layer on the roughness and TDD for a Ge/Si heteropitaxial system while modulating the substrate temperature within the range of 330 °C and 350 °C. Even in this case, a very narrow temperature window process is identified, as LT layer grown for temperature higher than 350°c lead to a surface roughening due to enhanced adatom mobility, while for temperature lower than 330°C too many defects are generated. At the optimal value of 335°C, an onset 3D growth is observed which instead become more smoother as the deposition process proceed due to coalescence of the islands.

Furthermore, in case a temperature ramp is set between the LT and HT layer growth, a slight increase on the overall surface roughness can be achieved. Finally, a very smooth pure Ge layer with a RMS ~ 1.9 nm and a TDD of $2x10^7$ cm^{-2} is obtained using a 30 nm LT seed layer grown at 335 °C and a HT temperature ramped layer.

Other techniques employed in SiGe/Si epitaxy for TDD and surface roughness suppression involve the use of continuously or stepwise graded SiGe buffers [2.58], thick graded buffers with following chemical-mechanical polishing [2.59], H or He implantation with formation of bubbles below the interface to direct the dislocation arms beneath the layer itself [2.60] and compliant substrates in order to use the higher plasticity of the material for TDD reduction [2.61].

2.5 Layers characterizations

A wide variety of techniques were used to characterize the epitaxial films and structure developed. These comprehend surface roughness, composition, layer thickness, defect density and residual strain.

2.5.1 Atomic Force Microscopy (AFM)

The quantification of the surface rougheness has been conducted using an Atomic Force Microscopy (AFM) characterization. A quick surface scan with a stylus allows for accurate determination of the surface roughness, as shown in the example of Fig.(2.16) of a Ge/Si (100) sample grown at 570 °C. Built in analysis tools are employed to determine the root means square (RMS) roughness and the maximum peak-to-valley heigh. The main drawbak associated with this technique is that it samples a very small are of the wafer surface, typically a square are ranging from about 1x1 μm^2 to 50 x 50 μm^2, so several assessment of the surface RMS have been conduct in different part of the sample as to evaluate the epilayers surface uniformity. The entire set of measurements conducted in this work have been performed using a Nanoscope III Digital Instruments in *contact mode* configuration.

2.5.2 Etch Pit Density (EPD)

A common and dependable method for determining dislocation density in lattice mismatched layers is direct imaging of the defects with plan-view TEM (PVTEM). Unfortunately, the maximum imageable are using electron microscopy is typically smaller than 10x10 μm^2. Assuming a magnification of 10 000x, a sample containing 10^5 cm^{-2} TD will require a hundreds of TEM micrograph to yield a statistically meaningful TDD value. An alternative method for revealing dislocations is selective etching of the sample and subsequent etch-pit density (EPD) measurement. Chemical etching reveals dislocations by selectively attacking their highly strained cores. EPD measurements are suitable for samples containing relatively low ($<10^8$ cm^{-2}) TDs since the etch-pits can overlaps, causing an underestimation of the TDDs value. In this work, the sample have been chemically etched using a Secco etch solution [2.62] as it does not have preferential planes of etching. This solution have been successfully applied to $Si_{1-x}Ge_x$ layers for Ge concentration up to $x = 0.9$ [2.63]. The EPD value have been successively retrieved using either an optical microscope or SEM images.

2.5.3 High Resolution X-Ray Diffraction (HRXRD)

The X-ray diffraction (XRD) is the most direct and accurate way to characterize the crystallographic quality and residual strain in a deposited semiconductor epilayer. High energy monocorator x-ray diffracted of the epilayers will generate pattern of diffraction peaks that can be measured and quantify to yield precide information on the symmetry, lattice spacing, orientation, crystalline quality and the integrated dislocation density over the epilayer and substrate thickness. The entire measurements conducted in this work have been performed using a PANanalytical X'Pert PRO-MRD, which have a Bartel's monochromator with four Ge (400) crystals. The radiation emitted from the Cu anode, filtered by the monochromator, is composed by the CuK_{α_1} peak with spectral purity of 10^{-5}. The analysis conducted on the samples are composed by symmetrical $\theta/2\theta$ scans for the (400) surface and asymmetrical (224) / (113) scansions. The strain relaxation of the Ge epilayers is evaluated using the Hornstra and Bartel model [2.64]. This model, which is based on the theory of elastic anisotropy, neglects the strain in the substrate and its associated curvature when growing the a lattice-mismatched layer on top. It however takes into account the anisotropy of diamond Si and Ge. For the (100), the relation linking the in-plane stress $\varepsilon_{||}$ and the perpendicular strain ε_z can be expressed as

$$\frac{\varepsilon_{||}}{\varepsilon_{||}+\varepsilon_z}=\frac{c_{11}}{c_{11}+2c_{12}} \tag{2.22}$$

where the c_{11} = 12.85 x 10^{10} Pa and the c_{12} = 4.83 x 10^{10} Pa have been retrieved from Ref. [2.65]. The in-plane lattice constant of Ge $a_{||}$ can be calculated using the expression

$$a_{||}=\frac{1}{2c_{12}}\left(a_{bulk}(c_{11}+2c_{12})-d_{\theta_{400}}c_{11}\right) \tag{2.23}$$

where a_{bulk} = 5.65785 Å and $d_{\theta_{400}}$ is the perpendicular lattice constant calculated as $d_{\theta_{400}}=4\lambda_{CuK_\alpha}/\sin\theta_{400}$, where λ_{CuK_α} is the wavelength of the CuK_{α_1} at 1.540594 Å. Afterwards, the relaxation factor R can be evaluated as

$$R=\frac{a_{||}-a_{Si}}{a_{bulk}-a_{Si}} \tag{2.24}$$

where a_{Si} = 5.43105 Å. The in-plane stress can be also evaluated using alternatively two asymmetric reflection or a symmetrical combined with an asymmetrical diffraction rocking curves. Detailed description of the method can be found in Ref. [2.66]. The general expression for calculation of the in-plane stress $\varepsilon_{||}$ and the lattice mismatch f using the diffraction curves relative to the $(h_i\ k_i\ l_i)$ and $(h_j\ k_j\ l_j)$ crystal planes can be expressed as

$$\varepsilon_{||}=\left(\Delta\omega_i\cot\vartheta_i-\Delta\omega_j\cot\vartheta_j\right)\cdot$$
$$\cdot\left\{\frac{1-\nu}{1+\nu}\left[\left(\cos^2\varphi_i-\cos^2\varphi_j\right)+\frac{1}{2}\left(u\ \cot\vartheta_i\sin 2\varphi_i-w\ \cot\vartheta_j\sin 2\varphi_j\right)\right]\right\}^{-1} \tag{2.25}$$

$$f=-\Delta\omega_i\cot\vartheta_i+\varepsilon_{||}\frac{1-\nu}{1+\nu}\cdot\left[\cos\varphi_i\left(u\ \cot\vartheta_i\sin\varphi_i+\cos\varphi_i\right)-\frac{1-\nu}{1+\nu}\right] \tag{2.26}$$

where $\vartheta_{i,j}$ are the substrate Bragg angles for the $(h_i\ k_i\ l_i)$ and $(h_j\ k_j\ l_j)$ planes respectively, $\varphi_{i,j}$ the inclination angle of the two crystal planes respect to the wafer surface, and u and w are two parameters which are related to the geometrical set-up of the diffraction measurements [2.66]

The HR-XRD rocking curves can be also used to understand the influence of several physical aspects which influence the shape of the diffraction peaks, by using the kinematic

theory of X-ray diffraction. This theoretical approach neglects both the primary and secondary extinction of the incident wave, which is assumed to be attenuated only by normal photoelectric absorption [2.8]. Furthermore, the kinematic theory neglects also the refractive index of the material under analysis. As a consequence, this theory gives good results for samples in which the film results highly defective or distorted, as the case considered in this work of Ge/Si highly-mismatched heterostructures, where the average dimensions of the blocks are small respect to the extinction length in the material. In particular, the deviation of the diffraction peak broadening from that derived from theoretical calculation is considered as the convolution of different peak broadening components which depends by different epilayers non-idealities. Assuming that the diffracted peak profile is Gaussian, the full width at maximum (FWHM) $\beta_m(hkl)$ can be deconvoluted using several Gaussian intensity distribution, each one corresponding to a different broadening mechanism [2.8]

$$\beta_m^2(hkl) = \beta_0^2 + \beta_d^2 + \beta_\alpha^2 + \beta_\varepsilon^2 + \beta_L^2 + \beta_r^2 \tag{2.27}$$

where β_0^2 is the intrinsic rocking curve width for the crystal being examined, β_d^2 is the width of the instrumental broadening function, β_α^2 is the rocking curve broadening caused by angular rotation at dislocations, β_ε^2 is the rocking curve broadening caused by inhomogeneous strain surrounding dislocations, β_L^2 is the broadening due to the crystal size, i.e. the layer thickness, and β_r^2 is the broadening due to curvature of the heteropitaxial specimen. Detail description of each component can be retrieved in Ref. [2.8]. Below, are summarize the expression of each rocking curve broadening components of Eq.(2.27)

a. *Intrinsic peak width*

Assuming a negligible absorption for a symmetrical Bragg reflection and a unpolarized primary beam, the intrinsic peak broadening can be expressed as

$$\beta_0 = \frac{2r_e\lambda^2[1 + \cos(2\theta_B)]|F_H|}{\pi V \cdot \sin(2\theta_B)} \tag{2.28}$$

Where r_e is the classical radius for the electron, i.e. 2.818 x 10^{-5} Å , λ is the wavelength of the incident X-ray, $|F_H|$ is the magnitude of the structure function, V is the crystal volume for which the $|F_H|$ is calculated, i.e. $V = a_0^3$, and θ_B is the Bragg angle.

b. *Angular rotation at dislocation*

The derivation of the broadening due to angle rotation at dislocations, it is first assumed that the crystal in examination is comprised of an arrangement of subsidiary mosaics with mutual inclination and each subsidiary is associated with a dislocation. It is furthermore assumed that the dislocations are arranged in a random network with an average spacing of $1/\sqrt{D}$, where D is the dislocation density. By these assumption, the expression for the peak broadening can be expressed as

$$\beta_{\alpha}^{2} \approx (2\pi \ln 2) b^{2} D \tag{2.29}$$

where b is the Burger vector.

c. *Dislocation strain broadening*

It is assumed first that the random array of TDs give rise to a Gaussian distribution of local strain. For half-loops in a (100) diamond or zincblende epitaxial layer, with 60° misfit segments and screw threading segments, the dislocation strain broadening component can be expressed as

$$\beta_{\varepsilon}^{2} = 0.09 b^{2} D \left| \ln\left(2\text{x}10^{-7}[cm]\sqrt{\text{D}}\right)\right| \tan^{2}\theta_{\text{B}} = K_{\varepsilon} \tan^{2}\theta_{\text{B}} \tag{2.30}$$

where D is the dislocation density, b is the Burger vector, and θ_{B} is the Bragg angle.

d. *Finite thicknes broadening*

For heteropitaxial layers, this broadening components is only affected by the thickness h of the epilayer. The expression for the broadening due to a finite layer thickness can be described using the Scherrer equation [2.70]

$$\beta_{L}^{2} \approx \left[\frac{4 \ln 2}{\pi h^{2}}\right]\left(\frac{\lambda^{2}}{\cos^{2}\theta_{B}}\right) \tag{2.31}$$

e. Wafer curvature broadening

Due to a difference in the thermal expansion coefficient between the Silicon (2.6 x 10^{-6} °C^{-1}) and Germanium (5.8 x 10^{-6} °C^{-1}), the grown wafers generally exhibit a curvature of radius *R,* which usually is expressed in the meters. This bending curvature caused a non-uniformity in the layer thickness and this have a worsening influence on the further fabrication processes. The broadening component due to wafer bending can be expressed as

$$\beta_R = \frac{\beta_0(\sqrt{2}/3)}{R \sin\theta_B} \tag{2.32}$$

where β_0 is the intrinsic peak width, and θ_B is the Bragg angle.

Among the broadening components listed earlier, the β_L^2 and β_R components can be determined with high accuracy once the R and h have been experimentally retrieved. Afterwards, the only unknown parameters in Eq.(2.27) are the two broadening component due to dislocations. By performing a set of at least two $\theta/2\theta$ scans, these two variables can be calculated using a system of two Eq.(2.27), and finally the dislocation density D can be retrieved.

References

[2.1] J.P. Dismukes, L. Ekstrom, R.I. Paff, ' Lattice parameter and density in Germanium Silicon alloys ', *J. Phys Chem*, vol **68** (1964), p. 3021

[2.2] E. Kasper, ' Silicium Germanium heterodevices ', *Appl. Surf. Sci.*, vol **102** (1996), pp. 189-193

[2.3] Yu.B. Bolkhovityanov, A.S. Deryabin, A.K. Gutakovskii, M.A. Revenko, L.V. Sokolov, ' Heterostructures Ge_xSi_{1-x}/Si(001) grown by low-temperature (300-400 °C) molecular beam epitaxy: Misfit dislocation propagaition ', *J. of Crystal Growth,* **vol.** 280 (2005), pp. 309-319

[2.4] K. Tamamura, K. Akimoto, Y. Mori, *J. Crystal Growth,* **vol.** 94 (1989), p. 821

[2.5] R. Houndre, H. Morkoc, *Critical Reviews in Solid state and Material Science,* **vol**. 16 (1990), p. 91

[2.6] R. Hull, J.C. Bean, *Critical Reviews in Solid state and Material Science*, **vol.** 17 (1992), p. 507

[2.7] M. Yamaguchi, C. Amano, *J. Appl. Phys.*, **vol.** 58 (1985), p. 3601

[2.8] J.E. Ayers, *Heteropitaxy of Semiconductors. Theory, Growth and Characterization,* CRC Press, 2007

[2.9] J.W. Matthews, A.E. Blakeslee, *J. Crystal Growth,* **vol.** 27 (1974), p. 125

[2.10] J.W. Matthews, A.E. Blakeslee, *J. Crystal Growth,* **vol.** 29 (1975), p. 280

[2.11] R. People, J.C. Bean, *Appl. Phys. Lett.*, **vol.** 47 (1985), p. 322

[2.12] J.H. van der Merwe, *J. Appl. Phys.*, **vol.** 34 (1962), p. 123

[2.13] J.C. Bean, L.C. Feldman, A.T. Fiory, S, Nakahara, I.K. Robinson, *J. Vac. Sci. Technol. A.*, **vol.** 2 (1984), p. 436

[2.14] J. Bek, J.P. Mannerts, L.C. Feldman, B.A. Davidson, A. Qurmazd, *Appl. Phys. Lett.*, **vol.** 49 (1986), p. 286

[2.15] E. Kasper, *Surf. Sci.*, **vol.** 174 (1986), p. 630

[2.16] J.C. Bean, *Science*, **vol.** 230 (1985), p. 127

[2.17] R. People, J. Bean, *Appl. Phys. Lett.*, **vol.** 49 (1986), p. 229

[2.18] E. Kasper, A. Schuh, G. Bauer, B. Holl[a]nder, H. Kibbel, *J. Crystal Growth*, **vol.** 157 (1995), p. 68

[2.19] J. Eberhardt, E. Kasper, *Solid-State Electronics*, **vol.** 45 (2001), p. 1325

[2.20] I. J. Fritz, *Appl. Phys. Lett.*, **vol.** 51 (1987), p. 1080

[2.21] B.W. Dodson, J.Y. Tsao, *Appl. Phys. Lett.*, **vol.** 51 (1987), p. 1325

[2.22] G. Vogg, F. Bensh, S. Kreuzer, R. Merkel, *Mat. Sci. Semic. Proc.*, **vol.** 8 (2005), pp. 161-165

[2.23] R. Beanland, *J. Appl. Phys.*, **vol.** 72 (1992), p. 3800

[2.24] F.K. LeGoues, B.S. Meyerson, J.M. Morar, *Phys. Rev. Lett.,* **vol.** 66 (1991), p. 2903

[2.25] M.A. Capano, L. Hart, D.K. Bowen, D. Gordon-Smith, C.R. Thomas, C.J. Gibbings, M.A.G. Halliwell, L.W. Hobbs, *J. Crystal Growth,* **vol.** 116 (1992), p. 260

[2.26] H.J. Frost, M.F. Ashby, *Deformation mechanism maps,* Pergamon, Oxford, 1982

[2.27] A.A. Chernov, ' Nucleation and epitaxy ' in *Modern Crystallogrphy III: Crystal Growth*, Springer-Verlag, New York, 1984

[2.28] P. Politi, *Physics Reports,* **vol.** 34 (2000), pp. 271-404

[2.29] R.J. Asaro, W.A. Tiller, *Metall. Trans.*, **vol.** 3 (1972), p. 1789

[2.30] M.Ya. Grinfeld, *Sov. Phys. Dokl.*, **vol.** 31 (1986), p. 831

[2.31] B. Voigtl[a]nder, Azinner, '*Appl. Phys. Lett.*, **vol.** 63 (1993), p.3055

[2.32] A.J. Pidduck, D.J. Robbins, A.G. Cullins, W.Y. Leong, A.M. Pit, *Thin Solid Films*, **vol.** 222 (1992), p. 78

[2.33] J. Tersoff, *Phys. Rev. Latt.*, **vol.** 43 (1991), p.9377

[2.34] K. Nakajima, T. Uijhara, N. Usami, K. Fujiwara, G. Sazaki, T. Shishido, *J. Crystal Growth,* **vol.** 26 (2004), p. 372-383

[2.35] G. Ehrlich, F.G. Hudda, *J. Chem. Phys.,* **vol.** 44 (1966), p. 1039

[2.36] J. Tersoff, A.W. Denier van der Gon, R.M. Tromp, *Phys. Rev. Lett.*, **vol.** 72 (1994), p. 226

[2.37] R. Kunkel, B. Poelsema, L.K. Verheij, G. Comsa, *Phys. Rev. Lett.*, **vol.** 65 (1990), p. 733

[2.38] B. Voigtländer, *Surface Science Reports,* **vol.** 43 (2001), p. 127-254

[2.39] L.V. Arapkina, V.A. Yurye, *Phys.-Usp.*, **vol.** 53 (2010), p. 279

[2.40] N. Usami, A. Alguno, T. Ujihara, K. Fujiwara, G. Sazaki, K. Nakajima, K. Sawano, Y.Shiraki, *Sci. Tech. Adv. Mat.*, **vol.** 4 (2003), p. 367-370

[2.41] D.W. Goodman, *Heterostructures on Silicon: one step further with silicon*, by Y.I. Nissim and E. Rosencher (Kluwer, Dordrecht, 1989)

[2.42] C.L. Andre, *III-V Semiconductors on SiGe substrates for Multi-Junction Photovoltaics,* Ph.D. Thesis, Ohio State University, 2004

[2.43] D. Dentel, J.L. Bischoff, T. Angot, L. Kubler, *Surf. Sci.*, **vol.** 402 (1998), pp. 211-214

[2.44] S.J. Kahng, Y. Kuk, *Sci. Rep. RITU A,* **vol.** 44 (1997), pp. 59-61

[2.45] K. Nakagawa, A. Nishida, Y. Kimura, T. Shimada, *J. Crystal Growth*, **vol.** 150 (1995), pp. 939-943

[2.46] M. Bauer, K. Lyutovich, M. Oehme, E. Kasper, H.-J. Herzog, F. Ernt, *Thin Solid Films,* **vol.** 369 (2000), pp. 152-156

[2.47] Y.H. Luo, J. Wan, R.L. Forrest, J.L. Liu, M.S. Goorsky, K.L. Wang, *J. Appl. Phys.*, **vol.** 89 (2001), p. 8279

[2.48] T. Egawa, A. Sakai, T. Yamamoto, N. Taoka, O. Nakatsuma, S. Zaima, Y. Yasuda, *Appl. Surf. Sci.*, **vol.** 224 (2004), pp. 104-107

[2.49] R. Köhler, H. Raidt, W. Neumann, J-U Pfeiffer, H. Schäfer, U. Richter, *J. Phys. D: Appl. Phys.*, **vol.** 38 (2005), pp. 319-327

[2.50] K. Lyutovich, E. Kasper, F. Ernst, M. Bauer, M. Oehme, *Mat. Sci. Engin. B*, **vol.** 71 (2000), pp. 14-19

[2.51] E. Kasper, K. Lyutovich, M. Bauer, M.Oehme, *Thin Solid Films*, **vol.** 336 (1998), pp. 319-322

[2.52] J. Yamanaka, K. Sawano, K. Suzuki, K. Nakagawa, Y. Ozawa, T. Hattori, Y. Shiraki, *Thin Solid Films*, **vol.** 508 (2006), pp. 103-106

[2.53] K. Lyutovich, M. Bauer, E. Kasper, H.J. Herzog, T. Perova, R. Maurice, *et al.*, *Mater. Sci. Eng. B*, **vol.** 89 (2002), p. 341

[2.54] H. Jorke, H.-J. Herzog, H. Kibbel, *Phys. Rev.*, **vol.** 40 (1989), p. 2005

[2.55] Z. Zhou, C. Li, H. Lai, S. Chen, J. Yu, *J. Crystal Growth*, **vol.** 310 (2008), pp. 2508-2513

[2.56] K.W. Shin, H.-W. Kim, J. Kim, C. Yang, S. Lee, E. Yoon, *Thin Solid Films*,

[2.57] O.O. Olubuyide, D.T. Danielson, L.C. Kimerling, J.L. Hoyt, *Thin Solid Films,* **vol.** 508 (2006), pp. 14-19

[2.58] C. Rosenblad, J. Stangl, E. Müller, G. Bauer, H. von Kaenel, *Mat. Sci. Eng. B*, **vol.** 71 (2000), p. 20

[2.59] E.A. Fitzgerald, M.T. Currie, S.B. Samavedam, T.A. Langdo, G. Taraschi, V. Yang *et al.*, *Physica Status Solidi (a)*, **vol.** 171 (1999), p. 227

[2.60] S. Mantl, B. Holländer, R. Liedtke, S. Mesters, H.J.Herzog, H. Kibbel, *et al.*, *Nucl. Instr. Meth. B,* **vol.** 147 (1999), p. 29-34

[2.61] A.R. Powell, S.S. Iver, F.K. LeGues, *Appl. Phys. Lett.*, **vol.** 64 (1994), p 1856

[2.62] F. Secco d'Aragona, *J. Electrochem. Soc.*, **vol.** 119 (1977), p. 757

[2.63] S. Marchionna, A. Virtuani, M. Acciarri, G. Isella, H. von Kaenel, *Mat. Sci. Semi. Proc.*, **vol.** 9 (2006), pp. 802-805

[2.64] J. Honstra , W.J. Bartel, *J. Crystal Growth*, **vol.** 42 (1978), p. 513

[2.65] H.J. McSkimin, P. Andreatch Jr., *J. Appl. Phys.*, **vol.** 34 (963), p. 651

[2.67] M. Yamaguchi, C. Amano, Y. Itoh, *J. Appl. Phys.*, **vol.** 66 (1989), p. 915

[2.68] P.P. Debye, E.M. Conwell, *Phys. Rev.*, **vol.** 93 (1954), pp. 693-706

[2.69] C.L. Andre, *III-V Semiconductors on SiGe substrates for Multi-Junction Photovoltaics,* Ph.D thesis, Ohaio State University, 2004

[2.70] F. Scherrer, *Nachr. Gottinger Ges.*, **vol.** 98 (1918)

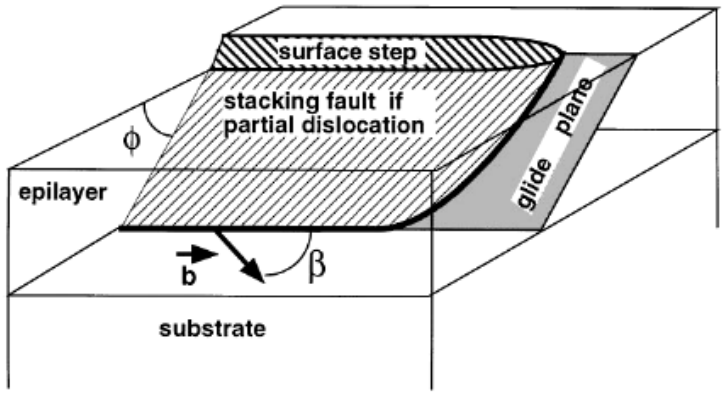

Fig. 2.1 A schematic representation of a discloation of Burger vector $\overline{\boldsymbol{b}}$ moving in the <111> glide plane.

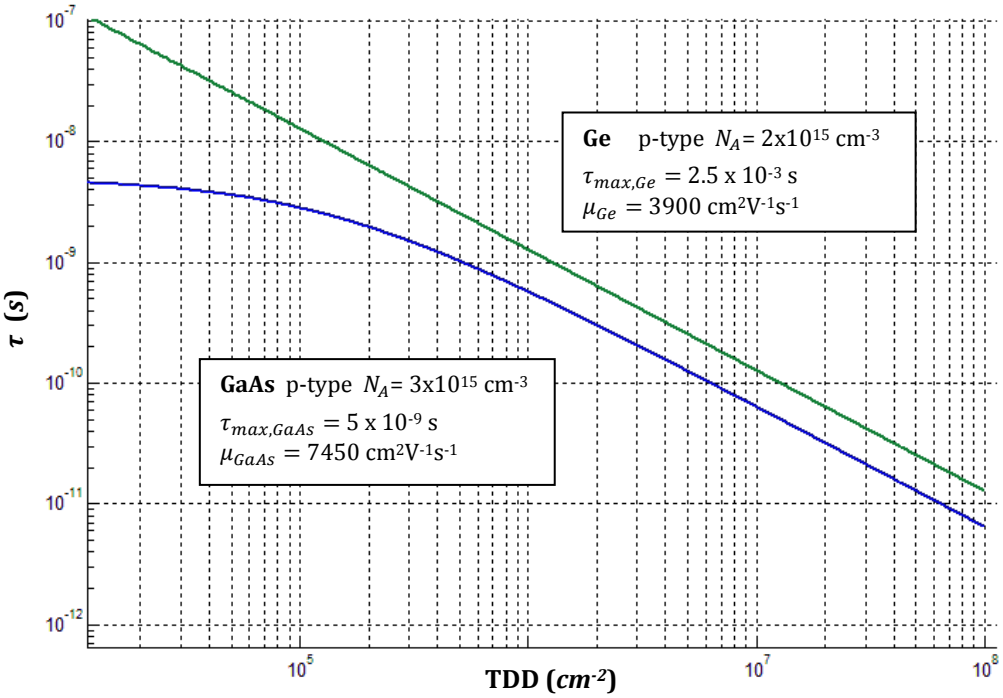

Fig. 2.2 Theoretical dependence of minority carrier lifetime on threading dislocation density calculated using the Eq. (2.8) and Eq. (2.10)

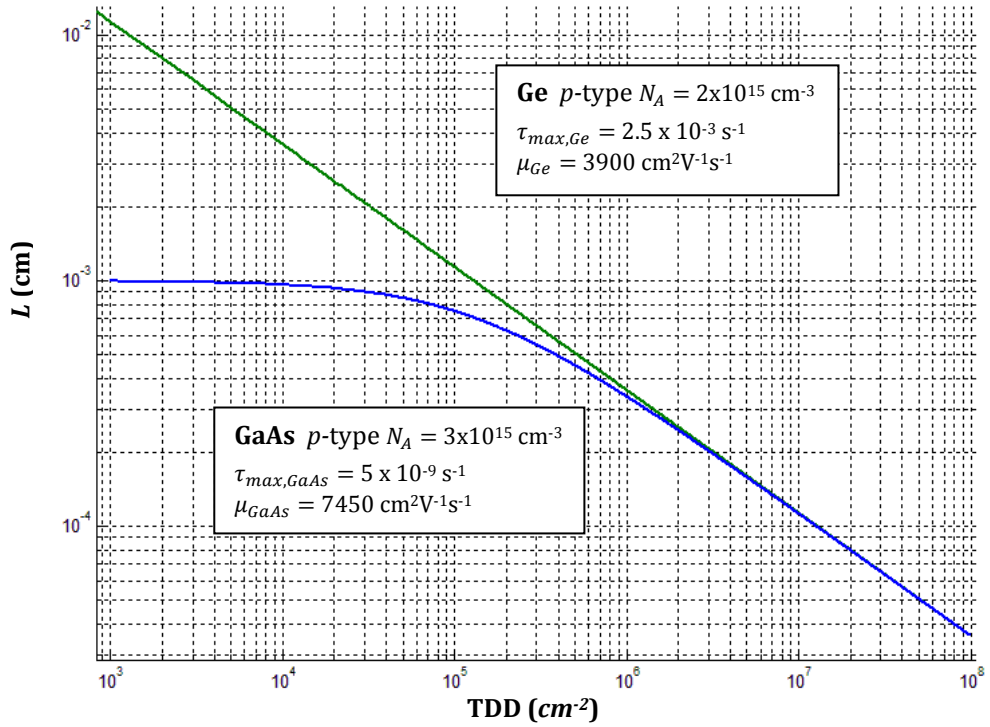

Fig. 2.3 Theoretical dependence of the diffusion length on the threading dislocation density calculated using Eq.(2.7) and Eq. (2.9)

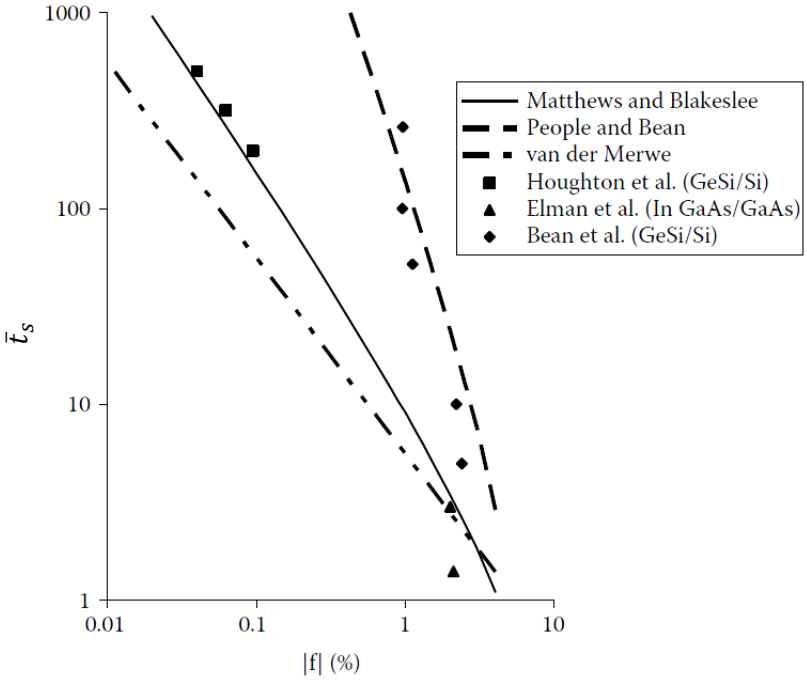

Fig. 2.4 Comparison between theoretical equilibrium calculations and experimental measurements of the critical thickness $\bar{t}_s$ (nm) as a function of the lattice mismatch [2.8]. The Mattews and Blakeslee curve is calculated assuming $\cos\lambda = \cos\alpha = 1/2$ and $b = a_{SiGe}/2 <$ 110 >.

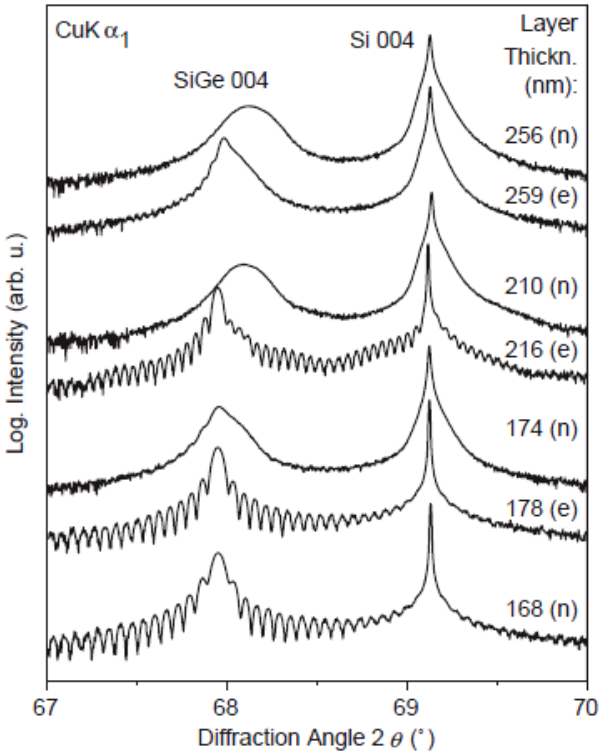

Fig. 2.5 HR-XRD rocking curves relative to $Si_{1-x}Ge_x$ samples grown onto etched (*e*) and non-etched (*n*) silicon substrate. The etched substrate are treated with gaseous HCl at 800 °C [2.22].

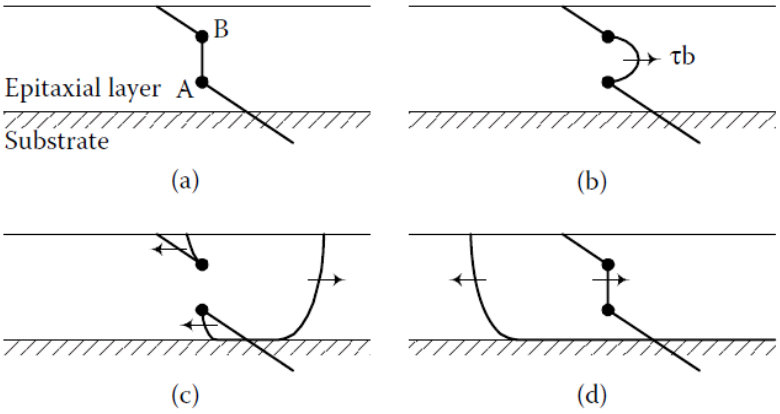

Fig. 2.6 Schematic representation of the dislocation multiplication by Frank-Read mechanism. [2.8]

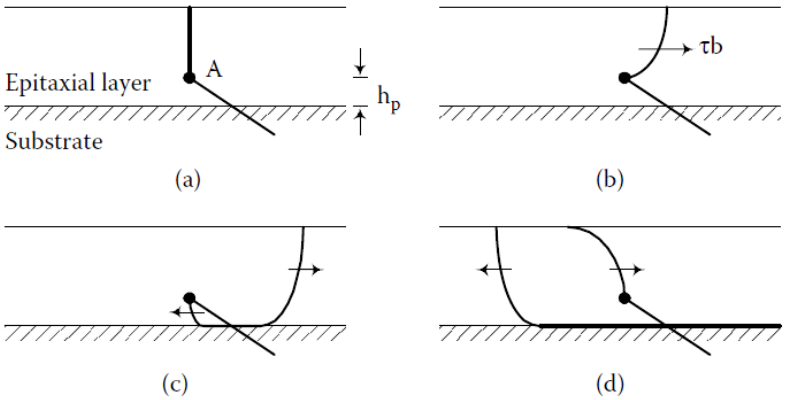

Fig. 2.7 Schematic representation of the dislocation multiplication by spiral mechanism. [2.8]

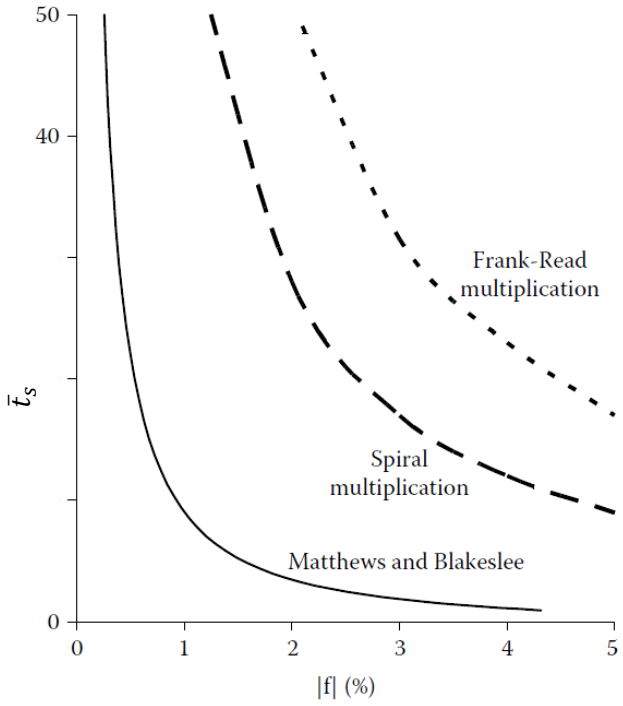

Fig. 2.8 Calculated theoretical critical thickness $\bar{t}_s$ using the kinetic formulation, in which the dislocation multiplication by the Frank-Read and spiral mechanisms are considered [2.8].

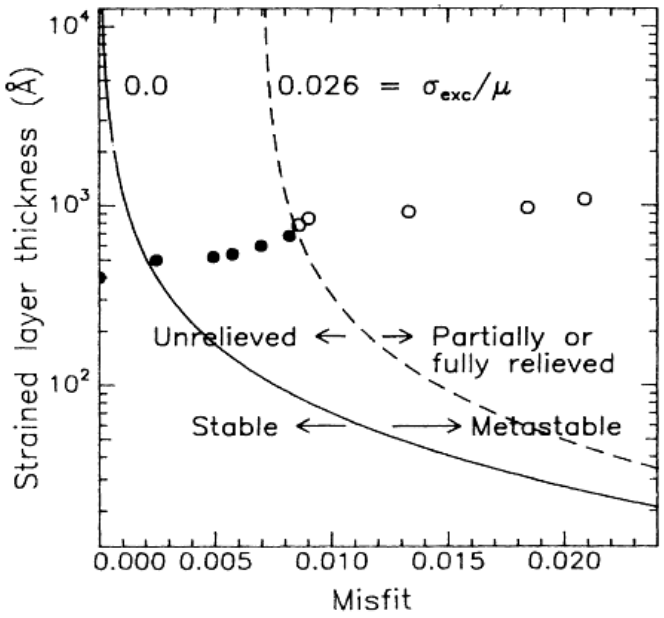

Fig. 2.9 Critical thickness as a function of the lattice mismatch for the $Ge_{1-x}Si_x/Ge$ films grown at 494°C, compared with experimental data. The fully strain (filled circles) and the relaxed (open circles) epilayers are separated by the $\sigma_{exc}/\mu = 0.026$ isobar. [2.21]

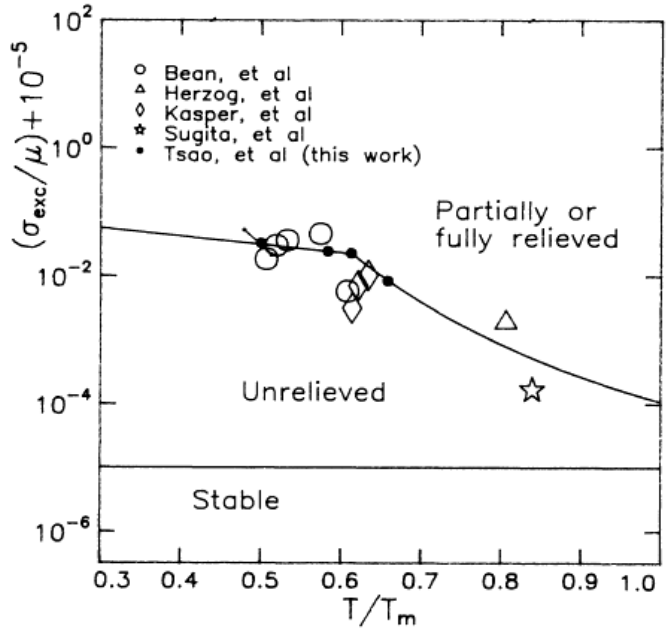

Fig. 2.10 The excess stress σ_{exc}/μ plotted as a function of the substrate temperature for the $Ge_{1-x}Si_x/Ge$ heterostructure. The excess stress have been offset of 10^{-5}, while the temperature is scaled to the melting temperature T_m [2.21]

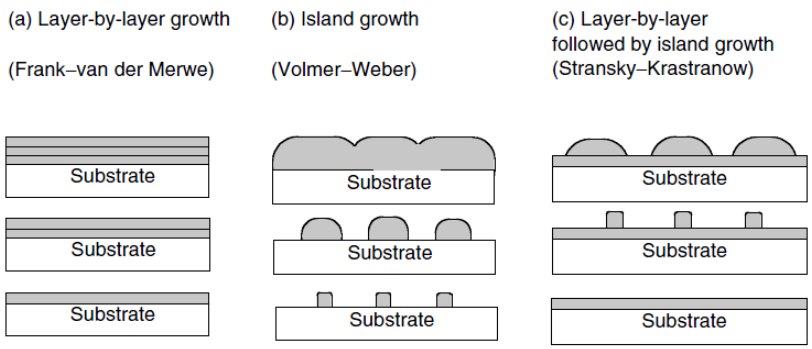

Fig. 2.11 Schematic representation of the heteroepitaxial layer growth modes.

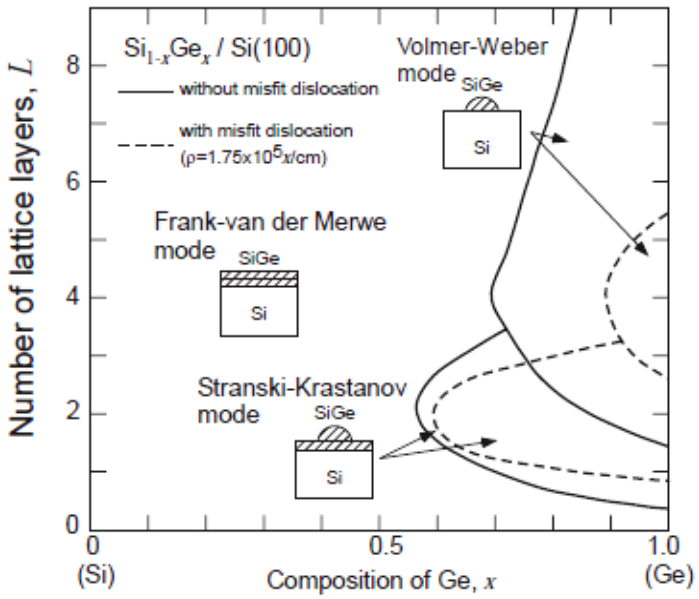

Fig. 2.12 Theoretical calculation of the $Si_{1-x}Ge_x/Si$ phase diagram in case dislocation generation is either considered or not [2.34].

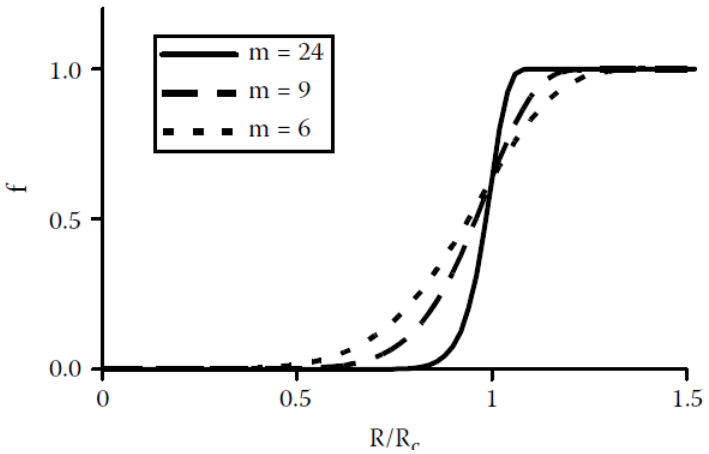

Fig. 2.13 Fraction of islands exhibiting second-layer nucleation vs. the normalized island size R/R_C with m as a parameter and R_C is the critical island size [2.36]

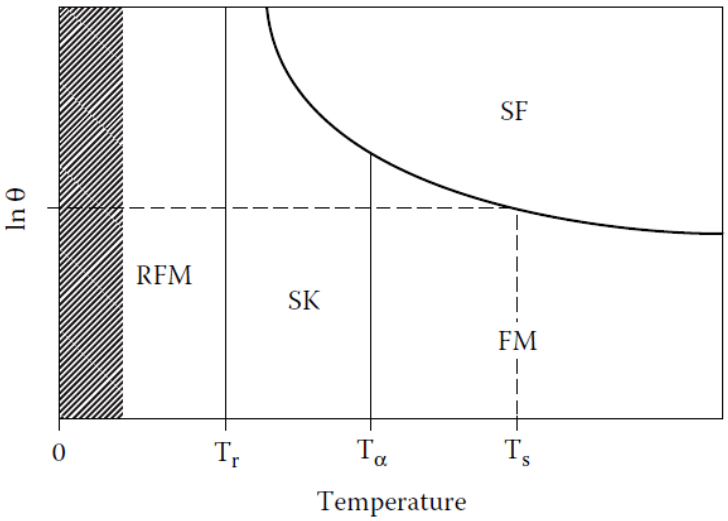

Fig. 2.14 Regimes of kinetically controlled growth modes for various values of temperature T and substrate miscut angle θ [2.36].

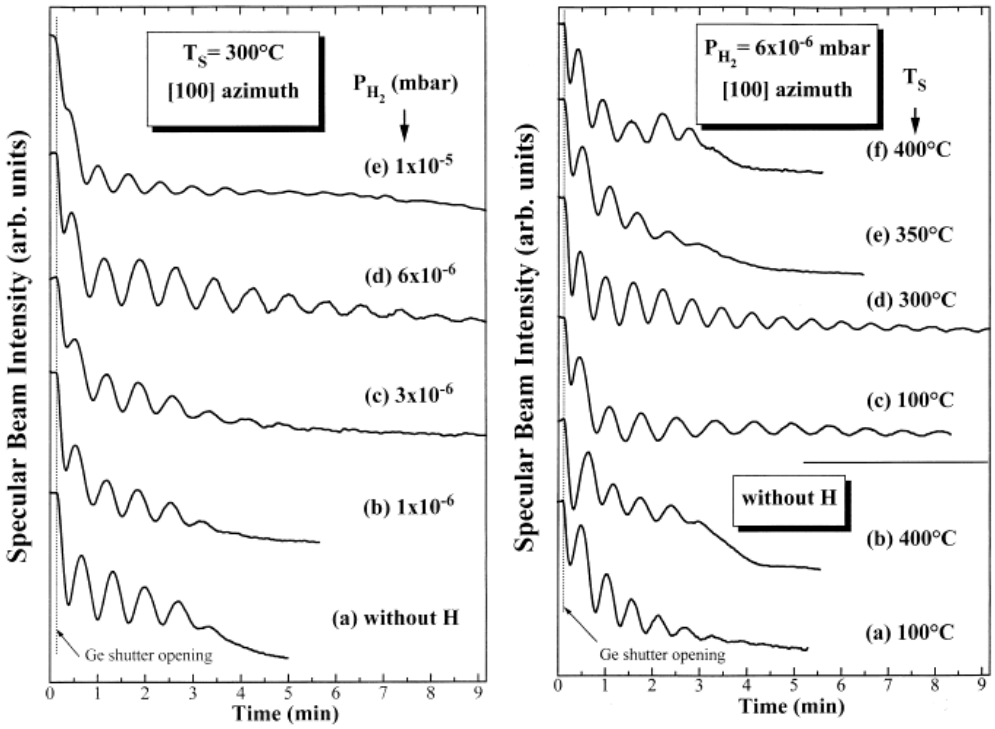

Fig. 2.15 RHEED specular intensity oscillations along the [100] azimuth during growth of Ge/Si (100) at 300°C for different P_{H_2} partial pressures (a), and for different temperature at $P_{H_2} = 6\text{x}10^{-6}$ mbar.

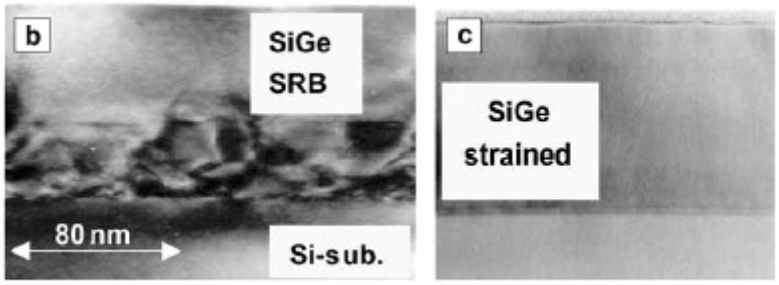

Fig. 2.16 Cross-sectional TEM images of a strain relaxed SiGe buffer structure grown by means of the LT-HT steps *(a)*, and SiGe epilayer for which the first LT step has been performed at 300°C [2.46]

CHAPTER 3
Plasma Enhanced Chemical Vapor Deposition

3.1 Plasma Enhanced CVD

A glow discharge can be defined as a partially ionized gas containing equal volume concentrations of positive and negative charged species, mostly ions and electrons, and different concentrations of ground-state and excited species [3.1, 3.2]. This partially ionized gas can be generated by subjecting the gas to very high temperatures or to strong electric or magnetic fields. In thermal plasmas, the electrons, ions, and neutral species are in local thermodynamic equilibrium while in 'cold ' plasmas, the electron and ions are more energetic than the neutral species. Most of the glow discharged used in microelectronics are generated by subjecting the gas to radio frequency (RF) electric field, and they are nonequilibrium glow discharges.

The electric filed initially accelerates a few free electrons present in the gas. Although the electric field also acts on the ions, they remain relatively unaffected because of their heavier mass. The accelerated electrons do not lose much energy in the elastic collisions with the gas species because of the large mass difference. Furthermore, these electrons do not even lose much energy during inelastic collisions which cause the excitation or ionization of the neutral species, until they reach the necessary threshold energies. As an example, for Argon activated plasmas the excitation energy is about 11.56 eV, while the threshold energy for ionization is 15.8 eV [3.1]. Consequently, these accelerated electrons gain energy quickly from the electric field. Once these electrons acquire sufficiently high

energies, their collisions with gas species result in excitations and ionizations, in which the latter generates additional electrons that are in turn, accelerated by the electric field. This transient process avalanches quickly, creating the steady-state glow discharge. In these steady-state conditions, the glow continuously loses charged species to the electrodes and other surfaces within the chamber, while gaining contemporarily a numerically equal number of electrons and ions from ionizations. Other mechanisms that produce additional electrons, such as secondary electron emission from positive ion bombardment on the electrodes and walls, are known to play a major role in sustaining the glow discharge [3.3]. The inelastic collisions between high energy electrons and gas species give rise to a highly reactive species, such as excited neutrals and free radicals, as well as ions and more electrons. In this manner, the energy of the electrons is used to create reactive and charges species without significantly raising the gas temperature [3.3]. The reactive species produces then, have lower energy barriers to physical and chemical reactions than the parent species and, consequently, can react at lower temperatures. The PECVD techniques thus uses these reactive species to deposit thin films at temperatures lower than those possible with thermally driven classic CVD reactors. Furthermore, the charges species in the glow discharge may also affect the properties of the deposited films [3.4, 3.5].

There are many possible inelastic collisions between electrons and gas species in a glow discharge. The most important processes which is involved during the PECVD epitaxial process are listed below

$$A + e^- \rightarrow A^* + e^- \qquad Excitation \qquad (3.1)a$$

$$A + e^- \rightarrow A^+ + 2e^- \qquad Ionization \qquad (3.1)b$$

$$A_2 + e^- \rightarrow 2A \quad + e^- \qquad Dissociation \qquad (3.1)c$$

$$A + e^- \rightarrow A^- \qquad Electron\ attachment \qquad (3.1)d$$

$$A_2 + e^- \rightarrow A \quad + A^- \qquad Dissociative\ attachment \qquad (3.1)e$$

$$A^* \rightarrow A \quad + h\nu \qquad Photoemission \qquad (3.1)f$$

Where A and A_2 are the reactant in molecular or atomic form, e^- is an electron, A^* is the reactant in excited state, and A^- and A^+ are ions of the A specie.

The rate at which these inelastic collision create excited species, ions, free-radicals can be estimated by using a reaction rate equation [3.6]. For example, the rate at which A^* is created from reaction (3.1)a can be expressed as

$$\frac{d[A^*]}{dt} = k_1[A][e^-] \tag{3.2}$$

where $[A^*]$ and $[A]$ are the concentrations of species A^* and A respectively, $[e^-]$ is the concentration of electrons, and k_1 is the reaction rate coefficient. Similar expressions can be derived also for the (3.1)b – (3.1)e reactions. As described earlier, only high energy electrons can take part in inelastic collisions. In order to take this into account, the k_1 parameter can be expressed as a function of the electron velocity and the inelastic cross-section. The cross-section $\tilde{\sigma}$ of an electron-reactant inelastic collision is proportional to the probability that this process will occurs and is a function of the electron energy. In case the energy of the electrons is lower than the required threshold energy, the collision cross section infact is zero. The rate coefficient k_i for the i reaction can be calculated by using the expression [3.6]

$$k_i = \int_0^\infty \left(\frac{2E}{m_e}\right)^{1/2} \tilde{\sigma}_i(E) \cdot f(E) \cdot dE \tag{3.3}$$

where E is the electron energy, m_e is the electron mass, $\tilde{\sigma}_i$ is the collision cross section and is a function of E, $f(E)$ is the electron energy distribution function and give the fraction of free electrons having a given energy, while the $(2E/m_e)^{1/2}$ represent the electron velocity. The integration is thus carried out over all possible electron energies. Some collision cross-section can be found in literature [3.7]. However, most of the of the cross-sections of interest in microelectronics are not known. As an example, in Fig. (3.1) is shown the rate coefficient for the different electron interactions mechanisms with the Ar gas. The dashed line in the plot represent the total cross-section $\tilde{\sigma}_t$, which can be calculated as the sum of the entire set of the cross-sections related to all the inelastic collisions processes. A similar situation exists with the electron energy distribution function $f(E)$. It is typical to assume a Maxwell-Boltzmann distribution, in which a large fraction of the electrons have energies lower than or equal to the average electron energy, and the fraction of electrons having higher energies decays exponentially with increasing energy. However, the actual electron energy distribution function is not known, and some theoretical models based on non-Maxwellian distribution have been proposed [3.3]. Moreover, it is possible that the reactant composition of the gas influence the $f(E)$ function because the higher-energy electrons lose a significant fraction of the their energies in inelastic collision with the reactants. Consequently, it is difficult to calculate

reaction rate coefficients and reaction rates theoretically. In Fig. (3.2) is schematically illustrated the electron energy distribution function. The equilibrium energy distribution is also shown for comparison. The effect of an electric field is to shift electrons to higher energies and therefore over-populate the high-energy region relative to the Maxwellian distribution. Electron undergoing inelastic collisions are transferred from the high energy to the low-energy end of the distribution. Electron-electron collisions tend to smooth the distribution and drive it toward the Maxweillian form. If these collision dominates such that a state of detailed balace exists for one dominat process, than the $f(E)$ can be well approximated by a Maxweillian distribution and an electron temperature can be used to describe the state of the electrons. However, even this case seldom occurs in practice. In high-pressure discharges, the electric field perturbation is usually minimal allowing the distribution function to be approximately Maxweillian, although it may be somewhat depleted at high energies by inelastic collision. In low-pressures discharges, the electric field can generate relatively large numbers of energetic electrons and, in the extreme, produce a bimodal distribution function.

In case the collision cross-section is assumed independent from the energy and the electrons energy distribution function is assumed being Maxwellian with electron temperature T_e, then Eq. (3.3) can be simplified as

$$k_i = \tilde{\sigma}_i \left(\frac{8kT_e}{\pi m_e}\right)^{1/2} \tag{3.4}$$

where k is the Boltzmann constant, and $(8kT_e/\pi m_e)^{1/2}$ represent the mean electron velocity. An important parameter related to the cross-section, is the mean free path which define the average distance transverse by particles between two subsequent collisions. The means free path λ and the cross-section $\tilde{\sigma}$ are generally defined by a simple relationship which treats the particles as impenetrable spheres. Thus, the λ for electrons passing through a gas of particle density N_0 can be expressed as

$$\lambda = \frac{1}{\sqrt{2}\tilde{\sigma}\, N_0} \tag{3.5}$$

Generally, this parameter can be also expressed with an inverse proportional relation to the partial pressure P of the plasma. Higher pressure infact means also high density on particle N_0, and thus a reduction of the mean free path.

3.1.1 DC and RF Glow Discharges

A glow discharge plasma is a low temperature, relatively low pressure, gas in which a degree of ionization is sustained by energetic electrons. Glow discharge configuration used in material processing differs in both their general geometry and in the orientation of the electric field that is used to provide energy to the electrons. The discharge may be driven by DC or radio frequency (RF) means, using a variety of electrode configurations. In case of RF activated plasma, the operating frequency is generally 13.56 MHz. At this frequency, only electrons can follow the temporal variations in applied potential. Thus the plasma can be pictured as an electron gas that moves back and forth at the applied frequency a sea or relatively stationary ions. As the electrons cloud approaches one electrode, it uncovers ions at the other electrode to form a positive ion sheath. The formation of the sheath voltage is described in detail later. The ions thus are accelerated by this voltage and bombard the electrodes [3.8].

The RF discharge can be further understood by examining the electrode current flow. These discharges are capacitive in nature, both because of the external capacitance which is placed in the electrical circuits and because one or both the electrode surfaces are generally non-conducting. These plasma sources are called capacitively coupled plasmas (CCPs). Consequently, the total ion and the electron charge flow to a given electrode during an RF cycle must balance to zero and a self bias that is negative with respect to the plasma potential develops on any surface that is capacitively coupled to a glow discharge [3.9]. The basis for this behavior is illustrated in Fig. (3.3), where the current/voltage characteristic are shown for as electrode immersed in a glow-discharged plasma. When an RF voltage signal is delivered to the electrodes, much larger currents are drawn when the electrode is positive relative to the floating potential than when it is negative, because of the mobility difference between the electrons and the ions. In order to achieve zero net current flow, it is necessary for the DC self-bias to develop such that the average potential is negative relative to the floating potential, as shown in the lower figure. This offset means the electrodes only minimally exceed the floating potential (and become anodes), for short portions of each RF cycle. Most of the time they are cathodes. Because the ions largely respond to the DC self-bias they flow to both electrodes throughout the cycle in quantities that are equal to the time-averaged electron flow [3.8].

RF discharges in planar diodes can be operated at considerably lower pressures than DC discharges. This is due to two reasons: a reduction in the loss of ionizing electrons and an increase in the volume ionization efficiency. In order to understand this, consider that a fraction of the ionizing electrons will be repelled from the electrode toward which they are accelerated as the cycle changes. Thus wall losses decrease, and electrons remain in the discharge longer to make additional ionizing collisions. In addition, electrons can gain energy from the RF field by making in-phase collisions with gas atoms. That is, if an electron, accelerated in one direction during a given half-cycle, makes an elastic collision in which its direction is reversed, it maintains most of its velocity due to the large mass mismatch between electrons and ions. If this happens near the end of the cycle, it will again be accelerated during the next half-cycle and thus have gained energy during the complete cycle. As the pressure is increased, collision probability increases and the volume ionization due to electrons accelerated by the oscillating electric field becomes increasingly important [3.8].

Additionally to the electric field , RF currents driven through coils will produce an alternating magnetic field, external to the coil, that can induce alternating currents in a gas. Plasma sources that rely on this type of energy transfer are called inductively coupled plasmas (ICPs) . An advantage of ICPs relates to the induced electron currents, which follow circular orbits in planes normal to the device axis. This motion limits the loss of electrons at the chamber walls. Thus, compared to CCPs, where the use of electrodes to deliver power further enhances wall losses, ICPs have plasma densities that are typically an order of magnitude greater than CCPs [3.8].

3.1.2 RF glow discharge breakdown

An important parameter for the plasma glow discharges is the degree of ionization R_i, which depends on a balance between the ionization rate caused by inelastic electron collisions and the rate at which particles are lost by volume recombination or by passage to the walls of the reactor

$$R_i \propto N_0 n_e \sqrt{\tilde{\sigma}_{ion}(E)} \tag{3.6}$$

where N_0 represent the particle density, n_e is the electron density, and $\tilde{\sigma}_{ion}(E)$ is the cross-section for the ionization process which is in general a function of the electron

energy. The rate of ionization thus depends on the type of the gas through the cross-section $\tilde{\sigma}_{ion}(E)$, on the electric field as it has influence on the electron density, and on the gas pressure through the particle density N_0. For most low-pressure configurations, the wall losses dominate over the volume recombination [3.8]. The degree of ionization have a deep impact also on the occurrence of the plasma ignition, i.e. *breakdown*, which thus depends strongly on the reactor geometry, the gas type and pressure, the electric field strength, and on the surface-to-volume ratio of the plasma [3.8].

In Fig. (3.4) are presented the experimental curves, known as Paschen curves, which define the minimum discharge breakdown potential for a DC glow discharge plasma as a function of the employed gas and a quantity pd which depends both on the chamber pressure p and the distance d between the two electrodes. The rise in voltage for lower pressure is mainly caused by the small volume-to-surface ration, i.e. the chamber is small so the electron losses due to interaction with the walls dominates over the ionization process. Otherwise, the pressure of the gas is too low, so the electron diffuse faster to the wall respect to the generation process though ionization. The epitaxial reactor chamber thus must be design properly in order to enhance the ionization processes over the losses due to wall interactions. The employment for example of quartz liner tubes, for plasma confinement and protection from wall coating during the deposition process, can lead to an high breakdown voltages requirement in case the deposited film is conductive. In these conditions infact, the electrons generated recombine with the quarz liner walls faster comparing to the ionization processes. On the other hand, similar condition are experienced in case of high gas pressure, where the mean diffusion length is too short and the collisions with gas atoms become so frequent that electrons lose energy faster than they can gain. Similarly, high breakdown voltage are also requested in very large chambers, where the local electric fields in the plasma are too weak to deliver sufficient energy to the electrons between collision, i.e. the electric filed are too weak to sustain the plasma over that volume of gas.

On the other hand, the breakdown for a RF discharge is related to the ability of the oscillating electric field increasing the energy of the electron sufficiently to produce the required amount of ionization which can balance the losses due to diffusion towards the chamber walls, the volume recombination, etc. If is considered the case in which the diffusion losses and the ions-electrons interaction dominate, then it is possible to balance the rate of ionization ν_i and the electron diffusion using the steady-state diffusion equation [3.8]

$$\nabla^2 n_e = (\nu_i/D)/n_e \tag{3.7}$$

where n_e is the electron concentration, and D is the diffusion coefficient for electrons. The expression for the collision frequency $\nu_i = N_0 \tilde{\sigma}_{ion} v$, where N_0 is the neutral species density and v is the velocity of the electrons, can be derived using the Eq.(3.2) and Eq.(3.4) assuming $N_0 \gg n_e$. By imposing the boundary equation $n_e = 0$ than results the solution

$$(\nu_i/D) = 1/\Lambda^2 \tag{3.8}$$

where Λ is a parameter that depends on the geometry of the reactor. Even in this case thus, the voltage breakdown requirements depends on the geometry of the reactor through the Λ parameter, the pressure of the ignition gas through the N_0 parameter which is contained in the collision frequency expression, and the electric field strength E through the expression of the D parameter.

3.1.3 Potentials in RF glow discharges

Several potentials are important in the glow discharges, such as the plasma potential, the floating potential and the sheat potential. The plasma potential V_p is the potential of the glow region of the plasma, which is normally considered nearly equipotential. It is the most positive potential in the chamber and is the reference potential for the glow discharge. The sheath potential V_s is instead caused by the interaction of the glow discharge with the any surface in contact with the plasma within the deposition chamber. Furthermore, both potential are mainly caused by the higher mobility of the electrons respect to the ions species. The V_p is infact always positive respect to any surface within the reactor, because the electrons diffuse faster to the walls surfaces respect to the ions. Therefore, the surfaces in contact with the plasma become negatively charged, and a positive space charge layer develop in front of the these surfaces. This process give rise to a potential difference V_s, called *sheath potential,* between the walls and the plasma. Because there are fewer electrons in the space charge layer, fewer gas species are excited by electron collisions. Consequently, fewer species relax and give off radiation, and the sheath region is dark relative to the glow discharge. Positive ions that enter the sheaths

from the glow region by random thermal motion accelerate into the electrodes and other surfaces in contact with the plasma. Similarly, secondary electrons emitted from the surfaces due to ion bombardment, accelerate through the sheath region into the glow region. The maximum energy with which positive ions bombard a surface, and the maximum energy with which secondary electrons enter the glow region, is determined by the difference between the potential of the surface and the plasma potential.

In case instead an electrically floating surface is considered, the voltage drop between the plasma potential V_p and the floating potential V_f can be calculated by imposing an equal impinging flux of positive and negative charges on the floating surface and assuming a Maxwellian energy distribution $f(E)$ [3.1]

$$V_p - V_f = \frac{kT_e}{2e} \ln\left(\frac{m_i}{2.3m_e}\right) \tag{3.9}$$

where T_e is the electron temperature, m_i and m_e are the masses of the ions and electron respectively, and e is the electron charge. This equation can be useful to estimate the maximum energy, given by $-e(V_p - V_f)$, at which ions may bombard an electrically insulated surface immersed in a plasma.

3.1.4 Qualitative PECVD deposition model

First, the plasma glow discharge is generated into the CVD reactor using an activating gas such as Ar or H_2 by means of a RF discharge. As described earlier, the free electrons are accelerated by the electric field and the avalanche ionization process begin. The rate at which ions and electrons energetic species are created is controlled by the bulk plasma parameters, such as the energy distribution $f(E)$ and the plasma density. These parameters can be tuned ‘ externally ‘ by means of process parameter such as the chamber pressure $\bar{p}$, gas flow, discharge excitation frequency, the RF power, which reflect on the ‘ internal ‘ plasma characteristics, particularly the electron plasma density, the electron energy distribution function, the electric potentials, and the fluxes of different species toward the surfaces exposed to plasma. For example, the $f(E)$ function have a strong influence on the chemically reactive species which are generated within the plasma environment, due to a different activation energy for each electron-molecular interaction process. As soon as the gas precursors are injected into the plasma glow, the inelastic

collisions with high energy electron provide the dissociation of the precursor molecules, with the consequent generation of highly reactive radicals. However, only a fraction of the total injected precursor is ionized, and thus the remaining ground state molecules follows a similar deposition process path which is common in the thermally driven CVD deposition, i.e. that is

- Mass transport of reactants to the wafer surface
- Adsorption of reactants
- Physical-chemical reaction yielding the epilayer and reaction byproducts
- Desorption of byproducts
- Mass transport of byproducts to the main gas stream
- Transport of byproducts away from the growth region

The key feature of the PECVD deposition technique instead is that in addition to these deposition steps, the plasma generate also reactive species, which also diffuse to the wafer surface and undergo to similar processes of adsorption, chemical reactions, surface migration, etc. Thus these highly reactive species follows an alternative deposition pathway which operate in parallel to the existing thermal deposition pathway. The plasma kinetics often bypass that of the ground state species because their sticking coefficient are closer to unity [3.2] and the activation energies are generally lower. The results is that plasma kinetic give rise to a deposition pathway which make possible high deposition rates. However, the substrate temperature is still a key parameter as provides the energy required to promote surface reaction and can thus be used as a tunable parameter which influence almost exclusively the epitaxial surface processes.

3.1.5 Plasma-surface interaction

Surfaces in contact with the plasmas are bombarded by slow and fast neutrals, electrons, ions, radicals, metastables, complex molecules, and photons. As described earlier, the establishment of a sheath potential between the plasma and the surface within the reactor chamber accelerate the ions towards the chamber walls promoting the ions bombardment. This process results in a possible liberation of neutral and charged species from the surface, as well as in a variation of the physical, electrical, and chemical properties of the surface. For example, the momentum exchange associated with ion bombardment can cause surface rearrangement, which can have dramatic effects on the structure and properties of a growing film [3.10]. The magnitude of the incident ion

energy depends on its transit trough the sheath region. If the mean free path for the ions is larger than the sheath region, than the energy of impact can be evaluate as the difference between the cathode potential and the plasma potential [3.8]. Contrarily, the ions collides with high probability with other ions or neutral species which result in a impact energy value considerably less than the potential drop across the sheath described by Eq. (3.6).

During the epitaxial deposition, ions bombardment can greatly influence the surface processes, such as adsorption, desorption and reactions of gas species. First it can caused adsorbed molecule to dissociate, thereby overcoming the activation energies for this process. This means that the substrate temperature requirement for promoting the dissociation and surface reactions are generally much lower respect to the thermally activated UHVCVD technique. In the field of $Si_{1-x}Ge_x$/Si heteroepitaxy, ions bombardment has been proved to great enhance the desorption of hydrogen from the substrate surface [3.11]. As described in Section 3.4.1, the hydrogen surface coverage can play a determinant role on the surface kinetics processes during epitaxy. Even at small coverage values infact, it have been shown to lower the surface diffusion of Si in low temperature MBE growth [3.12], leading to polycrystalline or amorphous epilayers. Furthermore, in thermally driven CVD deposition processes of Silicon and Germanium, the adsorbed hydrogen cause a severe reduction of the growth rate as the energetic barrier to adsorption is enhanced by the Si–H and Ge–H bonds. The employment of plasma glow discharges in epitaxial deposition processes instead, lead to a efficient hydrogen desorption as the energetic barrier is reduced by the collisions of bombarding ions. In PECVD reactors infact, a drastic reduction of the temperature combined with a constant glow discharge power do not affect sensibly the growth rate, while in principle would entail an higher hydrogen coverage. This means the hydrogen removal within the PECVD reactor must have non-thermal origin [3.13].

Additionally to ions, also electrons are responsible for substrate bombarding. As described earlier, the time-averaged flux of positively and negatively charged species to surface exposed to plasma is comparable. However, since the plasma potential is usually more positive than any other surface in contact, electron are tipically decelerated as they leave the plasma. Thus electron will impact on adjacent surfaces at relatively low energies compared to the ions. Nonetheless, electron irradiation can cause surface heating and promote chemical changes [3.8].

3.2 Inductive Coupled Plasma (ICP) sources

As described in section 3.1.1, two typologies of RF plasma glow discharge are commonly used in the microelectronics industry, i.e. the capacitively coupled plasma (CCP) and the inductive coupled plasma (ICP) sources. Although simple and inexpensive, the original CCPs had a number of disadvantages. For instance, the internal electrodes in CCPs introduced unnecessary impurities into the plasma. Futhermore, a change in the RF power results in a consequent variation of the both plasma density and the sheath drop, while varying the pressure results instead also in a change in the plasma chemistry. The high pressures also creates a dust problems. Negatively charged particulate of micrometer size or larger would form and be suspended above the substrate by electric filed, and these would collapse onto the wafer at plasma turn-off, thus contaminating the wafer surface. These problems are overcome in ICPs, which use an external coil, i.e. the 'antenna ', to introduce an electric field inside the chamber according to the Faraday's law. Two common typologies of ICP antenna shape is represented in Fig. (3.5), i.e. the planar and the cylindrical antenna coils.

When the RF current is applied to the antenna coil, the oscillating magnetic field generated induces an electric field inside the plasma by which the electron inside the glow discharge are accelerated. In case the spiral coil configuration is considered, the current-carrying plasma can be represented by an equivalent cylindrical work load of radius R with uniform temperature and electrical conductivity, represented in Fig. (3.8), while outside this region the gas is considered non-conducting. Based on the conventional induction heating theory, the application of an oscillating magnetic field results in the generation of eddy currents in the external cylindrical shell of the load. The electric field decay infact exponentially into the plasma, and thus can be expressed as $E = E_0 e^{-z/\delta_p}$, where z is the direction perpendicular to the coil and δ_p is the distance t which the power absorption is limited, i.e. called *skin* depth, and is a function of the oscillating frequency of the coil ω and the plasma dielectric function [3.8]. As described in Section 3.1.1, is it possible to define different skin depth expression as a function the balancing between the oscillating current coil frequency ω and the frequency of ionization ν_i [3.8, 3.14]

$$\delta_p \cong \left(\frac{m_e}{e^2 \mu_0 n_e}\right)^{1/2} \qquad \nu_i \ll \omega \qquad (3.10)a$$

$$\delta_p = \sqrt{2}c\left(\frac{\mu_0 m_e \nu_i}{e^2 n_e \omega}\right)^{1/2} \qquad \nu_i \gg \omega \qquad (3.10)b$$

where e is the electron charge, and μ_0 is the magnetic permeability of the vacuum. In a non-isothermal plasma with $n_e = 10^{10}$ cm^{-3}, $\nu_i = 10^9$ s^{-1}, and a frequency $\omega = 13.56$ MHz, the Eq.(3.10)b yield a skin depth of $\delta_p = 0.25$ m [3.14]. For a cylindrical coil configuration, it would thus expected that the power density is concentrated in a small region with thickness δ_p near the periphery. Since generally the skin depth is in the order of centimeter, and thus much smaller than the wafer to be processed, this configuration shold in principle give poor plasma uniformity along the wafer surface. Actually the opposite is true, and the parameters can be adjusted to have excellent uniformity across the wafer. In Fig. (3.7) are presented the measured profiles of the electron density n_e, the electron temperature T_e and the RF B_z field [3.15]. The RF field decays away from the wall, while the T_e peaks in the skin depth region as expected. However, the density n_e peanks instead near the axis of the plasma. Many theories have been developed [3.16] to explain this problem, which is called *anomalous skin depth,* but none have definitely physically explain it.

3.2.1 Equivalent circuit model

The principle of operation for an ICP source is schematized in Fig. (3.7) by means of the equivalent lumped circuit [3.17]. The spiral inductance L_c generated by the coil is driven in series-resonance with a capacitance C_T such that strong RF electromagnetic field is created near the coil. The plasma form in a region near this coil. An electron current flows through the conductive plasma region so as to oppose the RF magnetic field generated by the coil. The current flow in the plasma is modeled as a single-turn inductor L_p and electron collision are modeled as a resistance R_{pi}. Since the plasma glow discharge is near the coil, a mutual inductance M exists between the coil and the plasma inductance. Therefore, the circuit is equivalent to a non-ideal transformer with a coupling coefficient $k = M/(L_C L_P)^{1/2}$ [3.18]. The C_{P1} and C_{P2} capacities represent the parasitic capacitance between the coil and the plasma, and the plasma sheath act as a dielectric of this capacitance [3.19]. The L_c and R_{pi} plasma parameters can be calculated using a simple model shown in Fig. (3.8), in which the current $\tilde{I}_r$ flowing in N turn coils induce a current $\tilde{I}_P$ inside a single turn plasma skin. The plasma resistance R_P can be expressed as the ratio between the circumference of the plasma loop respect to cross sectional area of the loop

$$R_P = \frac{2\pi R}{\sigma_{dc} \cdot l\delta_p} \tag{3.11}$$

where R is the radius of the cylindrical plasma, and σ_{dc} is the electrical conductivity of the plasma which can be expressed as $\sigma_{dc} = e^2 n_{es}/m\,\nu_i$ [3.8]. On the other hand, the plasma inductance can be calculated as the ratio between the magnetic flux produced by the plasma current and the plasma current $\tilde{I}_P$ itself

$$L_P = \frac{\mu_0 \pi R^2}{l} \tag{3.12}$$

Where the magnetic flux $\pi R^2 \mu_0 \tilde{I}_P / l$ have been used. The coupling of the two inductances L_c and L_P can be expressed model the source as a transformer by considering only the inductance L_c and the equivalent plasma lumped circuit

$$\begin{pmatrix} \tilde{V}_{rf} \\ \tilde{V}_P \end{pmatrix} = \begin{bmatrix} L_{11} & L_{12} \\ L_{21} & L_{22} \end{bmatrix} \begin{bmatrix} j\omega \tilde{I}_{rf} \\ j\omega \tilde{I}_P \end{bmatrix} \tag{3.13}$$

where $\tilde{V}_{rf}$ is the voltage on the L_c inductance, while $\tilde{V}_P$ is the voltage drop on the plasma inductance L_P . By using the classic theory for the transformer coupling, it is possible to express the L_{11} and L_{22} autoinductances as ratio between the magnetic flux evaluated in each coil and the correspondent current, while the trans-conductances $L_{12} = L_{21}$ as the ratio between the magnetic flux in the equivalent coil of the plasma and coil current $\tilde{I}_r$

$$L_{11} = \frac{\mu_0 \pi b^2 N^2}{l} \tag{3.14}$$

$$L_{12} = L_{21} = \frac{\mu_0 \pi R^2 N}{l} \tag{3.15}$$

$$L_{22} = L_P = \frac{\mu_0 \pi R^2}{l} \tag{3.16}$$

where b is the radius of the ICP coil. The voltage drop across the plasma inductance can be derived by solving the equivalent circuit for the plasma, i.e. $\tilde{V}_P = \tilde{I}_P \cdot R_P$. Thus, it is then possible to solve for the impedance $Z_s = \tilde{V}_{rf}/\tilde{I}_{rf}$ seen at the ICP coil terminal

$$Z_s = j\omega L_{11} + \frac{\omega^2 L_{12}^2}{R_P + j\omega L_P} \tag{3.17}$$

Using Eq.(3.17), the right part of the circuit shown in Fig. (3.7), composed by the ICP inductance L_c and the equivalent L_P/R_P circuit for the plasma, can be simplified with the circuit schematized in Fig. (3.9)b. This one is composed by the equivalent resistance and inductance seen from the ICP plasma, derived respectively as the real part and the imaginary per of Eq. (3.17)

$$Re(Z_s) = R_s = N^2 \frac{2\pi R}{\sigma_{dc} \cdot l\delta_p} \tag{3.18}$$

$$Im(Z_s) = L_s = \frac{\mu_0 \pi R^2 N^2}{l}\left(\frac{b^2}{R^2} - 1\right) \tag{3.19}$$

The behavior of the R_s is strictly dependent on the electron concentration n_e through the σ_{dc} and δ_p parameters. In case high density plasma is considered, the value of R_s decrease with the electron density following the expression $1/\sqrt{n_e}$. On the other hand, in low density plasma the skin depth is bigger than the plasma size R and so R_s behave as $\propto n_e$. In Fig. (3.10) is plotted the value of R_s as a function of the electron density. Thus the power adsorbed by the R_s load of the plasma can be expressed as $P_{abs} = (1/2)|\tilde{I}_{rf}|^2 R_s$.

In order to maximize the power transfer between the RF power supply and the plasma, the output impedance of the RF power supply and the whole system impedance have to be matched. The RF power supply have a fixed output impedance Z_C, which is generally of about 50 Ω, while the impedance of the load changes as a function of many parameters, such as the geometrical design of the UHV chamber or the pressure and the gas species. Hence, a matching circuit is inserted between the RF supply by which it is possible to tune the impedance seen from the RF power supply so that it equals Z_C , i.e. the sum of the matching networks Z_N and the Z_s must be equal to the impedance of the RF power supply. By expliciting the Z_N and Z_s impedances and solving the equivalent circuit, the matching conditions can be expressed as

$$C_L = \frac{1}{Z_C \omega} \sqrt{\left(\frac{Z_C}{R_s} - 1\right)} \tag{3.20}$$

$$C_T = \frac{L_s}{\omega} - \frac{R_s}{\omega} \sqrt{\frac{Z_C}{R_s} + 1} \tag{3.21}$$

An analysis of Eq. (3.20) highlights that if the plasma have a load resistance greater than the Z_C, the RF power supply and the plasma load can not be matched only by adjusting the C_L or C_T values, while it is necessary a variation in the antenna geometry, i.e. for example decreasing the number of coils N. Furthermore, the Eq. (2.21) instead shows that matching a large area antenna inductance require an even lower value of the series capacitance C_T. However, too low C_T values enhance the influence of the non-controllable parasitic capacitance usually present between the ground and the coupling circuit, which result in problematic impedance capacitance. This problem can be overcome by introducing an inductance in parallel to the matching circuit.

3.3 Low Energy Plasma Enhanced Chemical Vapor Deposition (LEPECVD)

As described in previous sections, the employment of plasma glow discharge in epitaxial deposition processes can lead to several advantages respect to the thermally driven CVD technique. The generation of high reactive species resulting from the ionization of the precursor gasses for example, give rise to a kinetic deposition pathway which can greatly enhance the growth rate of the epilayer. Since the energy for precursors gas dissociation is supplied from the inelastic electron collision with neutral species, very low temperature epitaxial deposition can be performed without affecting sensibly the growth rate. However, the ion bombardment experienced by the wafer surface can lead to bulk damages when their energy is higher than a certain threshold value of 15 – 20 eV [3.20, 3.21]. A possible reduction of this effect can be achieved by the remote plasma-enhanced chemical vapor deposition (RPCVD), in which the wafer surface is prevented being in contact to the plasma glow discharge [3.22]. Otherwise, an electron cyclotron resonance source (ECRCVD) is often used [3.23] as it can ensure plasma glow discharge characterized by low potentials and thus consequently low ions energies. Nevertheless,

ions damages on substrate surface are not necessary excluded unless the substrate bias is controlled independently [3.24].

Among the other deposition techniques for in the field of Silicon and Germanium epitaxy, the low energy plasma enhanced chemical vapor deposition (LEPECVD) has been proved being possible to mantain the ions impact energy below the critical threshold energy for bulk damage [3.13, 3.25 – 3.28]. The process is based on a very-low-voltage arc discharge generated using a DC plasma source. The plasma source contains a Ta filament heated by a direct current, typically 130 A which is connected to an UHV growth chamber by a small orifice. The plasma is ignited by applying a voltage of 20-30 V between the grounded chamber walls and the hot filament. Its geometry is defined by a grounded anode in the lower part of the growth chamber and by a magnetic field, which is induced by a combination of coils and permanents magnets [3.28]. The Ar discharge gas is fed directly into the plasma source. The reactive gasses, i.e. SiH_4, GeH_4, H_2, PH_3, are injected into the UHV growth chamber by means of a dispersal ring placed few centimeters over the substrate. The substrate is kept at fixed potential respect to ground by means of an external power supply, while the temperature the wafer is modulated by radiative heating from a graphite heater.

The most important feature is represented by the fact that the growth rate do not depend sensibly from the substrate temperature in the range generally employed for silicon-germanium epitaxy, i.e. 300°C to 800°C. In Fig. (3.11) is represented the Arrhenius plot of the growth rate as a function of the inverse of the temperature in which the discharge power and the silane flow are fixed [3.25]. Three different regimes can be identified. Within the range of about 300°C to 600°C the growth rate is almost independent from the substrate temperature. Below 300°C, the growth rate increase drastically due to the adsorption and incorporation of the SiH_2 and SiH_3 radicals in the epilayer. As the temperature decrease infact, the desorption of these species become less efficient. In thermal CVD where there is no plasma, the dependence on the temperature is exponential in this range due to hydrogen adsorption whose coverage also vary exponentially with the temperature. On the other hand, for temperatures higher than 550°C the growth rate also increases exponentially. For the Germanium instead, the growth rate is limited by the adsorption and incorporation of GeH_2 and GeH_3 radicals for temperatures up to 400°C and thus the curve decreases as the temperature increases. In this case, the lack of intermediate regime can be addressed to the lower temperature of decomposition of

germane [3.25]. The XRD analysis of a $Si_{0.82}Ge_{0.18}$ grown at 600°C plotted in Fig. (3.13), show a well-defined layer peak and thickness fringes demonstrating the good quality of the SiGe/Si interface. The epilayer thus results pseudomorphic even if the grown thickness of 142.6 nm exceed the critical thickness expressed by the empirical People *et al.* [3.30] limit. Furthermore, the AFM scans reveals a RMS roughness of 0.08 nm.

3.3.1 LEPECVD reactor at University of Ferrara

An improved LEPECVD reactor have been developed at the University of Ferrara and installed within the Clean Rooms facilities. The reactor LEPECVD at the University of Ferrara is the results of a joint research project between the Physics Department of University of Ferrara, *DICHROIC CELL S.R.L.* and the CNR-INFM institute. In Fig. (3.14) is presented the schematized configuration of the LEPECVD reactor. In the previous configuration, the plasma glow discharge is ignited by a low-voltage DC arc-discharge plasma source. Although high quality results have been obtained employing this configuration, there are several drawbacks regarding the generation of the glow discharge by using a DC plasma source. Systems using an DC arc-discharge are infact hard to scale to large substrate of 300 mm and beyond, as it is difficult to achieve a high uniformity over a wide substrate area. The glow discharge generated within the source is infact in contact with the UHV growth chamber only through a small aperture with a diameter of 1 cm, and thus the source can be considered as puntiform. The magnetic fields induced by the coil and permanent magnets are used to focalized the plasma in an area which is typically smaller than the substrate surface, and this plasma focus is shifted rapidly over the surface area in order to simulate a constant plasma glow discharge. Deflection of the focalized plasma spot outside the wafer surface can improve the uniformity along the substrate, but also have worsening effect on the growth rate. There have been also attempts to improve plasma uniformity by replacing the original point source plasma with a broad-area source [3.31]. Plasma DC glow discharge suffers however of additional drawbacks. In case are present metallic part or thermionic emitters as for the arc-discharge DC plasma which are in direct contact with the glow discharge, these can be eroded during the chamber cleaning cycle in which corrosive gasses are usually employed. Similar issue is valid also for the anode or the metallic chamber walls in case of anode-less reactor design. The problem can be reduced using particular UHV chamber design, which however increases the complexity of the reactor and thus the overall cost.

Most of these issues have been solved employing a ICP plasma source. ICP plasma sources can be infact designed to achieve high uniformity even for 300 mm wafer application [3.32] and to reduce drastically the direct contact between metallic parts and the plasma glow discharge. As described in Section 3.1, the RF glow discharge allows to increase the plasma power discharge without affect drastically the energy of the ions, as only the electron which have small masses can follow the temporal variation of the electric field. The LEPECVD process developed at the University of Ferrara is based thus on a ICP plasma glow discharge with a RF frequency of 13.56 MHz and a maximum power discharge of 1.6 kW. The reactor have been designed for 4" wafers but it can be scalable for wafer diameter above 300 mm while maintaining high uniformity. The plasma glow discharge is ignited using Ar or H_2 gasses, which are injected directly into the plasma source. The precursors gasses SiH_4, GeH_4 and the dopant gasses PH_3 and BH_3, can be injected into the UHV growth chamber either through a dispersal ring placed few centimeters above the substrate or directly into the plasma source. The higher partial pressure generated by injecting through the dispersal ring give rise to high density low-energy plasma regions above the wafer surface which reduces both the bombarding ions energy and the diffusion pathway of the radicals toward the substrate. Each gas line is provided with electronic mass flow controllers (MFCs) which is capable of a maximum gas flow rate of 100 sccm. The wafer is held by means of a subsceptor made of Al_2O_3 or quartz and it is radiatively heated by a graphite element which is placed few centimeters above the substrate. This aspect is described in detail in the cap. 5. The UHV growth chamber is kept using a turbo molecular pump and a rotary pump at pressure of 10^{-8} mbar. A lock-load module which is in contact with the UHV chamber through a shutter valve, is employed as a pre-deposition cleaning chamber and it is kept at the pressure of 10^{-6} mbar by a turbo molecular pump and a scroll pump. The module is provided with several IR lamps which heat the sample in order to promote the desorption of water and other surface contaminants.

References

[3.1] B. Chapman, *Glow Discharge Processes,* John Wiley, New York, 1980

[3.2] M.J. Ran, *J. Vac. Sci. Technol.,* **vol.** 16 (1979), p. 420

[3.3] R. Reif, ' Plasma Enhanced Chemical Vapor Deposition of Thin Films for Microelectronics ', in *Handbook of Plasma Processing technology: fundamentals, etching, deposition and surface interactions,* edited by S.M. Rossnagel, J.J. Cuomo and W.D. Westwood, New York, Noyes Publications/William Andrew Publishing, 1990.

[3.4] J.E. Greene, S.A. Barnett, *J. Vac. Sci. Technol.*, **vol**. 21 (1982), p.285

[3.5] J.E. Greene, *Solid State Technology*, **vol.** 30 (1987), p. 115

[3.6] G. Turban, Y. Catherine, B. Grolleau, *Thin Solid Films,* **vol.** 60 (1979), p. 147

[3.7] S.C. Brown, *Basic Data of Plasma Physics*, MIT Press, Cambridge, MA, 1966

[3.8] S.G. Walton, J.E. Greene, ' Plasma in Deposition Processes ', in *Handbook of Deposition Technologies for Films and Coatings,* 4th ed.,edited by P.M. Martin, Oxford, William Andrew Publishing, 2010.

[3.9] H.S. Butler, G.S. Kino, *Phys. Fluids*, **vol.** 6 (1963), p. 1346

[3.10] J.E. Greene, S.A. Barnett, J.E. Sundgren, A. Rockett, *Ion Beam Assisted Film Growth,* Elsevier, Amsterdam (1988), p. 101

[3.11] C. Rosenblad, H.R. Deller, T. Graf, E. M[u]ller, H. von Kaenel, *J. Crystal Growth,* **vol.** 188 (1998), pp. 125-130

[3.12] D.J. Eaglesham, H.-J. Gossmann, M. Cerullo, *Phys. Rev. Lett.,* **vol.** 65 (1990), p. 1227

[3.13] C. Rosenblad, H.R. Deller, H. von Kaenel, *Mat. Sci. Engin. B,* **vol.** 58 (1999), pp. 76-80

[3.14] H. Conrads, M. Schmidt, *Plasma Sources Sci. Technol.,* **vol.** 9 (2000), p. 441-454

[3.15] J.D. Evans, F.F. Chen, *Phys. Rev. Lett.*, **vol.** 86 (2001), p. 5502

[3.16] V.I. Kolobov, D.J. Economou, *Plasma Sources Sci. Technol.*, **vol.** 6 (1997), R1

[3.17] R.B. Piejak, V.A. Godyak, B.M. Alexandrovich, *Plasma Sources Sci. Technol.*, **vol.** 1 (1992), pp. 179-186

[3.18] J. Hopwood, *J. Microel. Systems,* **vol.** 9 (200), pp. 309-313

[3.19] Y. Yin, J. Messier, J. Hopwood, *IEEE Trans. Plasma Sci.,* **vol.** 27 (1999), pp. 1516-1524

[3.20] Y. Chen, J.W. MacKay, *Phil. Mag.,* **vol.** 19 (1969), p. 357

[3.21] M.V. Ramana Murty, H.A. Atwater, *Phys. Rev. B,* **vol.** 45 (1992), p. 1885

[3.22] L. Breaux, B. Anthony, T. Hsu, S. Banerjee, A. Tasch, *Appl. Phys. Lett.*, **vol.** 55 (1989), p. 1885

[3.23] D.S.L. Mui, S.F. Fang, H. Morko[c], *Appl. Phys. Lett.*, **vol.** 59 (1991), p 1887

[3.24] H.-S Tae, S.-H Hwang, S.-J. Park, E. Yoon, K.-W. Whang, *Appl. Phys. Lett.*, **vol.** 64 (1994), p. 1021

[3.25] G. Pin, O. Kermarrec, G. Chabanne, Y. Campidelli, J.-B. Chevrier, T. Billon, D. Bensahel, *J. Crystal Growth,* **vol.** 286 (2006), pp. 11-17

[3.26] C. Rosenblad, T. Graf, J. Stangl, Y. Zhuang, G. Bauer, J. Shulze, H. von Kaenel, *Thin Solid Films,* **vol.** 336 (1998), p. 89-91

[3.27] C. Rosenblad, M. Kummer, H.-R. Deller, T. Graf, A. Dommann, T. Hackbarth, G. H[o]ck, E. M[u]ller, H. von Kaenel, *Mat. Res. Soc. Symp. Proc.*, **vol.** 696 (2002), N4.7.1

[3.28] C. Rosenblad, H.R. Deller, M. D[o]beli, E. M[u]ller, H. von Kaenel, *Thin Solid Films,* **vol.** 318 (1998), pp. 11-14

[3.29] R.G. Andosca, W.J. varhue, E. Adams, *J. Appl. Phys.,* **vol.** 72 (1992), p. 1126

[3.30] R. People, J.C. Bean, *Appl. Phys. Lett.,* **vol.** 47 (1985), p. 322

[3.31] H. von Kaenel, R. Haid, *System for low-energy Plasma-enhanced Chemical Vapor Deposition,* Int. Patent Appl. WO2006/0000846

[3.32] W.Z. Collison, T.Q. Ni, M.S. Barnes, *J. Vac. Sci.Technol. A*, **vol.** 16 (1998), p. 100

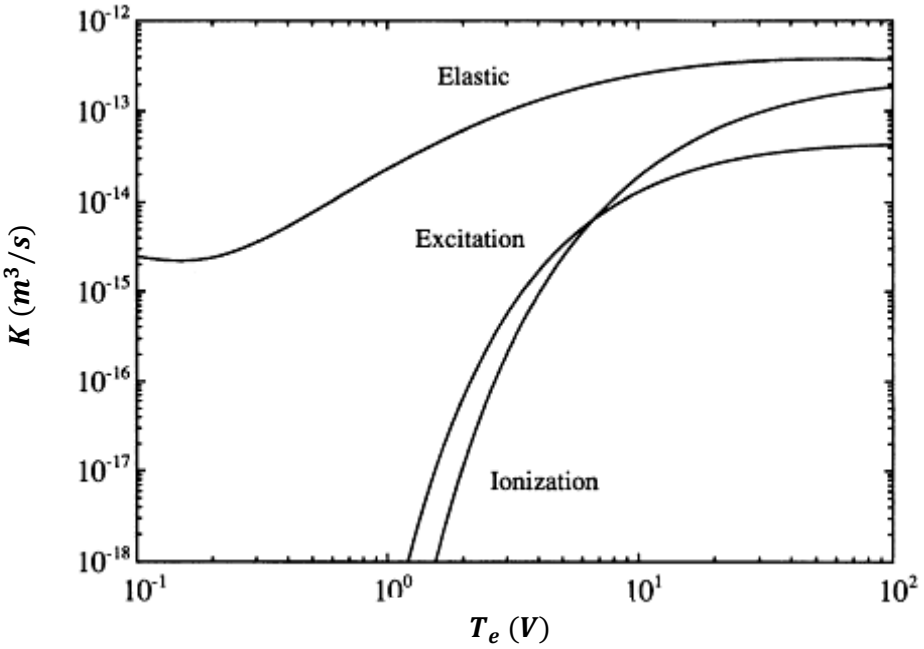

Fig. 3.1 Electron-Argon rate coefficients $\boldsymbol{k}$ for elastic and inelastic (excitation and ionization) collisions as a function of the electron temperature $\boldsymbol{T_e}$

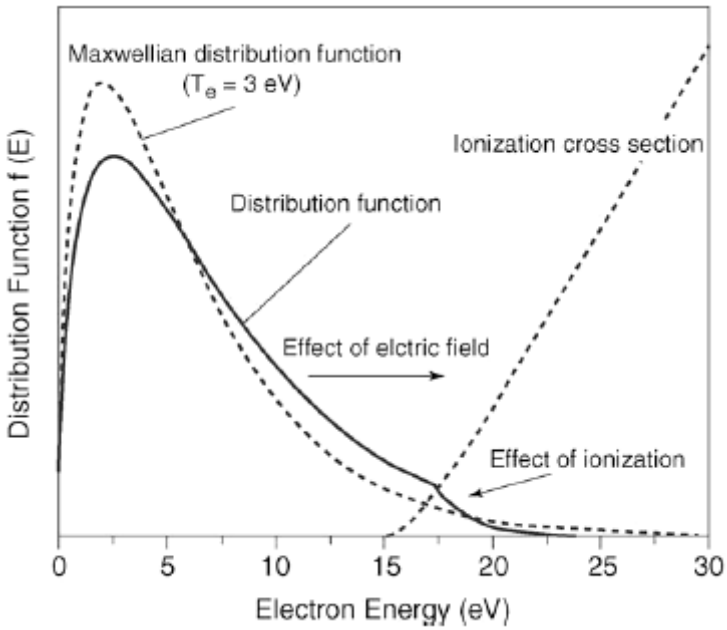

Fig. 3.2 Schematic representation of the electron energy distribution $\boldsymbol{f(E)}$ and inelastic ionization collision cross sectionin Argon. While the applied electric field tend to enhance electron energy, the inelastic collisions cause the depopulation of higher energies.

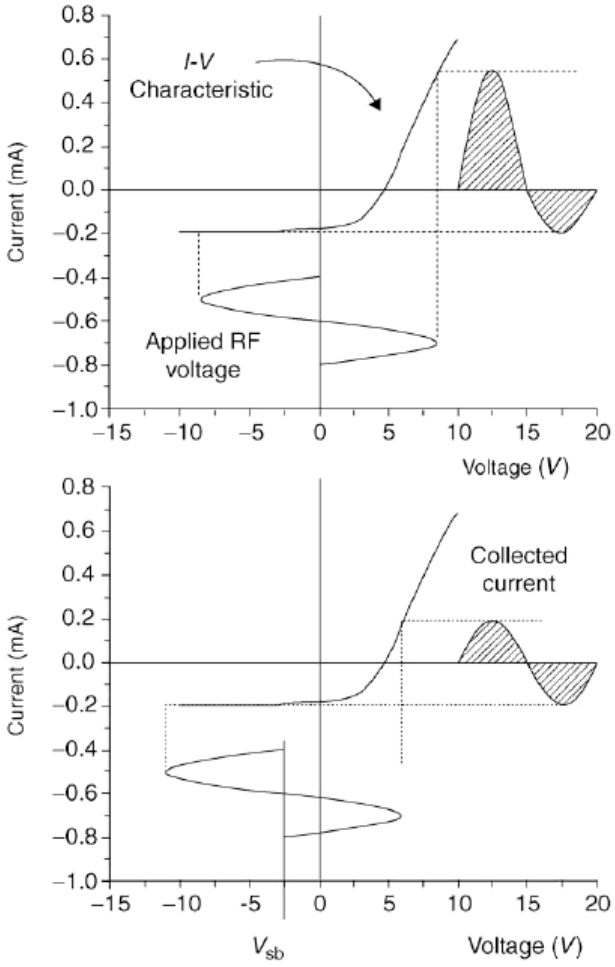

Fig. 3.3 Schematical representation of the self bias generation in a capacitively coupled plasma (CCP) RF discharge. The current-voltage I-V characteristic of the plasma defines the current collected at the electrode. In case of negligible bias voltage, the electron current is favored. For electron-ion balance, the surface must set ot a negative bias voltage

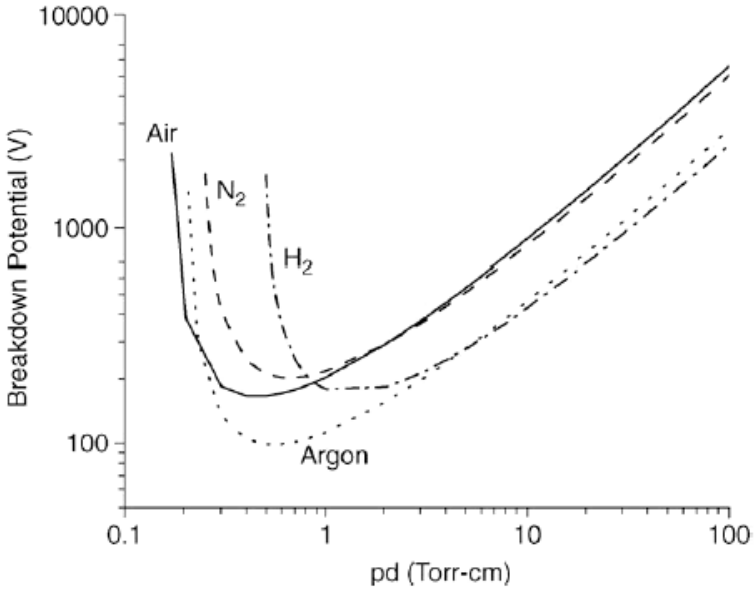

Fig. 3.4 Paschen curves for break down between parallel plates for Ar, N_2, Air and H_2.

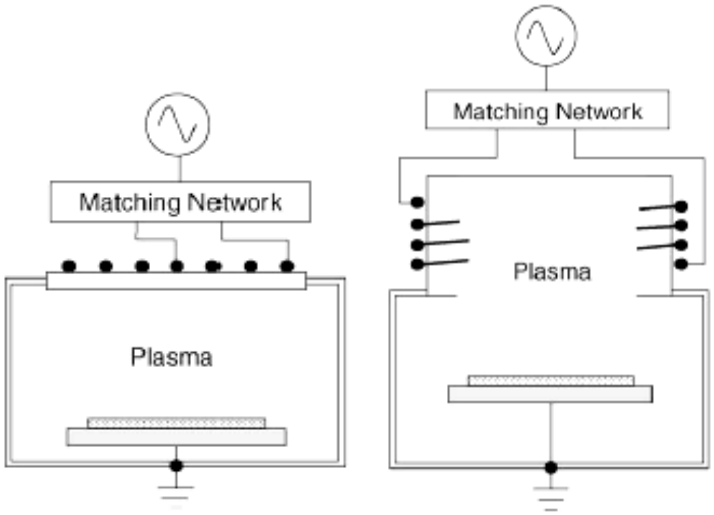

Fig. 3.5 Schematic representation of the two main configuration for the inductively coupled plasma (ICPs) sources. (*a*) Planar coil (*b*). Spiral coil

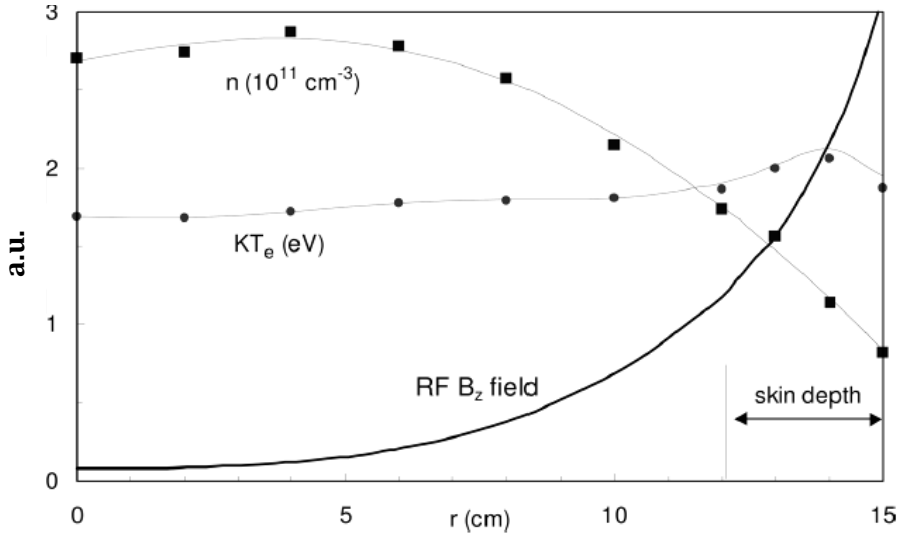

Fig. 3.6 Experimental measurement data plot of the electron density $\boldsymbol{n_e}$, electron temperature $\boldsymbol{T_e}$ and the $\boldsymbol{B_z}$ magnetic field as a function of the radial distance for a ICP plasma glow discharge.

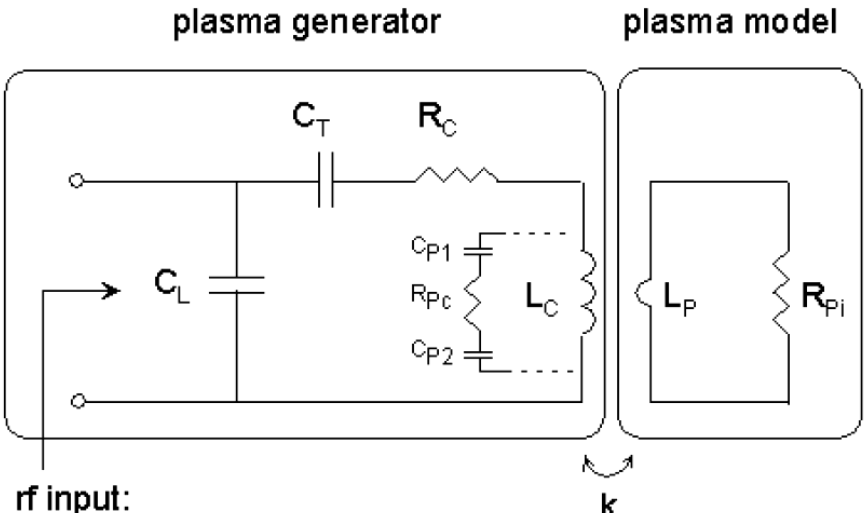

Fig. 3.7 Equivalent circuit for an inductively coupled plasma (ICP) source. The ICP source consist of an impedance matching network ($\boldsymbol{C_L}$ and $\boldsymbol{C_T}$) and the inductive coupler ($\boldsymbol{L_C}$). The plasma glow discharge instead is represented using a single loop inductance ($\boldsymbol{L_C}$) and a resistance $\boldsymbol{R_{Pi}}$.

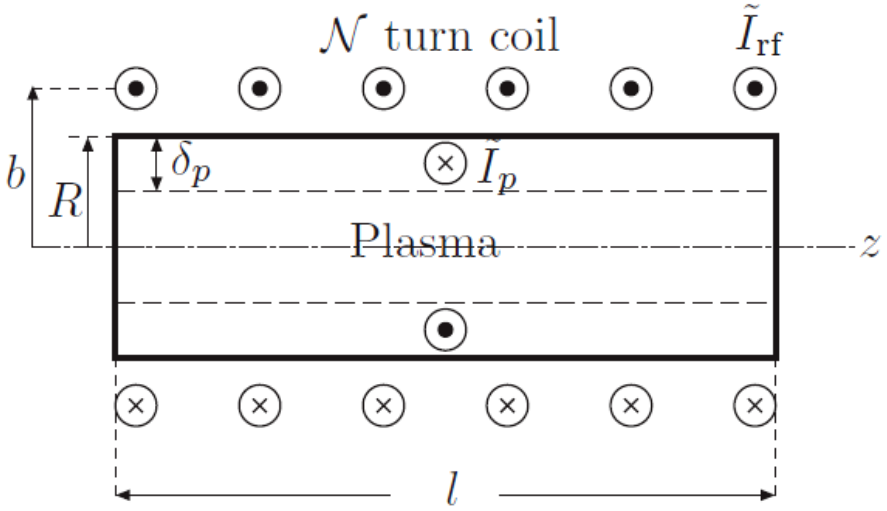

Fig. 3.8 Schematical representation of the ICP source – plasma coupling model. The ICP source inductance is represented by a spiral coil with radius $\boldsymbol{b}$ and $\boldsymbol{N}$ turns, while the plasma glow discharge is represented by a single coil with radius $\boldsymbol{R}$.

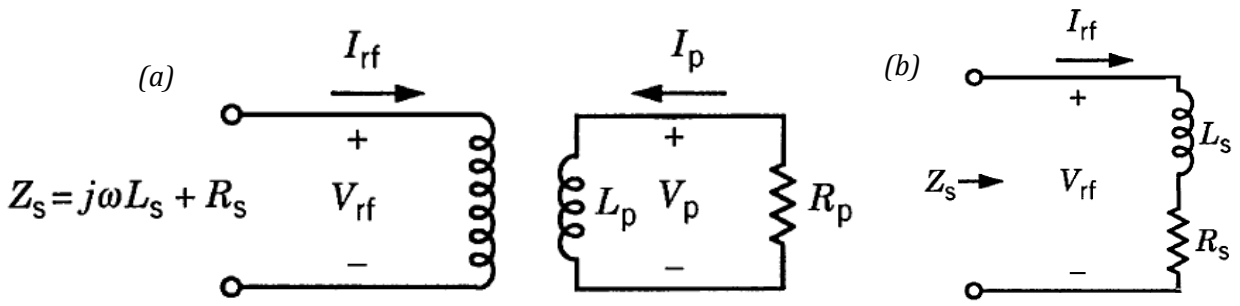

Fig. 3.9 (*a*). The equivalent circuit employed for the calculation of the impedance $\boldsymbol{Z_s}$ seen from the ICP source. (*b*). The equivalent circuit representing the total impedance $\boldsymbol{Z_s}$

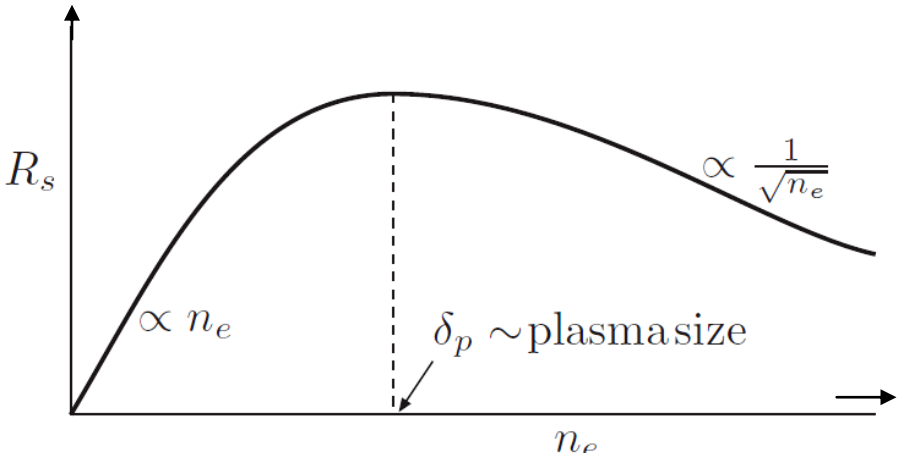

Fig. 3.10 Schematical plot of the $\boldsymbol{R_S}$ behavior as a function of the electron density $\boldsymbol{n_e}$.

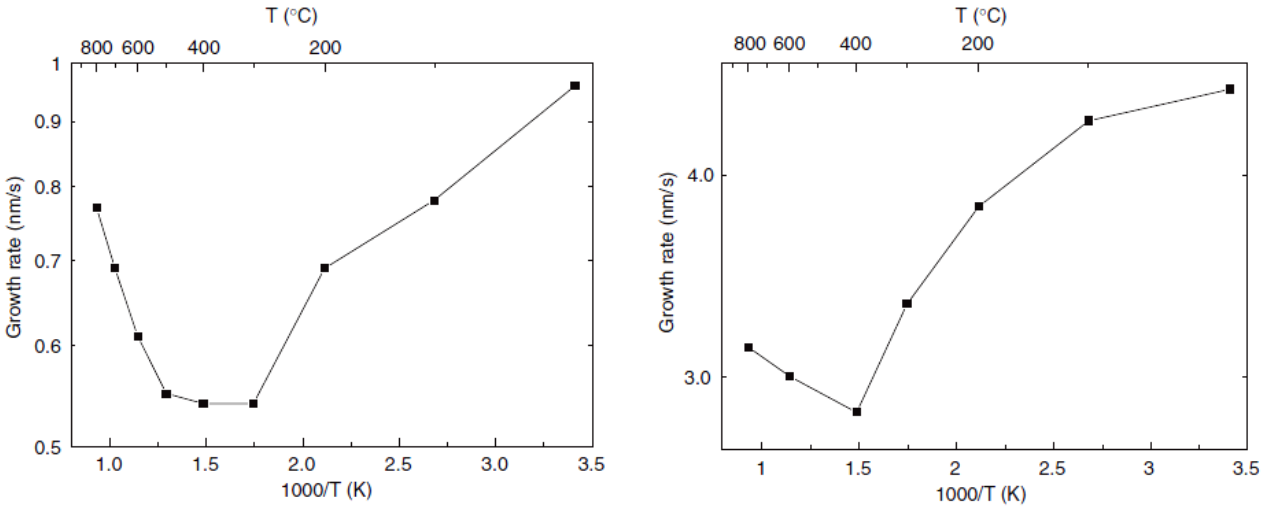

Fig. 3.11 The Arrenius plot of the growth rate for Si (*left*) and Ge (*right*) epitaxial deposition using the LEPECVD DC-arc plasma discharge technique. The GeH_4 and SiH_4 precursor are used [3.25]. See text for discussion.

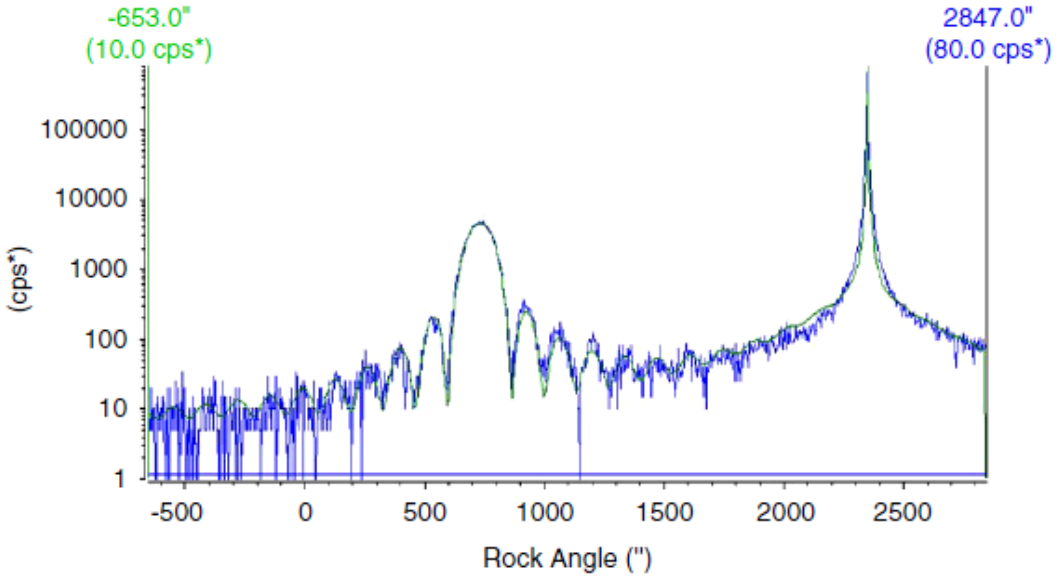

Fig. 3.12 HR-XRD $\boldsymbol{\theta/2\theta}$ (400) scans for a $Si_{0.82}Ge_{0.18}$ epilayer grown using the LEPECVD DC-arc plasma discharge technique. Even if the thickness of the epilayer is larger than the critical thickness calculated by People *et al.* [3.30], the rocking curve scan presents the interference fringes which suggest that the layer is pseudomorphic [3.25].

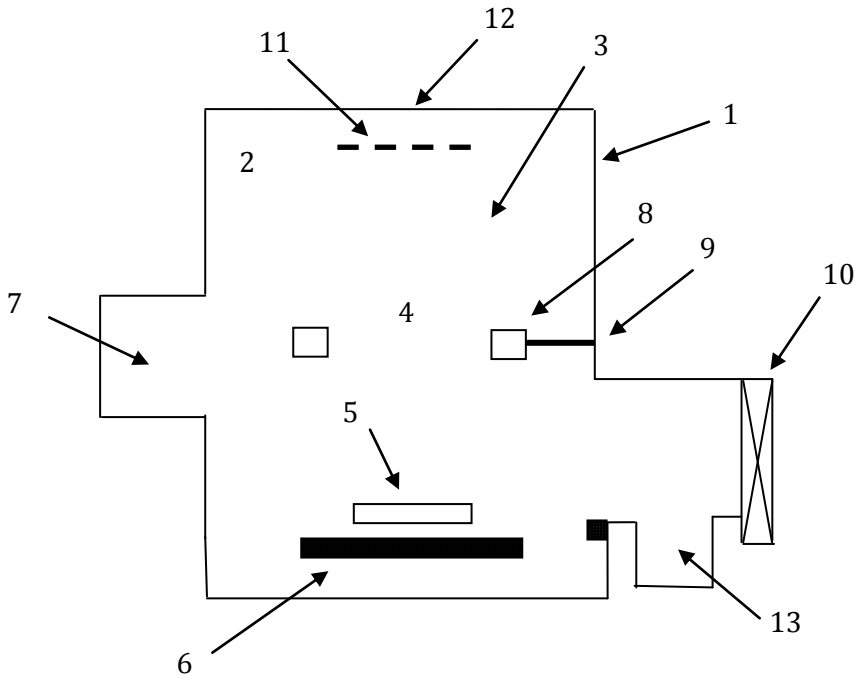

(1).Metallic vacuum vessel ***(2).***Vacuum chamber ***(3).***Quartz/ceramic enclosure ***(4).*** Deposition region ***(5).***Subsceptor ***(6).*** Indirect Wafer heating ***(7)-(13)*** Vacuum pump ***(8)-(12).*** Gas injection points ***(9).*** Gas inlet ***(10).*** Gate valve ***(12).*** ICP plasma source

Fig. 3.13 Schematic representation of the LEPECVD reactor developed at the University of Ferrara in collaboration with *Dichroic Cell s.r.l.* (*Courtesy of Dichroic Cell* ® - Patent WO2009024533A1)

CHAPTER 4
Wafer Heating Stage Thermal Model

4.1 Wafer heating model

4.1.1 Radiative heating model

The substrate temperature is one of the most important parameters because it influences all adatom processes of the surface, the crystalline growth, the surface morphology, the abruptness of doping transitions and the relaxation processes in the heterostructures. Due to UHV conditions, the wafer is radiatively heated from the backside by a current powered meander, which is typically made of high density (HD) graphite covered with a pyrolitic graphite coating. The spectrum of the radiation emitted by the heating element at a specific temperature, can be modeled using the Plank's radiation function for a blackbody at temperature T [4.1]. The wavelength correspondent to the emission peak for a given spectrum can be calculated using the Wien's displacement law

$$\lambda_{max} = \frac{2898}{T} \tag{4.1}$$

The total radiated power P from a blackbody at given temperature, integrated over the hemisphere can be calculated using the Stefan-Boltzmann radiation law

$$P = A\,\sigma T^4 \tag{4.2}$$

where A is the emitter area and σ is the Stefan-Boltzmann constant. The radiation law expressed by Eq. (4.2) apply to a blackbody, which is a perfect emitter. In case real material are considered, the emissivity function is included in the expression as they in general emit less radiation than a blackbody would at a given temperature. The emissivity of a medium is defined as the ratio of the radiation it emits to that emitted from a blackbody at the same temperature and in general is a function of the temperature T, wavelength λ, angle θ and polarization ϑ. Same considerations can be made for the radiative absorption of a material $a(\lambda, \theta, \vartheta, T)$, which results equal to the spectral emissivity for a given material and for the same parameters value as stated by the Kirchhoff's law. As it will be discussed in section [4.3], the spectral emissivity function for silicon has a strong dependence on the temperature and dopant concentration. Light doped silicon at 300 K for example is transparent for wavelength $\lambda > 1.1\mu m$, while results opaque only in shorter wavelength range. In these conditions, there exist only a small overlap between the spectral emission of the heater and the spectral absorption of the silicon. Even at a heater temperature of 970 K, the maximum of the emission for a blackbody has a wavelength of $3\mu m$, at which silicon is transparent. As the temperature increases, the absorption in the near-infrared region increase gradually due to enhanced free-carrier absorption processes and so the heating process become more efficient. Furthermore, a different spectral emissivity function can be defined for each material involved in the radiative heat exchange, that imply thus different thermal responses for same impinging radiation. The main issue of temperature control inside a vaccum chamber thus is that the wafer is generally much hotter than the chamber walls, while the heater element experiences generally higher temperatures respect to the other components. These temperature differences permit the rapid heating or cooling of the wafer, but they also have important consequences for the methods of temperature measurements and control [4.2].

Thermal modeling of the heating stage requires the calculation of power coupling and heat loss from any surface involved in the radiative heat exchange. In order to calculate the total amount of radiative energy reflected, transmitted, absorbed or emitted by any surface within the reactor (while taking into account the spectral distribution, the power absorption and thermal emissions) have to be described by quantities that average over the relevant ranges of wavelength and angle of incidence. The relevant spectral and angular ranges depends on the geometry of the system and the nature of the heat source. To integrate over direction, integration should be performed over both the angle of

incidence and the azimuthal direction. For example, to integrate the spectral directional absorbance [4.1]

$$a_\lambda = \frac{\int_{\phi_1}^{\phi_2}\int_{\theta_1}^{\theta_2} a_{\lambda,\theta}\cos\theta\sin\theta\, d\theta d\phi}{\int_{\phi_1}^{\phi_2}\int_{\theta_1}^{\theta_2}\cos\theta\sin\theta\, d\theta d\phi} \tag{4.3}$$

where ϕ is the azimuthal angle. By assuming that the surface is optically smooth, and that the material are optically isotropic, the dependence of the radiative properties on azimuthal angle is eliminated. Performing the integration over the angle of incidence θ yields

$$a_\lambda = \frac{\int_{\theta_{min}}^{\theta_{max}} a_{\lambda,\theta}\cos\theta\sin\theta\, d\theta}{\int_{\theta_{min}}^{\theta_{max}}\cos\theta\sin\theta\, d\theta} \tag{4.4}$$

Where integrating from θ = 0 to $\pi/2$ yield the total hemisphere properties. The resulting spectral absorbance a_λ is then integrating over the bands, where the a band is characterized by a spectral range and a characteristic temperature. It is assumed that the spectral distribution of the energy of incident radiation is the of a blackbody at the characteristic temperature. For example, the total absorptance of a surface i within the spectral bound λ_1 and λ_2 is given by [4.1]

$$a^i = \frac{1}{\sigma T_b^4 \gamma_{T_b}^m}\int_{\lambda_1}^{\lambda_2} e_b(\lambda, T_b)\, a_\lambda d\lambda \tag{4.5}$$

where e_b is the Planck function evaluated at the blackbody temperature T_b, and $\gamma_{T_b}^m$ is the fraction of the blackbody energy at the temperature T_b, in the spectral range m between bounds λ_1 and λ_2 . The integral is analogous for emittance, transmittance and reflectance. For calculating the absorbance, reflectance or transmittance of a surface with respect to the heater element radiation, evaluation should be performed using the Planck function at the heater temperature. For calculating the emittance of a surface, evaluation should be performed using the Planck function at the surface temperature.

The calculation of the total absorbance regarding the i^{th} surface would be the summation of all the radiations emitted by the other surfaces and the reflected radiation depending

on the particular geometrical set up of the environment. Furthermore, it is necessary to take into consideration of the shadowing effects that limit the total incoming radiation on the i^{th} surface, i.e. only a fraction of the emitted radiation power from the j^{th} surface reach the i^{th} surface as a function of the particular geometrical configuration of the heating stage. The widely used method to perform this evaluation is by introducing the *view factor* F_{ij}, which takes account of all the radiation which leaves surface i^{th} and strikes surface i^{th} [4.1]. Various analytical approaches have been developed in order to calculate the viewing factor for simple geometrical configurations, while in case of complex geometry the most implemented method is the Monte Carlo ray tracing, where the radiation transport equation is solved in a statistical averaging procedure [4.1, 4.3, 4.4]. The radiation is described by a radiative heat exchange matrix $\Phi_{ij}(T_b)$, which is calculated by Monte Carlo, where the i and j range over the N radiative surfaces areas of the reactor. This matrix is defined as [4.5]

$$\Phi_{ij}(T_b) = a^i(T_b)\Gamma_{ij}(T_b)e^j(T_b) - \delta_{ij}e^j(T_b) \tag{4.6}$$

where $\Gamma_{ij}(T_b)$ describes the fraction of the radiation emitted from the surface element j with the integrated emissivity $e^j(T_b)$ which is absorbed by the i surface with integrated absorption $a^i(T_b)$. These radiative exchange factors depend on the geometry of the chamber, the temperature-dependent optical properties and the reflection law of the surfaces. Both integrated emissivity $e^j(T_b)$ and $a^i(T_b)$ can be calculated using the Eqs. (4.3)-(4.4). The second term in the Eq. (4.6) describes the self-emission of the surface. By adopting a simplified 2D axisymmetric reactor model [4.6], it is now possible to express the differential equation which describes the steady state thermal behavior of the i surface inside the reaction chamber

$$k_i \nabla T_i \cdot \boldsymbol{n} = a_i^h \sum_{j=1}^{N_{s,m}} P\,\Gamma_{ij}^h(T_b) + \sigma \sum_{m=1}^{N_b} \left[a_i^m \sum_{j=1}^{N_{sw}} \gamma_{T_j}^m \varepsilon_j^m \Gamma_{ij}^m(T_b) T_j^4 - \gamma_{T_i}^m \varepsilon_i^m T_i^4 \right] \tag{4.7}$$

where k_i is the thermal conductivity of the material referred to the i^{th} surface, T is the surface temperature, $\boldsymbol{n}$ is the unit vector normal to the surface, a is the total absorbance, ε the total emittance, Γ_{ij} is the term of Eq. (4.6) which describes the fraction of the radiation emitted from the surface element j that strike the surface i, P is the total radiative power emitted from the heater element, σ is the Stefan-Boltzmann constant, $\gamma_{T_j}^m$ is the fraction of

the blackbody energy in the band m at temperature T_j, $N_{s,m}$ is the number of emitting surfaces on the heater, N_b is the number of bands excluding the heater band and N_{sw} is the number of surfaces excluding the heater surfaces. Superscript h indicates the heater band and m indicates bands for emission from all other surfaces. The term on the left side is the contribution of conduction of the material. The first term on the right gives the radiative input absorbed by surface i from the heater. The last term accounts for energy that is emitted from all other surfaces in the enclosure that is absorbed by surface i and the energy that is emitted from surface i^{th}. The radiative properties of all surfaces influence radiative exchange factors in each band because of multiple reflection in the chamber. Also, the radiative properties of surface i directly impact the energy balance through absorption and emission of radiation in each band. To solve for temperature fields, the knowledge of the radiative properties of all surfaces in each band is mandatory.

4.1.2 Wafer temperature uniformity

The uniformity is probably one of the issue having the strongest impact on the basic layout of a epitaxial reactor design. The move to larger wafer sizes also fundamentally clashes with the technology, because in general the heating element causes a higher temperature in the center of the wafer respect to the edges. The heat dissipation by thermal conduction process which arises in the contact region between the wafer and the holding elements, affects infact the temperature distribution decreasing the edge temperature and thus increasing the temperature gradient between the centre and the edge of the wafer. Furthermore, the spatial unevenness distribution along the wafer of the radiative power emitted from the heater modify the temperature profile enhancing or smoothing the thermal gradients. A simple 1D approximation of the steady-state temperature distribution along the wafer can be derived using a simplified form of Eq. (4.7) in which only the terms regarding the wafer and the heater element are used [4.18]

$$k_w d_w \nabla^2 T + \eta(x) P(x) - H_{eff}(x) \sigma T(x)^4 = 0 \tag{4.8}$$

where $\eta(x)$ is the power coupling efficiency between the heater and the wafer, $P(x)$ is the power density distribution, k_w is the thermal conductivity of the silicon, $H_{eff}(x)$ describe the efficiency with which power is lost by wafer through thermal radiation and d_w is the thickness of the wafer. Silicon is a good conductor of heat and lateral thermal conduction within the wafer smoothes out the temperature profile, reducing the non-uniformity. The

smoothing effect become stronger as the length scale become smaller. To simulate a discontinuity in the radiated heating power, a 1D sinusoidal modulation of the heater radiation flux incident on the wafer with period L is considered. In case the modulation is small compared to the average incident power, it is possible to linearize the Eq. (4.8) an solve respect to the modulation of the temperature [4.18]

$$\Delta T(x) = \frac{\eta \Delta P}{4T_0^3 \sigma H_{eff} + k_w d_w (2\pi/L)^2} \sin\left(\frac{2\pi x}{L}\right) \tag{4.9}$$

where ΔP is the module of sinusoidal power density and T_0 is the steady-state mean temperature. The expression shows that as the length scale L decreases, the non-uniformity decreases. In Fig. (4.1) are presented the calculations results using the Eq. (4.9) for a 1% sinosuidal modulation of the incident power required to keep the wafer various temperature, for a range of length scales L. As the length scales increases, the modulation approaches the value for no conduction within the wafer. The non-uniformity increase rapidly with the temperature because ΔP rises with T_0^4. The thermal conductivity of silicon also decreases rapidly, which makes non uniformity problem worse. For length scale below about 3 mm, non-uniformity is negligible for power changes < 10%.

The behavior is different in case the transient state is considered. During the ramp up and down in temperature, the non-uniformity problem is different because some of the energy is used to increase the wafer temperature, rather than just compensate the heat loss. This changes the spatial power distribution required for temperature uniformity. At the very first moment when the power is applied, there is very little heat loss from the wafer, because it is very close to the temperature of the other components in the chamber. In this conditions, temperature uniformity requires only that an evenness of the radiating power delivered from the heater element along the wafer surface. As the temperature rises, spatially inhomogeneous heat loss processes occur and so the radiative power distribution requirements for temperature uniformity changes. As a results, the illumination distribution requirements evolve as the wafer heats up. Furthermore, transition from the transient condition to the steady-state can take some time because of the time constant of the wafer. This could have a large impact on the epitaxial processes, in which frequently is necessary to vary the temperature of the wafer during the deposition process.

4.1.3 Contact Thermal Resistance (CTR)

Thermal contact conductance plays a key role in heat conduction mechanisms when the heat flow is interrupted by solid/solid interfaces. Particularly in a vacuum environment, accurate evaluation of the thermal contact conductance is mandatory in order to obtain high quality numerical results [4.7]. As schematized in Fig. (4.3)a, most engineering surfaces in contact exhibit both microscopic and macroscopic non-uniformities. The former are referred to as roughness, the latter arise from waviness and deformation of the bulk material. In this situation, heat flows experience two stages of resistance in series, i.e. the macroscopic constriction resistance R_L and the microscopic constriction resistance R_S [4.7, 4.8]. Thus, the total resistance R can be expressed as the sum of the two components. A model frequently employed to predict macroscopic constriction resistance is based on the Holm theory [4.9], in which the R_L value is related to a parameter r_L that represents the radius of the contour area. Although the expression is simple and straightforward, prediction of the contour area in a comprehensive manner, is a very complex task due to case-by-case nature of waviness and deformation of the substrate [4.7].

Nishino *et al.* [4.7] studied the thermal contact conductance in a vacuum environment in case of contact between a flat rough surface and an approximately spherical one, and between similarly flat rough surfaces as a function of the contact pressure. Respect to other similar works, the thermal constriction resistances R_L and R_S have been measured as a function of the contact pressure distribution, which have been assessed experimentally both for rough/spherical and rough/rough surfaces. In Fig. (4.3)b are presented the experimental results for the rough/rough contact thermal resistance which have been also compared with theoretical data. Contrarily to other case studies, in this particular configuration the experimental results show that the microscopic constriction resistance dominate over the macroscopic one, thus the confirming the low effective contact area between the two surfaces. Furthermore, the experimental measures show that the total constriction resistance decay exponentially with the contact pressure applied.

4.2 Temperature Measurements

Accurate wafer temperature measurement within reactor environment has turn out to be one of the most challenging problems for semiconductor processing technology over the

last decade. The request for wafer-to-wafer high repeatability and process control accuracy results in two fundamental technical problems. The first is that of making sure that the temperature distribution within any given wafer processed lays within a certain range. This issue of wafer uniformity, which have probably the most impact on the technological development of epitaxial reactors, have been discussed in Section 4.1.2. The second problem is that of ensuring that every thermal cycle is similar, regardless of the type of wafer being processed. The wafer itself is the most important and unpredictable variable within the reactor, as a result of its optical properties, which dominate its thermal response. Furthermore, the harsh conditions experienced inside the reactor has a deep impact on the technological issue for high accuracy measurement. The methods used must not only fulfill the requirements, but must also be simple to implement and calibrate, cost-effective and robust with respect to routine fluctuations in the process. Two type of temperature measurements are assessed below, which rely on the contact and non-contact temperature assessment techniques.

4.2.1 Pyrometry

Optical pyrometry deduces the wafer's temperature from the intensity of the thermal radiation it emits at a specific wave band [4.10]. The thermometer collects the incoming radiative energy by means of an optical system onto an electronic detector which has been accurately calibrated to produce a known between the radiative power intensity and the temperature reading. There are two major problems in this approach. The first is that the pyrometer can receive stray radiation from the heater and other system components that heat up during processing. The second difficulty is that the spectral emissivity of the wafer, which usually depends on temperature itself, must be know in order to correct for deviation of the wafer's emission from blackbody behavior. Furthermore, coatings on the wafer can radically change wafer's spectral emissivities and cause errors in the pyrometer readings [4.11]. The stray radiation can be minimized by various filtering methods, but an unknow target emissivity remains a problem. The error introduced when the spectral emissivity at the pyrometer wavelength λ_p, is incorrectly set at ε_a instead of the real value ε_r can be calculated as [4.12]

$$\frac{1}{T_a} = \frac{1}{T_r} + \frac{\lambda_p}{c_2} \ln\left(\frac{\varepsilon_a}{\varepsilon_r}\right) \tag{4.10}$$

where T_r is the real temperature, T_a is the measured temperature and c_2 is the Plank's second constant which has a value of 14.39x10^3 $\mu m\ K$ [4.12]. For small emissivity errors, $\Delta\varepsilon$, the trend of the absolute value of the temperature mismatch ΔT can be linearized using the expression

$$\Delta T \cong \frac{\lambda_p}{c_2} T^2 \frac{\Delta\varepsilon}{\varepsilon} \tag{4.11}$$

Here T is the absolute temperature and ε is the nominal wafer emissivity. This last expression shows that the error increase linearly with the emissivity error and rises with the square of the absolute temperature T. As an example, In Fig. (4.2) is presented the calculation of the absolute temperature mismatch ΔT for a 390 μm thick, highly doped and low doped silicon wafers as a function of the temperature within the range of 620 K to 1073 K. The calculation have been performed using the Eq. (4.11) using measured emissivities data for light and high doped silicon wafers [4.53] while assuming a wavelength λ_p of 950 nm. The variation of the emissivity for the highly doped silicon wafer is about 2% in that range, which result in a acceptable maximum temperature reading error of $\pm$1.85°C. On the other hand, the emissivity variations from 0.15 to 0.67 for lightly doped wafer within the same range, give rise to a maximum temperature error of about $\pm$90°C. The presence of a coating on the surface under measurement can also cause severe errors in optical temperature measurements due to coherent radiative interference effects which are described in detail in Section 4.4.1. In Fig. (4.4) is presented the error that would arise from the use of pyrometer which is set to assume that the wafer emissivity is that of plain silicon, for wafer coated with oxide films of varying thickness.

Although both Eq. (4.10) and Eq. (4.11) suggest that emissivity errors can be minimized by using the shortest wavelength possible, there are several other factors that influence the wavelength choice. The first aspect comes from the intensity of the thermally emitted radiation in that wavelength. The strength of the radiation influences the minimum temperature that can be detected and also the relative importance of any stray radiation that enters the pyrometer. The choice of wavelength thus always ends up being a trade-off between various aspects of the temperature range, stray-light elimination, emissivity-indipendence requirement, and signal detector capability. In the case of the silicon wafer, the measurements should be performed in the wavelength range below the 1.1 μm due to the semitransparent behavior experienced by silicon after this wavelength value. This

choice also allows an accurate measurements within the temperature range typical for the Silicon – Germanium epitaxial deposition processes, i.e. between 500 K and 1073 K.

4.2.2 Thermocouples (TCs)

Direct temperature measurement of the wafer temperature can be perform by physically embedding the TC junction within the wafer [4.24]. Although this method can provide convenient and accurate temperature reading in a wide variety of applications, its application is limited to calibration and setting up process recipes, while it is impractical for direct measurements during wafer processing. Various TC sensor can be also embedded onto the same wafer in different position of the wafer surface, so that the dynamic temperature non-uniformity can be assess during the process cycle. The creation of so called *instrumented wafer* is however a trivial task, because the temperature reported from the TC hot junction can differ from that of the wafer as a function of the method used for TC embedding. An improper soldering method can also influence of the temperature experience by the bare wafer as the TC itself can cause a thermal loss by thermal conduction with wafer surface. Nevertheless, recent evaluations of TC errors suggest that they are capable of about 3°C accuracy at 1000°C [4.14].

4.3 Silicon and $Si_{1-x}Ge_x$ radiative properties

Modeling of interactions of Silicon and $Si_{1-x}Ge_X$ alloys with radiation involve complicated functions of temperature, wavelength, doping level and strain. This variation is the results of three different absorption mechanisms, i.e. band gap transition, free-carrier and lattice absorption [4.15]. When photon energy is greater than the band gap energy of the semiconductor, electron in the valence band can be transferred into the conduction band. Therefore, at relatively short wavelengths (< 1100 nm for Silicon at room temperature) the band gap absorption dominates as the photons have enough energy to create electron-hole pairs.

On the other hand, free carriers are largely responsible for the absorption process at longer wavelength, in the near-infrared region, and this mechanism dominates where band gap absorption diminishes. The incoming radiation energy is absorbed by exciting electrons to a higher energy levels within the conduction band. In case an intrinsic silicon is considered, only thermally generated free carriers exist in the valence band (holes) or

conduction band (electron), with a concentration N_e less that $1x10^{10}$ cm^{-3} at 300°K [4.16]. In these conditions, radiative absorption due to free-carrier process results about more than 5 orders of magnitude less than band gap absorption [4.17]. As it will be discuss in detail in Section 4.3.1, absorption by this process increases rapidly as the temperature increases and the thermally generated electron and holes increase. For an heavily doped semiconductor instead, ionized donors or acceptors produce free carrier in addition to thermally generated ones, that can greatly enhance the free-carrier absorption in the near-infrared region.

At low temperatures there are also weak absorption features superimposed at the free-carrier background. These features correspond to lattice absorption that is caused by the weak photon-phonon interaction. This mechanism is significant only at high IR wavelength ($> 6\ \mu m$) and effects are swamped by free-carrier processes once the temperature exceed ~ 400°C [4.18].

The cumulative effect of the three absorption processes is that Silicon and $Si_{1-x}Ge_X$ are transparent in certain regions of the spectrum. In Fig. (4.5) is presented the absorption spectra of light-doped silicon for a range of temperatures and wavelength of interest of epitaxial growth processes. The high absorption coefficient for wavelength below 1100 nm is caused by the band gap absorption processes. This region correspond to the portion of the spectrum in which the silicon is opaque to radiation. As the wavelength increase, the energy of the photon decreases until it drops below the indirect silicon band gap. Above this limit that is called *absorption edge*, incoming radiation is absorbed only by the free-carrier and photon-phonon interaction mechanisms and the absorption coefficient experiences a rapid step decrease of magnitude inverse proportional to the doping level and temperature value. In this region, silicon is semitransparent to radiation.

In order to evaluate quantitatively the radiative properties of the silicon, a theoretical calculation of dielectric function that includes the three radiative absorption processes is mandatory. Once the complex function is known, it will be possible, as it is presented in Section 3.4, to evaluate the optical properties of the semiconductor wafers.

4.3.1 Silicon radiative properties model

Quantitative assessment of the radiative properties of a material can be calculated by deriving the complex dielectric function, which is related to the refractive index n and the extinction coefficient κ in the form

$$\varepsilon(\omega) = (n + i\kappa)^2 \tag{4.12}$$

Here, the real part is related to the phase speed of radiation propagating through the material, while the imaginary part takes account of the absorption losses and it is related to the absorption coefficient α by the expression $\alpha = 4\pi\kappa/\lambda$, where λ is the wavelength of the electromagnetic radiation. Despite the abundance of published work on the optical constants of single crystal silicon [4.20], a model which is valid over the full spectrum, temperature and dopant concentration ranges relevant for rapid thermal processing does not exist, while otherwise there exist various experimental measurements, models and correlations for the optical constants for specific spectral, dopant concentration and temperature ranges [4.20]. Definition of the variable ranges involved in this work is thus mandatory. Model should be valid for temperature range between 300 K and 1170 K, which correspond to the relevant range for $Si_{1-x}Ge_X$/Si, Ge/Si and silicon homoepitaxy deposition processing. In order to take account of the 99% of the radiation emitted by the heater element in this range of temperature, is necessary that the optical model should be defined in the wavelength range of 0,3 – 20 μm. Model finally, should be valid for doping level of up to 10^{20} cm^{-3}, which includes the whole range of wafer resistivities used in this work.

In order to derive the expression of the complex dielectric function for silicon which includes all the three absorption processes described earlier, a semi empirical expression valid for both intrinsic and doped silicon, is shown in Eq. (4.13), in which the doping effects are taken into account employing the Drude model [4.17][4.20]

$$\varepsilon(\omega) = \varepsilon_{bl} - \frac{N_e e^2/\varepsilon_0 m_e^*}{\omega^2 + i\omega/\tau_e} - \frac{N_h e^2/\varepsilon_0 m_h^*}{\omega^2 + i\omega/\tau_h} \tag{4.13}$$

Where the term ε_{bl} accounts for all absorption mechanisms but free-carrier absorption, i.e. the band gap absorption and the lattice vibrations, while the second and third terms

are the Drude terms for transition in the conduction band and valence band respectively. Here, N_e and N_h are the electrons and holes concentrations, m_e^* and m_h^* are the effective masses, τ_e and τ_h are the scattering times for free electrons and holes respectively, e is the electron charge and ε_0 is the permittivity in free space. For simplicity, the effective masses are considered to be independent of the frequency, dopant concentration and temperature, and their valued are $m_e^* = 0.27m_0$ and $m_e^* = 0.37$, where m_0 is the electron mass in vacuum [4.21].

Since ε_{bl} accounts for all contribution other than the free carrier absorption, it can be determined from refractive index and extinction coefficient of the silicon using Eq. (4.12) and assuming that no free carriers exist [4.20]. When considering the contribution from the transition across the band gap, the modification of the band gap by impurities is neglected and this approximation should not affect the significantly the results [4.22]. The refractive index n_{bl} in the wavelength range between $0.24\mu m$ and $0.84\mu m$ is calculated using the expression derived by Jellison and Modine [4.23], which highlights a linear dependence on temperature up to 763 K. They also estimate that this correlation should remains valid for temperatures as high as 1400 K. At wavelength longer than $1.2\mu m$, refractive index is calculated using the Li's expression [4.24], which has been developed for temperature values up to 753 K, even though Timans [4.20] has shown that is good up to 1073 K and wavelengths longer than $1.1\mu m$. In the wavelength between $0.84\mu m$ and $1.2\mu m$, a weight average based on the extrapolation of above two expressions is suggested by Lee *et al.* [4.25] that results extremely similar to the correlation proposed by Magunov [4.26]. The latter have been derived measuring the refractive index at wavelengths $1.15\mu m$ to $3.39\mu m$ for temperatures between 300 K and 700 K, even though Timans [4.27] demonstrates experimentally that this correlation extrapolates well to temperature of 1073 K and wavelengths of $0.9\mu m$ to $2.4\mu m$. When $\lambda > 10\mu m$, it is assumed that n_{bl} is independent of the wavelength and the value calculated by Li at $\lambda = 10\mu m$ is used to represent the refractive index in above this value. In Fig. (4.6) are plotted the calculated refractive index n_{bl} of silicon in the wavelength range of $0.3\mu m$ to $5\mu m$ for various temperatures by combining the empirical expressions listed above. The equations used [4.23][4.24][4.25] give a continuous curve of refractive index as a function of wavelength that can be extended up to $14\mu m$. All told, the refractive index value decrease slightly as the wavelength increase and increase monotonically as the temperature increase.

The extinction coefficient κ_{bl} accounts for the band gap absorption as well as the lattice absorption. The band gap absorption mechanism occurs when the photon energy is greater that the ban gap of silicon and result in a high absorption coefficient. For wavelengths $\lambda < \lambda_g$, where λ_g is the wavelength of the photon whose energy corresponds to the band gap energy, κ_{bl} is calculated using the expression of Jellison and Modine [4.23] which is valid in the range of $0.4\mu m$ to $0.9\mu m$ and for temperatures up to 1400 K as for the refractive index value. For wavelengths $\lambda > 0.9\mu m$ and temperature range of 573 K to 1073 K, the expression suggested by Timans [4.28] is employed. The extinction coefficient is derived through the evaluation of the absorption coefficient α_T by calculating the interband transition component suggested by MacFarlane *et al.* [4.30]. The contribution to the absorption coefficient which arises from interband transitions α_{BG} is described by the relation

$$\alpha_{BG}(\lambda, T) = \sum_{i=1}^{4} \left(a_{e,i}(\lambda, T) + a_{a,i}(\lambda, T) \right) \tag{4.14}$$

Here $a_{e,i}(\lambda, T)$ and $a_{a,i}(\lambda, T)$ are the components associated to the absorption and emission of the i th phonon respectively. The two of them are involved in the band gap transition processes, as silicon is an indirect band gap semiconductor. The sum is taken over the four types of phonon-assisted absorption processes described by MacFarlane [4.30] and subsequently identified by McLean [4.31]. The four phonon energies involved were found to correspond to temperatures of 212 K, 670 K, 1050 K and 1420 K. Detailed expressions of the two components can be found in Ref. [4.28]. The variation of the bang gap energy value with the temperature is calculated using the expression [4.32]

$$E_g(T) = E_{g0} - AT^2/(B + T) \tag{4.15}$$

where A = 4.73x10^{-4} eV/K, B = 635 K and E_{g0} = 1.155 eV as suggested by Jellison and Lowndes [4.32]. On the other hand, the lattice absorption occurs in the wavelength range between $6\mu m$ and $25\mu m$. Since the effect of lattice absorption is negligible in most of RTP applications compared to the absorption by free carrier, it is assumed to be independent of the temperature and dopant concentration. To account the effect of lattice absorption, κ_{bl} is obtained from tabulated extinction coefficient that can be found in Ref. [4.33]

Once ε_{bl} is determined, the remaining unknown parameters in the Eq. (4.13) of the complex dielectric function $\varepsilon(\omega)$ are the carrier concentrations N_e and N_h, and the scattering times τ_e and τ_h, which have generally a strong dependence on temperature and doping level. The carrier concentration can be calculated using the following equation by supposing known the Fermi energy E_F [4.34]

$$N_e = N_C F_{1/2}\left(\frac{E_F - E_g}{kT}\right) \tag{4.16a}$$

$$N_h = N_V F_{1/2}\left(\frac{-E_F}{kT}\right) \tag{4.16b}$$

Here, N_C and N_V are the effective density of states in the conduction band and valence band respectively, $F_{1/2}$ is a Fermi-Dirac integral of order$^1/_2$, E_g is the band gap energy of silicon and k is the Boltzmann constant. Variations of the band gap energy values due to temperature changes has been taken into account using Eq. (4.15), while effective density of states values of N_C = 2.86x10^{19} cm^{-3} and N_V = 2.66x10^{19} cm^{-3} with a temperature dependence of $T^{1.5}$ is used [4.35]. The Fermi-Dirac integral $F_{1/2}$ can be conveniently simplified by an exponential function, while the detailed description of the procedures to determine the Fermi energy E_F can be found in Ref. [4.34]. In this calculation, the ionization energy of the considered impurity or dopant is required. Phosphorus and Boron are considered as the *n*-type and *p*-type impurities respectively, for which values of 44 meV and 45 meV are used [4.35]. The resulting carrier concentrations N_e and N_h derived using this calculation has been proved being affected by an error of 3% respect to the values obtained by numerical integration [4.17]. The calculated carrier concentration N_e for *n*-type silicon are plotted in Fig. (4.7) versus the temperature for various doping levels. For intrinsic silicon, only thermally generated electron are present in the conduction band, and its concentration is about 10^8 cm^{-3} at 300 K and 10^{18} cm^{-3} at 1000 K. For increased doping level, the density of carrier introduced by donor dominate for low temperatures, so the carrier concentration curve in this region have a constant value correspondent to the donor concentration. At a certain point correspondent to the temperature at which the thermally generated carrier density is comparable with the donor concentration, the curve deviates from being constant following the intrinsic silicon curve, after which thermal generation processes dominate the carrier density as the temperature further increases. This is valid for doping levels less than 10^7 cm^{-3}. For larger donor concentrations, thermally generated electrons do not influence significantly the

carrier concentration density in the selected temperature range of 300K to 1000 K, which hence can be considered as independent of the temperature.

A real challenge is represented by the assessment of the electrons and holes scattering times as a function of the temperature and doping level. In this work the theoretical approach employed by Lee [4.17] is used. Electrons and holes in a single silicon crystal can scatter with lattice vibration and ionized impurities. The total scattering time which consists of the above two mechanism can be expressed as [4.35]

$$\frac{1}{\tau_e} = \frac{1}{\tau_{e,l}} + \frac{1}{\tau_{e,d}} \tag{4.17}$$

where $\tau_{e,l}$ and $\tau_{e,d}$ are the electron-lattice and the electron-defect scattering time respectively. The same correlation can be expressed for the hole scattering time τ_h and the two components $\tau_{e,l}$ and $\tau_{e,d}$. The first step is to evaluate the scattering time at room temperature τ_{e0} as it is influenced mostly by the dopant concentration. Derivation can be performed using the relation between the scattering time and the carrier mobility μ [4.36]

$$\tau = \frac{m^* \mu}{e} \tag{4.18}$$

Combined with the fitted mobility equation at room temperature as a function of the dopant concentration [4.37]

$$\mu_e^0 = \frac{1268}{1 + (N_D/1.3x10^{17})^{0.91}} + 92 \tag{4.19a}$$

$$\mu_h^0 = \frac{447.3}{1 + (N_A/1.9x10^{17})^{0.76}} + 47.7 \tag{4.19a}$$

where N_D or N_A represent the donor or acceptor concentration expressed in cm^{-3}. On the other hand, the scattering time from lattice contribution at room temperature $\tau_{e,l}^0$ and $\tau_{h,l}^0$, which is independent of the dopant concentration, can be separately obtained from the room temperature lattice mobility of 1451 $cm^2V^{-1}s^{-1}$ for electron or 502 $cm^2V^{-1}s^{-1}$ for holes [4.38] using Eq. (4.18). Consequently, the scattering time contribution $\tau_{e,d}^0$ and $\tau_{h,d}^0$ due to impurities can be derived easily by means of Eq. (4.17) knowing the total scatter time and the lattice vibration contribution. At room temperature, the scattering process is dominated by lattice scattering for lightly doped silicon, and the impurity scattering becomes important for heavily doped silicon when the dopant concentration exceeds 10^{18}

cm^{-3} [4.17]. The second step is to assess the temperature dependence of the total scattering time. The theory predicted that the carrier-impurity scattering times vary with $T^{1.5}$, and the carrier-lattice scattering times due to acoustic phonons vary with $T^{-1.5}$ [4.35]. As the temperature increase, the scattering rate $(1/\tau)$ due to impurity tends to decrease because the electrostatic force governing dopant sites becomes weaker and carriers can move agilely. On the other hand, the carrier-lattice scattering rate increases as the temperature goes up because of the increased phonon density of states. Therefore, lattice scattering dominates the scattering processes at high temperatures even for heavily doped silicon. Because of the relatively insignificance of impure scattering at high temperatures, the following expression is used to calculate the impurity scattering times

$$\frac{\tau_{e,d}}{\tau_{e,d}^0} = \frac{\tau_{h,d}}{\tau_{h,d}^0} = \left(\frac{T}{300}\right)^{1.5} \tag{4.20}$$

The temperature dependence of $\tau_{e,l}$ and $\tau_{h,l}$ can be more complicated since optical phonon modes may contribute to the scattering in addiction to acoustic phonon modes. The expressions of the scattering times for electrons and holes is derived by modifying the experimental fitting of the mobility due to lattice scattering in the work of Morin and Maita [4.38] in order to obtain a better agreement of the calculation results with the measured near-infrared absorption coefficient data for light doped silicon [4.20,4.22,4.19]

$$\tau_{e,l} = \tau_{e,l}^0 (T/300)^{-3.8} \tag{4.21a}$$

$$\tau_{h,l} = \tau_{h,l}^0 (T/300)^{-3.6} \tag{4.21b}$$

Substituting the Eqs. (4.20) and Eqs. (4.21) into Eq. (4.17) it is possible to obtain the scattering time for any temperature and doping concentration values.

Calculations of the total electron scattering times τ_e for a *n*-doped silicon by means of the theoretical approach described before are plotted versus temperature values for different donor concentrations in Fig. (4.8)a. In the first part of the curve, which is related to low temperatures, the doping level has a strong influence on the scattering time, that decreases as the donor concentration increases. For a dopant concentration of 10^{20} cm^{-3} and room temperature for example, the total scattering time reaches a value of 1.2×10^{-14} s, that is about 17 times less than the value for the 10^{15} cm^{-3} at the same temperature. As the temperature increases, the curves of different doping levels decrease overlapping after a

temperature of about 800 K are reached. After this value, the doping level has no significant effects on scattering time, which imply a dominance of the electron-lattice scattering processes over the electron-impurities contribution at this temperature range. The calculated scattering time is compared for verification in Fig. (4.8)b with measured data from other publications [4.21, 4.39, 4.40] by plotting the results versus dopant concentration at room temperature. For high doping level, the theoretical results fit reasonably well with the measured data, thus confirming the adopted theoretical approach as a good approximation.

Further verification of the model is performed by comparing the calculated absorption coefficient α for lightly doped silicon with measured datas at different temperatures, plotted in Fig. (4.9)a. At room temperature, theoretical results are compared with data extracted from the work of Edwards [4.33], showing a very good correspondence in the wavelength region in which band gap absorption is the dominant process. For comparison purpose, in Fig. (4.9)b are plotted the results of semi-empirical model proposed by Timans [4.28] for lightly doped silicon with experimental measurements of absorption coefficient at high temperatures. At temperatures higher than 600 K, calculation results for light dope silicon are compared with measurement data performed by Rogne [4.19]. In this range of temperature, the agreement is not so good as the empirical model proposed by Timans [4.28], which includes a contribution due to free carrier processes in the expression of the absorption coefficient α_T based on the works of Sturm and Reaves [4.29] and Vandenabeele and Maex [4.41]. Validity of this empirical model however is restricted only for lightly doped silicon and within a wavelength range between $0.9\mu m$ and $9\mu m$. Nevertheless, the theoretical calculation based on Drude model has been found to give results with very good approximations for a wide value ranges of temperature and dopant concentration parameters. Also the comparison at specific wavelength of the absorption coefficient as a function of dopant concentration and temperature with measured data by Strum and Reaves [4.29] shows a very good agreement [4.17].

Finally, the overall refractive index n and extinction coefficient κ of silicon are calculated by substituting the theoretical results described above into Eq. (4.13). In Fig. (4.10) are plotted the optical constants of *n*-type silicon versus the wavelength for different temperature and dopant concentration values. Calculation results show that refractive index of lightly doped silicon, i.e. with dopant concentration $\leq 10^{15}$ cm^{-3}, decreases as the wavelength increases, reaching a constant value for $\lambda > 10\mu m$. In these conditions, the

influence of the donor or acceptor concentration have negligible effects on the refraction index, which can be described using the semi-empirical approximation employed for the ε_{bl} term. For higher doping level, the refractive index first decrease reaching a minimum at a particular wavelength, and than it increases rapidly towards longer wavelengths. This trend agrees with the measured results [4.42]. On the other hand, the extinction coefficient results show a strong dependence on dopant concentration at long wavelength, where the free-carrier absorption is dominant. For fixed temperature, doping effects start to influence the absorption coefficient at dopant concentration values which increase proportionally with the temperature. The cause of this trend can be derived from Fig. (4.7). For a certain value of temperature $\bar{T}$, there exist a correspondent value of doping level $\overline{N_D}$ at which the number of free-carrier generated by donors result equal to the thermally generated carriers. In case a lower doping level is considered, the free carrier density is determined exclusively by thermally generated electron, so only an increase of the temperature have significant effects on free-carrier absorptions processes. Therefore only dopant concentrations higher than $\overline{N_D}$ can affect the free carrier concentration at temperature $\bar{T}$ and thus have consequent effects on the absorption coefficient.

4.4 Wafer optical properties

Once the radiative properties of silicon and $Si_{1x}Ge_x$ alloys are known, the spectral-directional optical properties of the wafer can be assessed as a function of temperature, dopant concentration and thicknesses of multi-layer structure. The low absorption coefficient experienced by lightly doped silicon at low temperature described in Section 4.3, give rise to semi-transparent behavior within this wavelength range at typical wafer thickness of about $400\mu m$. Because of this, wafer is represented as an optical element in which coherent and incoherent internal multiple reflections should be taken into account in order to obtain an accurate optical model. The simplest and most effective way of calculating the radiative properties for multi-layer structure is by thin film optics [4.43], which predicts the reflectance and transmittance of a multi layer film stack for a particular wavelength and angle on incidence. However, the theory is valid under the assumption of optically smooth and parallel interfaces. While this is true in general for the front side of the wafer, which is a multilayered, homogeneous, optically smooth surface, the theory could not in principle be applied to the backside surface, which whereas has rough optic interfaces. As it will be seen further in Section 4.4.3, the theory can be employed as a good

approximation also for surface whose roughness RMS is lower than the wavelength of the incoming radiation.

4.4.1 Coherent Formulation

When the thickness of each layer is comparable or less than the wavelength of incoming electromagnetic waves, the wave interference effects inside each layer become important to correctly predict the radiative properties of multilayer structure of thin films. By treating the electromagnetic radiations as a waves, the thin film optics is capable of capture the interference effects in the layers. The main assumptions of this theoretical approach are

- The surface of the stack and all the interfaces between the films are optically smooth. Each interface is typically characterized by parameter called *optical roughness*, expressed as σ_{rms}/λ, where σ_{rms} is the root mean squared (RMS) roughness. If optical roughness is smaller than unity, then the interface is deemed optically smoot, and if not, it is deemed optically rough.
- The interfaces between the films are parallel.
- Dimension of the sample in the direction parallel to the interface is much larger than the wavelength. Otherwise, the incident light encounters the film edge which is an interface not parallel to the interfaces between films.
- The optical constants within a particular layer do not vary in the direction perpendicular to the interface.

In Fig. (4.11) is shown a schematic representation of the multilayer structure. The transfer-matrix method provides a convenient way to calculate the radiative properties of multilayer structures of thin films. For the j th medium of thickness d_j, the complex refractive index is

$$\widetilde{n_j} = n_j + i\kappa_j \tag{4.22}$$

where n_j and κ_j are the real refractive index and the extinction coefficient respectively. It is assumed that $\widetilde{n_1} = 1$, i.e. the top semi infinite medium is air, and the optical properties of air are assumed to be the same as those of vacuum. The electromagnetic wave is incident from the first medium at angle of incidence θ_1, and is transmitted through or reflected from the following layers. By assuming that the electric field in the jth medium is a summation of the forward and backward waves in z-direction, the electric field in each

layer can be expressed as a function of the A_j and B_j amplitudes of forward and backward waves in the j th layer respectively. Detailed expression of the electric field in each layer can be found in Ref. [4.43]. Using the central equation of the multilayer theory, it is possible to relate the amplitudes of the first interface with those of the Nth interface

$$\begin{pmatrix} A_1 \\ B_1 \end{pmatrix} = \left[\prod_{j=1}^{N} P_j D_j^{-1} D_{j+1} \right] \begin{pmatrix} A_{N+1} \\ B_{N+1} \end{pmatrix} = \begin{bmatrix} m_{11} & m_{12} \\ m_{21} & m_{22} \end{bmatrix} \begin{pmatrix} A_{N+1} \\ B_{N+1} \end{pmatrix} \tag{4.23}$$

where P_j is the propagation matrix, D_j is the dynamic matrix, and m_{ik} is an element of the transfer function matrix. The propagation matrix accounts for the effect of absorption and interference within a layer j bounded by two interfaces. Because layer 1 is not bounded by two interfaces, the propagation matrix has no meaning, and P_1 is set equal to identity matrix. For layers 2,3, $\cdots$, N the propagation matrix is

$$P_j = \begin{bmatrix} e^{i\phi_j} & 1 \\ 1 & e^{-i\phi_j} \end{bmatrix} \tag{4.24}$$

where $\phi_j = 2\pi \tilde{n}_j d_j \cos(\tilde{\theta}_j)/\lambda$ is the phase shift, $\tilde{n}_j$ is the complex refractive index expressed in Eq.(4.12), and $\tilde{\theta}_j = sin^{-1}(n_1 \sin\theta_1/\tilde{n}_j)$ is the complex angle.

The dynamic matrix account for reflection and refraction at the interface j, relating amplitudes of reflected and refracted waves on either side of the interface. Depending on the state of polarization of the wave, the dynamic matrix is given by

$$D_j = \begin{bmatrix} 1 & 1 \\ \tilde{n}_j \cos\tilde{\theta}_j & -\tilde{n}_j \cos\tilde{\theta}_j \end{bmatrix} \qquad s\ polarization \tag{4.25}a$$

$$D_j = \begin{bmatrix} \cos\tilde{\theta}_j & \cos\tilde{\theta}_j \\ \tilde{n}_j & -\tilde{n}_j \end{bmatrix} \qquad p\ polarization \tag{4.25}b$$

where s and p indicate that electric field vector is perpendicular and parallel to the plane of incidence, respectively. Non-absorbing layers have purely real refractive index, so they have purely real angles that can be interpreted as the direction of propagation in the layer. Absorbing layers have complex refractive indices, so they have complex angles which have no direct physical interpretation. The angle θ_1 is purely real and interpreted as the angle of incidence. Given the angle of incidence, the complex angle for the other layers are calculated in succession using the complex form of Snell's law

$$\sin\tilde{\theta}_{j+1} = \frac{\tilde{n}_j}{\tilde{n}_{j+1}}\sin\tilde{\theta}_j \tag{4.26}$$

The reflectance for an s or p wave for the whole stack is the ratio of the intensities of the forward and backward propagating waves on the left side of interface 1. The transmittance for and s or p wave is the ratio of the intensities of the forward propagating on the right side of the interface N and the forward propagating wave on the left side of interface 1. The intensity of an electromagnetic wave is proportional to the square of its amplitude

$$R_{s/p} = \frac{B_1}{A_1} = \left|\frac{m_{21}}{m_{11}}\right|^2 \tag{4.27}$$

$$T_{s/p} = \frac{\tilde{n}_{N+1}\cos\theta_{N+1}}{\tilde{n}_1\cos\theta_1}\frac{A_{N+1}}{A_1} = \frac{\tilde{n}_{N+1}\cos\theta_{N+1}}{\tilde{n}_1\cos\theta_1}\left|\frac{m_{21}}{m_{11}}\right|^2 \tag{4.28}$$

Here $T_{s/p}$ is the transmittance for the s or p polarization and $R_{s/p}$ the reflectance for the s or p polarization. As thermal radiation emitted from the heater element can be well approximated as unpolarized, $R_{\lambda,\theta}$ and $T_{\lambda,\theta}$ may be calculated as simple arithmetic average between the s or p polarization components [4.44].

4.4.2 Incoherent Formulation

When the thickness of the layer is much greater than the wavelength of the incoming radiation, interferences effects due to coherent radiative interactions can be neglected. Wafers used in this work have thicknesses in the range between $300\mu m$ and $450\mu m$, which is at last about 1 order of magnitude greater than the maximum wavelength value considered for calculations. In this case, the incoherent formulation or geometric optic should be used to predict the radiative properties of the silicon substrate, while the coherent formulation results are used to describe the optical behavior of the multilayer structures which are present on the surface of the silicon substrate. In Fig. (4.11) is represented the geometrical configuration employed for calculation, composed by the silicon substrate and two layer stacks on the top and bottom surfaces. The radiation is supposed impinging on the top surface. The fraction of the incident radiation reflected form the top surface is $R^*_{s/p}$, the apparent reflectivity of the sample, and the fractional transmitted is $T^*_{s/p}$, the apparent trasmissivity. These quantities include the effects of

multiple reflections within the slab and are calculated, as in the case of coherent formulation, for s and p polarizations. Summation of the contribution from the multiply-reflected rays shown in Fig. (4.11) give the expressions for $R^*_{s/p}$ and $T^*_{s/p}$ [4.43]

$$R^*_{s/p} = \rho_{tv} + \frac{a^2\tau_t^2\rho_{bs}}{1 - a^2\rho_{ts}\rho_{bs}} \tag{4.29}$$

$$T^*_{s/p} = \frac{a\tau_t\tau_b}{1 - a^2\rho_{ts}\rho_{bs}} \tag{4.30}$$

where τ_t and τ_b are the transmissivities of the top and bottom stacks of films, ρ_{tv} is the reflectivity of the top of the stack for radiation incident from the outside, i.e. the vacuum, ρ_{ts} is the reflectivity for radiation incident from the inside the substrate and ρ_{bs} is the corresponding reflectivity for the bottom multilayer structure. These quantities regards the multilayer structures and therefore it is possible to calculate them using the Eq. (4.27) and Eq. (4.28), which result from the coherent formulation. The a term describes the attenuation of intensity experienced by a ray passing through the substrate and can be expressed as

$$a = \exp\left(-\frac{4\pi\kappa_s d_s}{\lambda\cos\theta_s}\right) \tag{4.31}$$

where d_s is the thickness of the silicon substrate and θ_s is the angle of refraction as defined in previous Section. In case absorption is taken into account, the angle of refraction is complex. However, for slightly absorbing medium with $\kappa_s \ll 1$, θ_s can be determined using Snell's law of refraction [4.45]. For silicon, the expression of κ_s derive from calculations performed in Section 4.3.1, and thus it depends on the temperature, dopant concentration and wavelength. By this way, the optical properties of the wafer reflects the physical properties of the silicon which compose the substrate. Using the Kirchhoff's law, that states that the absorptivity, defined as the fraction of incident power that is neither reflected nor transmitted, equals the emissivity for radiation emitted at the same wavelength, angle of incidence and polarization, the expression of the emissivity $\varepsilon_{s/p}$ of the wafer can be calculated as

$$\varepsilon_{s/p} = 1 - R^*_{s/p} - T^*_{s/p} = 1 - \rho_{tv} - \frac{a\tau_t(\tau_b + a\tau_t\rho_{bs})}{1 - a^2\rho_{ts}\rho_{bs}} \tag{4.32}$$

while the emissivity for unpolarized light can be expressed as [3.30]

$$\varepsilon = \frac{\varepsilon_s + \varepsilon_p}{2} \tag{4.33}$$

If the sample is opaque, i.e. a = 0, the spectra emissivity results $(1 - \rho_{tv})$.

4.4.3 Surface roughness effects

As described early, real wafer surfaces may not match the simple model adopted by the thin film optics. The front surface may be textured by pattern etched in coating or by the presence of epitaxially grown devices, and the 'not polished ' back surface are rough with RMS on the order of $1\mu m$ [4.22]. Under these circumstances, the approach outlined above may not predict correctly the optical properties of the wafer. Roughness has various physical effects on the interaction of electromagnetic radiation with the surface which are not accounted for in the thin film optic theory. Firstly, it causes scattering of incident radiation in directions other than specular ones [4.46]. Secondly, diffraction effects may arise [4.46]. For multilayer structures, the interface roughness can destroy the coherence of the interfering electromagnetic waves, reducing the amplitude of interference fringes [4.47]. Finally, if there are surface cavities with dimensions comparable to or larger than the wavelength with the large height-to-width ratios, there can be multiple reflections in these cavities which decrease the overall reflectance [4.48].

There have been various studies of the emissivity of the backside of bare silicon wafers. Xu and Sturm [4.49] found that surface roughness had a large effect on the dependence of the reflectance on illumination angle, by measuring the reflectance of bare silicon wafer with varying degree of surface roughness. The results are also compared with the theory developed by Beckman [4.46]. The comparison shows that the theoretical model captures the correct trends, but experimental measurements suggest that multiple reflection in surface cavities, not accounted in the Beckmann model, had a significant effects on optical properties. For multilayer structures with rough interfaces, thin film optics have been extended using the Beckmann model to predict the reflectance in the specular direction [4.47]. An important work have been made by Zhou and Zhang [4.50], in which they developed a Monte Carlo model to calculate the radiative properties of semitransparent wafers with surface roughness. A statistical model of the random surface roughness have been first developed and then solved using a numerical ray tracing technique, assuming that geometrical optics is applicable to the reflection between microfacets at the surfaces and inside the silicon wafer [4.51]. As described early, the slope of the microfacets have

strong influence on the radiative properties of the surface, and a Gaussian distribution have been employed. The radiative properties of Silicon as described in Section 4.3.1 are employed for modeling the optic behavior of the silicon substrate. From simulations, the radiative properties of lightly doped silicon wafer, including emittance, reflectance, trasmittance, bidirectional reflectance distribution function (BRDF) and bidirectional transmittance distribution function (BTDF) can be assessed as a function of the roughness parameter, temperature, dopant concentration and wavelength.

On the other hand, Hebb *et al.* [4.22] verify the thin film optics on rough surface of bare and coated silicon wafer using experimental data of the total reflectance integrated over the hemisphere at room temperature. Because of the assumptions of this theory, the results found in earlier sections, i.e. Eq. (4.29) and Eq. (4.30), are to be intended as referred to specular directions. Since optically rough surfaces generally reflect radiation in all direction in the hemisphere, the results of the thin film optics applied to the rough surface are intended being referred to the integrated energy reflected in all direction by the surface. Thus no information on the directional dependence of the portion of the incoming energy that is diffusely or specularly reflected can be gained by thin film optics. The agreement between the theoretical results and experimental measurements are also compared with the surface roughness profile, which have been characterized using AFM. The ability of thin film optics to yield accurate predictions of the radiative properties of these surfaces depends infact how badly the assumptions are violated. If the slopes of the rough surface are very gentle, then the surface may be considered locally smooth, and thin film optics may be adequate for predicting the radiative properties. Gentle slope would also indicate a surface with shallow surface cavities. Various backside surface from different wafer manufacturer are studied [4.22]. In Fig. (4.12)a the theoretical and experimental reflectance data for bare lightly doped silicon wafers are presented, while Fig. (4.12)b shows the AFM image of the surface. For wavelength smaller than the bandgap wavelength, the measure reflectance is somewhat smaller than predicted. However the differences almost lie within the experimental uncertainty. At the microscale, the RMS roughness is $0.87\mu m$, while at the nanoscale the surface is smooth. The rise in the measured reflectance at $1.1\mu m$ is due to multiple reflections in the wafer, which is semitransparent at these wavelength range due to a low value of dopant concentration and temperature. The under prediction of the reflectance at wavelength above bandgap could be due to total internal reflection in the wafer [4.52]. Nevertheless, the results shows that the thin film optics is capable of giving a good approximation of the total

hemisphere reflectance for a rough surface even if multilayered structures are present on the surface [4.22], and the agreement goodness is better as the microfacets slopes are stepper.

References

[4.1] R. Siegel, J.R. Howell, *Thermal Radiation Heat Transfer,* 3rd ed., 22-37. Washington, DC: Hemisphere Publishing Corporation, 1992.

[4.2] P.J. Timans, *Mater. Sci. Semicond. Process.*, vol **1** (1998), p. 169

[4.3] A. Kersch, *Phoenics J.*, vol. **8** (1995), 421

[4.4] A. Kersch, W.J. Morokoff, *Transport simulation in Microelectronics*, Birkh[a]user-Verlag, Basel, 1995.

[4.5] A. Kersch, T. Schafbauer, ' Thermal modeling of the RTP and RTPCVD processes ', *Thin Solid Films*, vol **365** (2000), pp. 307-321.

[4.6] R. Kakosche, E. Buβman, ' Simulation of temperature effects during rapid thermal processing ', *Mat. Res. Proc.*, vol **146** (1989), p. 473

[4.7] K. Nishino, S. Yamashita, K. Torii, *Experimental Thermal and Fluid Science,* vol **10** (1995), pp. 258-271

[4.8] M.M. Yovanovich, *Int. J. Heat Mass Transfer,* vol **12** (1969), pp. 1517-1520

[4.9] R. Holm, *Electric Contacts-Theory and Application,* 4th e., p. 16, Springer-Verlag, New York, 1967

[4.10] G.D. Nutter, *Theory and Practice of Thermal Radiation Thermometry,* edited by D.P. DeWitt, and G.D. Nutter, 231-337. ùNew York: Wiley, 1988

[4.11] D.W. Pettibone, J.R. Suarez, A Gat, *Mater. Res. Soc. Symp. Proc.*, vol **52** (1986), p. 209.

[4.12] P.J. Timans, *Solid State Technol.*, vol **40** (1997), p. 63.

[4.13] P. Vandenabeele, W. Renken, *Mater. Res. Soc. Symp. Proc.,* vol **470** (1997), p. 17

[4.14] P. Vandenabeele, W. Renken, *Mater. Res. Soc. Symp. Proc.,* vol **525** (1997), p. 115

[4.15] A.R. Abramson, ' Effect of Doping Level During Rapid Thermal Processing of Multilayer Structures', *J. Mater. Res. ,* Vol. 14, No. 6, pp. 2402-2410, 1999

[4.16] A.B. Sproul, M.A. Green, ' Improved value for the silicon intrinsic carrier concentration from 275 to 375 K ', *J. Appl. Phys.,* 70, 375, (1991)

[4.17] B.J. Lee, Z.M. Zhang, ' Temperature and Doping Dependence of Radiative Properties of Silicon: Drude model revisited ', *13th International conference on Advance Thermal Processing of Semiconductors, 2005*

[4.18] R. Doering, Y. Nishi, ' Handbook of Semiconductor Manufactoring Technology – Second Edition ', CRC Press, (2008)

[4.19] H. Rogne, P.J. Tilmans, and H. Ahmed, *Appl. Phys. Lett.,* 69, 2190, (1996)

[4.20] P.J. Tilmans, ' The Themal Radiative Properties of Semiconductors ' *Advances in Thermal and Integrated Processing,* F. Roozeboon (ed.), Kluwer Accademic Publishers, Dordrecht, the Netherlands (1996).

[4.21] W.G. Spitzer, H. Y. Fan, ' Determination of Optical Constants and Carrier Effective Masses of Semiconductors ', *Phys. Rev.*, vol **1** (1957), pp. 882-890.

[4.22] J. P. Hebb, ' Pattern effects in Rapid Thermal Processing ', Ph.D. Dissertation, Dept. of Mechanical Engineering, Massachusset Institute of Technology, Cambridge, MA (1997).

[4.23] G.E. Jellison, F.A. Modine, ' Optical Functions of Silicon at Elevated Temperatures ', *J. Appl. Phys.,* vol. **76** (1994), pp. 3758-3761.

[4.24] H.H. Li, ' Refractive index of Silicon and Germanium and Its Wavelengh and Temperature Derivatives ', *J. Phys. Chem. Ref. Data*, vol **9** (1980), pp. 561-658.

[4.25] B.J. Lee, Z.M. Zhang, E.A. Early, D.P. DeWitt, B.K. Tsai, ' Modeling Radiative Properties of Silicon with Coating and comparison with Reflectance Measurements ', *J. Thermophys. Heat Transfer,* (2005).

[4.26] A.N. Magunov, ' Temperature dependence of refractive index of Silicon single-crystal in the 300 -700 K range ', *Opt. Spectroscop.*, vol. **73**, 205 (1992)

[4.27] P.J. Tilmans, ' The effect of coating on the emissivity of Silicon ', *Proceedings of 2nd International Rapid Thermal Processing Conference*, Monterey, CA, 186 (1994)

[4.28] P.J. Tilmans, ' Emissivity of Silicon at Elevated Temperature ', *J. Appl. Phys.*, vol. **74** (1993), pp. 6353-6364

[4.29] J.C. Sturm, C.M. Reaves, *IEEE Trans. Electron Devices,* vol. **39**, 81 (1992)

[4.30] G.G. MacFarlane, T.P. McLean, J.E. Quarrington, V. Roberts, *Phys. Rev.*, vol **111**, 1245 (1958)

[4.31] T.P. McLean, in *Progress in Semiconductors*, edited by A.F. Gibson, F.A. Kr[o]ger, R.E. Burgess (Heywood, London, 1960), vol. **5**, pp. 53-102

[4.32] J.E. Jellinson, Jr. and D.H. Lowndes, *Appl. Phys. Letters,* vol. **41**, 594 (1982)

[4.33] D.F. Edwards, ' Silicon (Si) ', *Handbook of Optoical Costants of Solids,* E.D. Palik (ed.), Academic Press, Orlando (1985), pp. 547-569

[4.34] T.K. Gaylord, J.N. Linxwiler, ' A Method for Calculating Fermi Energy and Carrier Concentrations in Semiconductors ', *Am. J. Phys.*, vol. **44**, (1976), pp. 353-355

[4.35] S.M. Sze, *Physics of Semiconductor Devices*, 2nd ed., Wiley, New York (1981)

[4.36] D.L. Rode, *Semiconductors and Semimetals,* vol. **10**, eds. R.K. Willardson and A.C. Beer, Academic Press, New York (1975)

[4.37] W.E. Beadle, J.C.C. Tsai nad R.D. Plummer, *Quick Reference Manual for Silicon Integrated Circuit Technology,* Wiley, New York (1985)

[4.38] F.J. Morin, J.P. Maita, *Phys. Rev.*, vol. **96**, 28 (1954)

[4.39] M.A. Saifi, R.H. Stolen, ' Far-Infrared Interference Technique for Determining Epitaxial Silicon Thickness ', *J. Appl. Phys.*, vol. **43** (1972), pp. 1171-1178

[4.40] W.G. Spitzer, G.W. Goebli, F.A. Trumbore, ' Effect of Heat Treatment on Optical Properties of Heavily Doped Silicon + Germanium ', *J. Appl. Phys.*, vol. **35** (1964), pp. 206-211

[4.41] P. Vandenabeele, K. Maex, ' Influence of Temperature and Backside Roughness on the Emissivity of Si Wafer During Rapid Thermal Porcessing ', *J. Appl. Phys.*, vol. **72** (1992), pp. 5867-5875

[4.42] P.A. Schumann, W.A. Keenan, A.H. Tong, H.H. Gegenwar , C.P. Schneide, ' Silicon Optical Constants in Infrared ', *J. Electrochem. Soc.,* vol. **118** (1971), pp. 145-148

[4.43] P. Yeh, *Optical Waves in Layered Media*, Wiley, New York (1988)

[4.44] D.L. Chapek, R.A. Weimer, K.F. Scheugraf, A. Ahmad, R.P.S. Thakur, R. Singh, ' Correlation between thermal stress and the performance of devices processed by RTP ', *Proc. 3rd International Rapid Thermal Processing Conference,* August 30-September 1, Amsterdam, The Netherlands, p. 281 (1995)

[4.45] Z.M. Zhang, ' Optical properties of a Slightly Absorbing Film for Oblique Incidence ', *Appl. Opt.*, vol. **38** (1999), pp. 205-207

[4.46] P. Beckmann, A. Spizzichino, *The scattering of Electromagnetic Waves from Rough Surfaces,* Permagon Press, New York (1963)

[4.47] C.L. Mitsas, D.I. Siapas, ' Generalized matrix method for analysis of coherent and incoherent reflectance and transmittance of multilayer structures with rough surfaces, interfaces, and finite substrates ', *Appl. Optics,* vol. **34** (1995), p. 1678

[4.48] R. Siegel, J.R. Howell, *Thermal Radiation Heat Transfer,* Washington, DC: Hemisphere, 1992.

[4.49] H. Xu, J.C. Sturm, ' Emissivity of srough silicon surfaces: Measurement and calculations ', in *Proc. Symp. Mat. Res. Soc.*, 1995, vol. **387**, pp. 29-35

[4.50] Y.H. Zhou, Z.M. Zhang, ' Radiative Properties of Semitransparent Silicon Wafers with Rough Surfaces ', *J. Heat Transfer,* vol. **125** (2003), pp. 462-470

[4.51] K. Tang, R.O. Buckius, ' A Statistical Model of Wave Scattering from Random Rough Surfaces ', *Int. J. Heat Mass Transfer,* vol. **44** (2001), pp. 4059-4073

[4.52] P. Vandenabeele, K. Maex, R. De Keersmaecker, ' Impact of pattern layers on temperature nonuniformity during rapid thermal processing ', *Mater. Res. Soc. Proc.*, vol. **149** (1989), p. 149

[4.53] P.J. Timans, in *Rapid Thermal Processing 1993*, edit by R.B. Fair and B. Lojek, RTP 1993, Scottsdale, 1993, 282-6

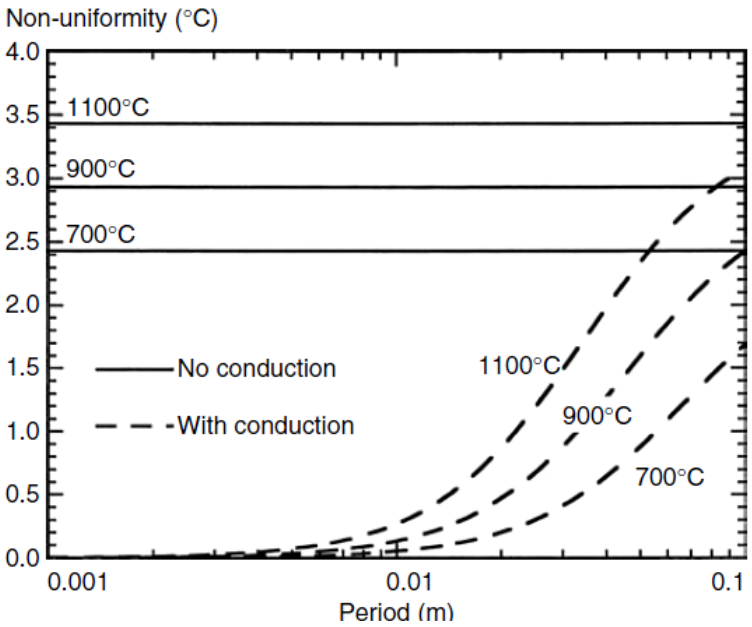

Fig. 4.1 The effect of a spatial modulation of incident power density on wafer temperature uniformity. The curves show predictions of the magnitude of the temperature non-uniformity caused by a 1% sinusoidal modulation in the input power density for a 725$\boldsymbol{\mu m}$ thick silicon wafer at 700, 900 and 1100°C [4.18]

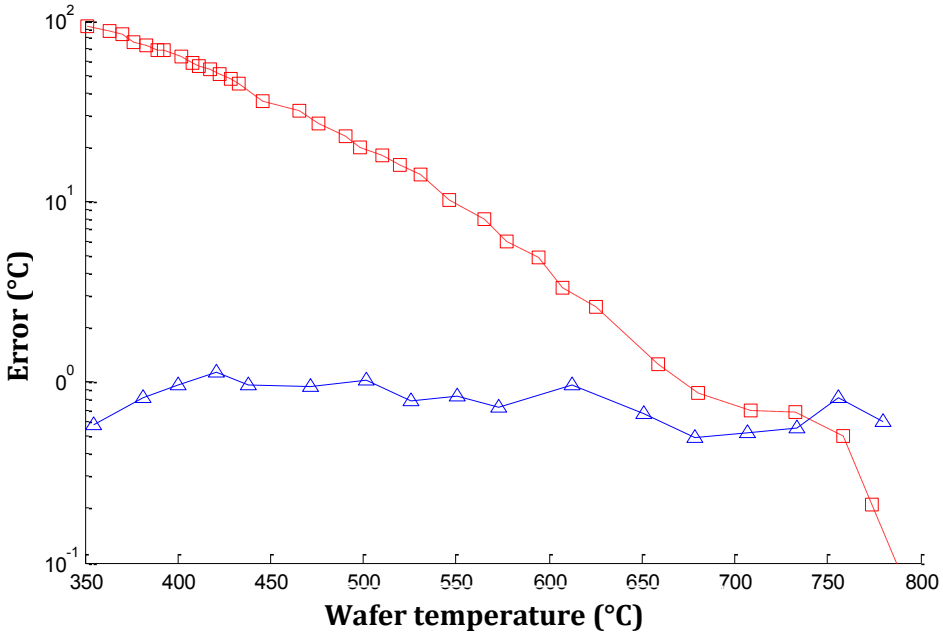

Fig. 4.2 Calculated pyrometric measurement error for high and low doped silicon wafers [4.53] as a function of the substrate temperature in case a constant emissivity value $\boldsymbol{\varepsilon} = 0.67$ and $\lambda_p = 0.95$ μm are employed.

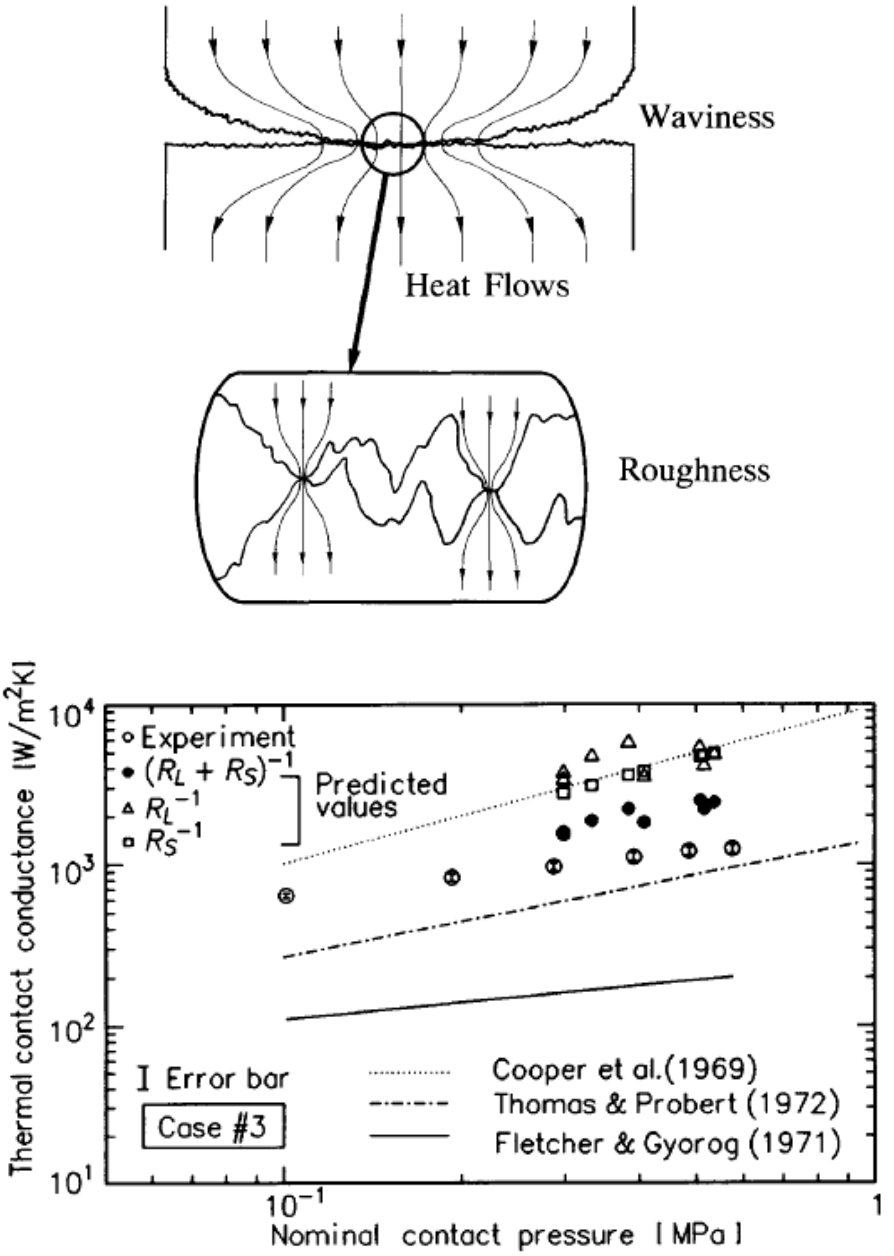

Fig. 4.3 *a)* Schematic representation of the macroscopic and microscopic costriction thermal resistance for contact interfaces. *b)* Experimental measurement and theoretical prediction of the total contact thermal resistance for a rough/rough interface in vacuum environment [4.7]

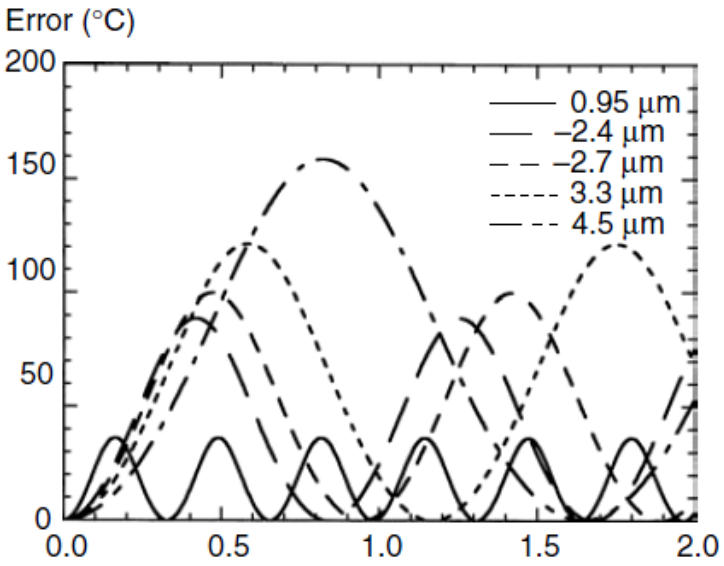

Fig. 4.4 The impact of silicon dioxide thickness on the temperature measurement errors in pyrometry. The error is positive when the pyrometer overstimates the wafer temperature. [4.18]

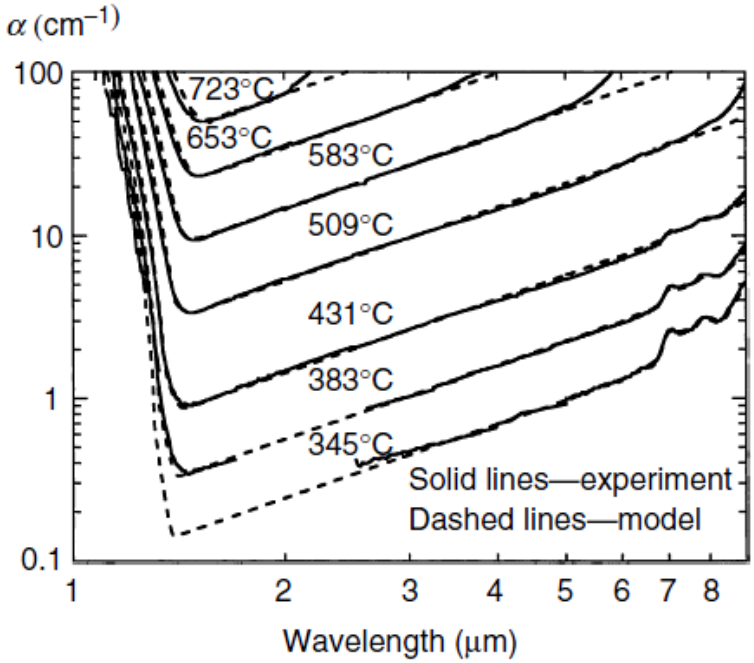

Fig. 4.5 The absorption spectra of Silicon for a range of temperatures [4.19]

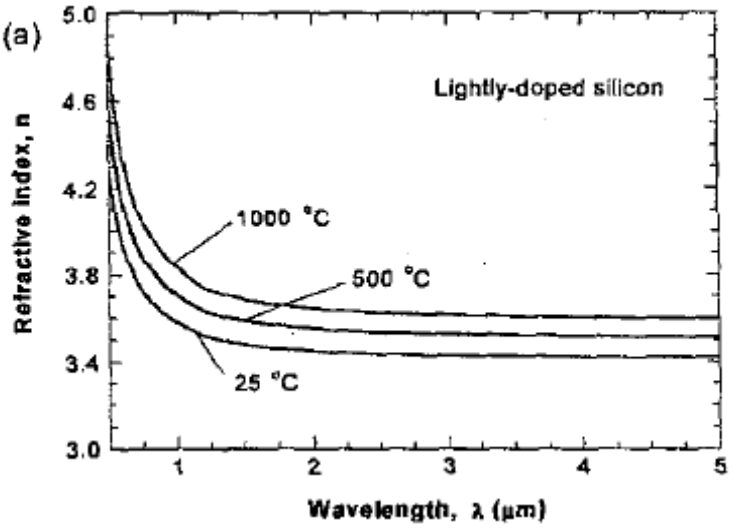

Fig. 4.6 The refractive index of Silicon calculated from the empirical expression listed in Section 3.3.1

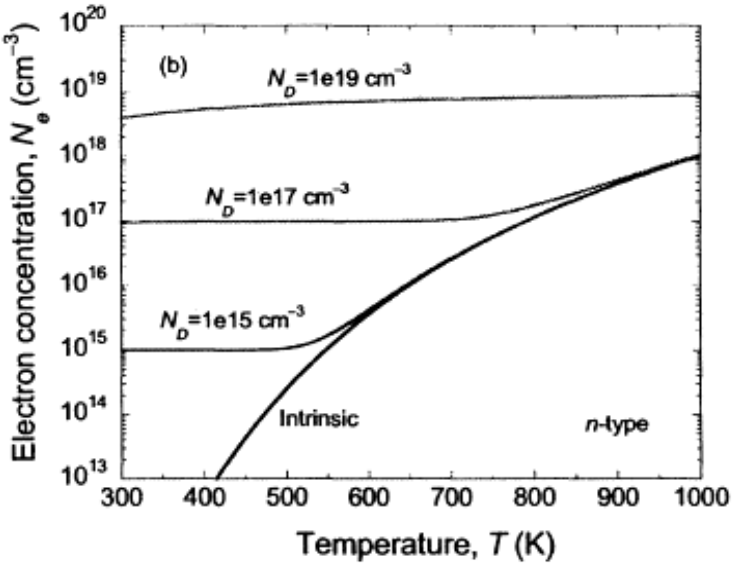

Fig. 4.7 Calculated electron concetration N_e in silicon conduction band as function of the temperature and dopand concentration [4.17].

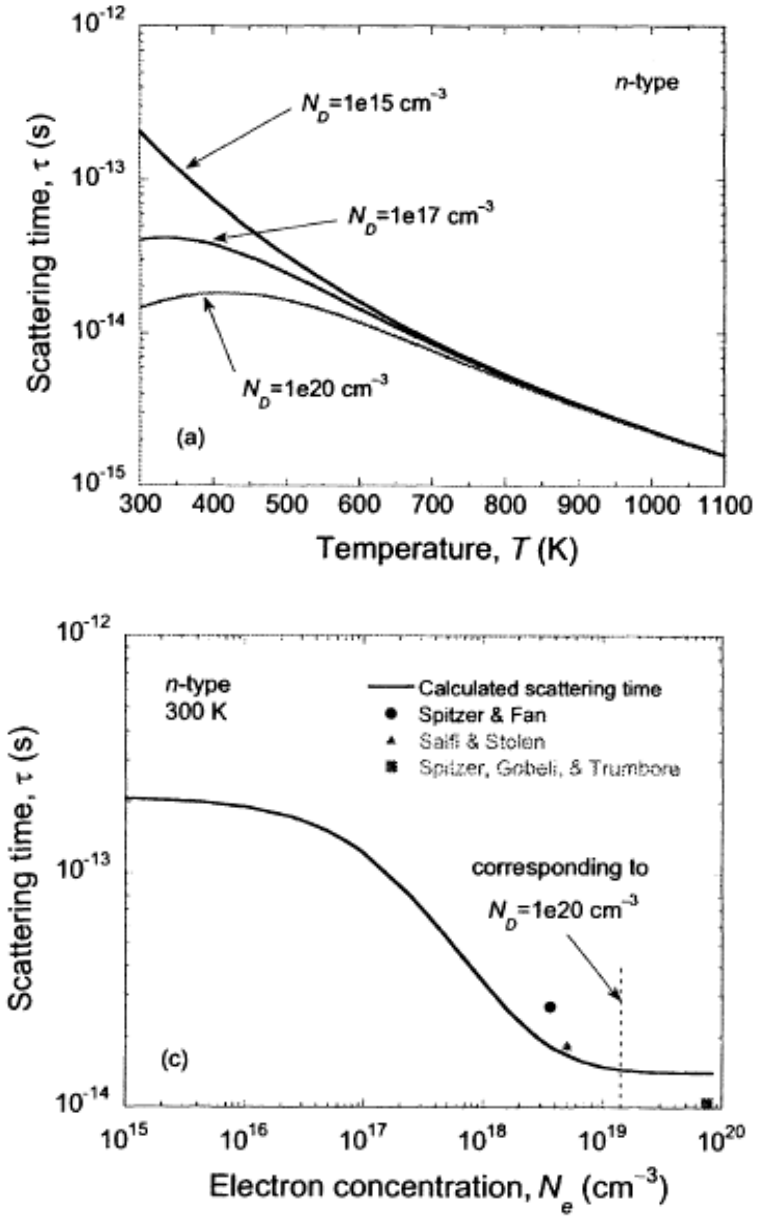

Fig. 4.8 *a)* Calculated electron scattering time $\boldsymbol{\tau}$ as a function of the temperature and dopant concentration $\boldsymbol{N_D}$ *b)* Comparison between the calculated electron scattering time in silicon with experimental measurements. [4.17]

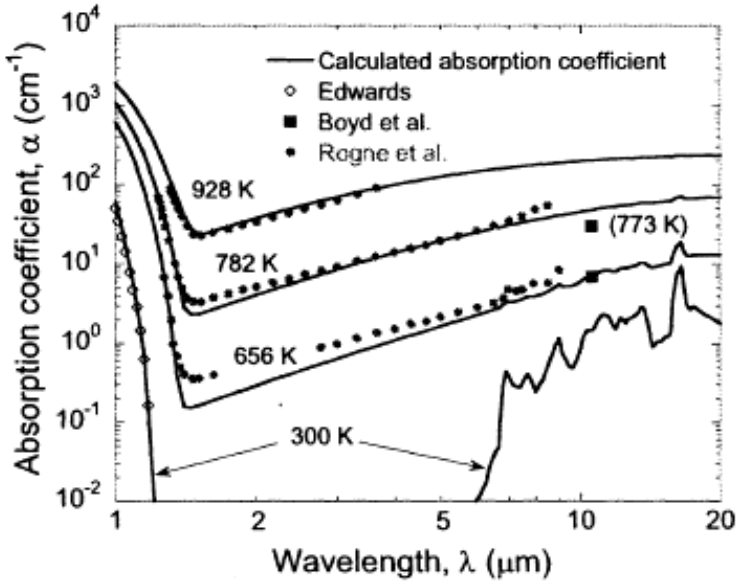

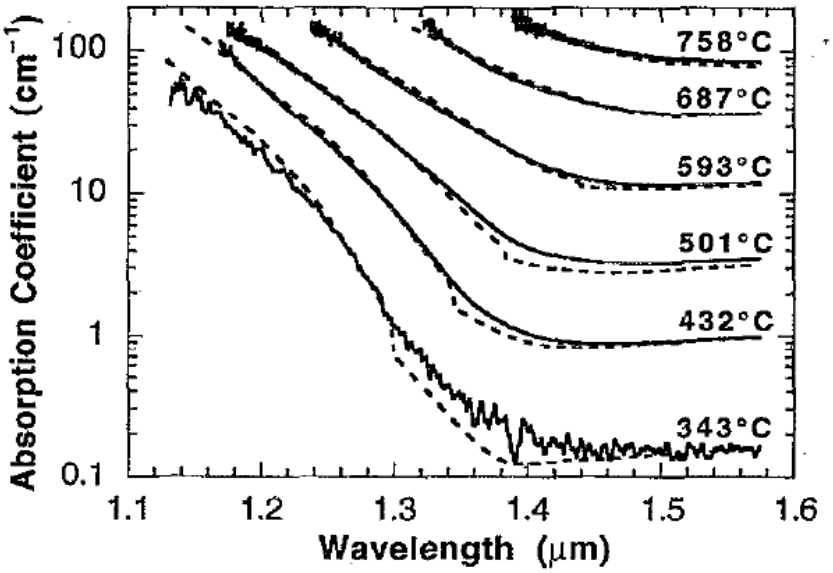

Fig. 4.9 *a)* Calculated and experimental data of lighly doped silicon absorption coefficient $\boldsymbol{\alpha}$ for different temperatures [4.28] *b)* Comparison between the semiempirical model proposed by Timans [4.39] and measured data

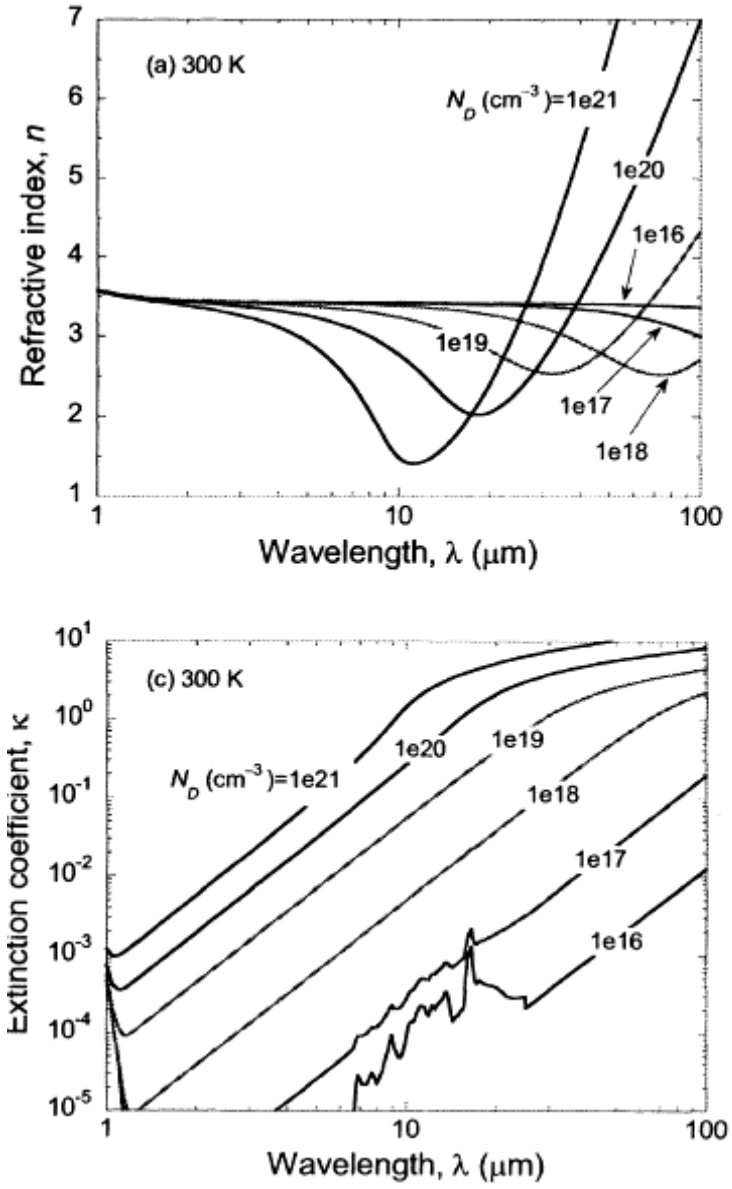

Fig. 4.10 Calculated optical constants of Silicon for different dopant concentration. Calculation have been performed at room temperature. [4.28]

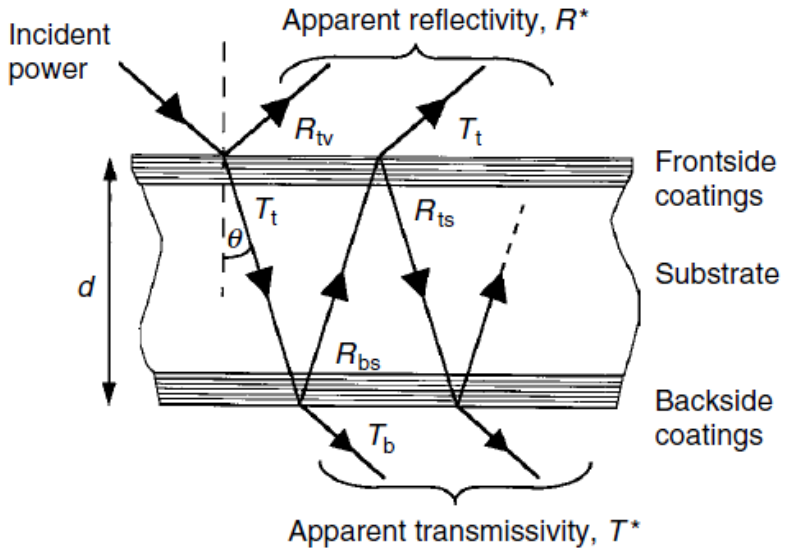

Fig. 4.11 Schematic representation of the wafer configuration for thin film optics calculation

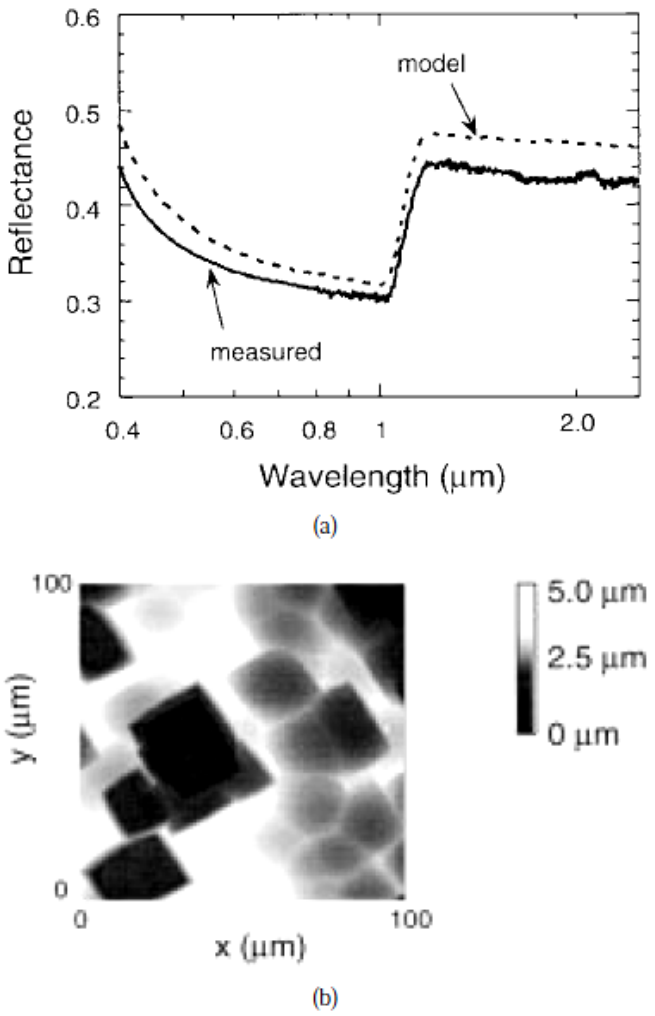

Fig. 4.12 *a)* Theoretical calculation of silicon rough surface reflectance compared with experimental measurements *b)* AFM image of the wafer backside surface. [4.22]

CHAPTER 5
Thermal FEA results

5.1 LEPECVD Heating Stage

In Fig. (5.1) is shown a 3D schematic representation of the heating stage employed within the LEPECVD reactor and under study in this work, which is meant for 4" substrates. The wafer is radiatively heated for behind using a current powered heating element, which is constructed from high-density (HD) graphite, coated with pyrolitic graphite. The HD graphite is usually adopted in UHV heater design tanks to its thermal, structural and electrical properties at high temperatures, i.e. low thermal expansion coefficient, high tensile and compressive strength and ability to withstand to high electrical current densities. It also shows an unique behavior of the tensile, compressive and flexural strengths which increase proportionally with the temperature up to a value as high as 2700 K. At this value, graphite has about double the strength it has when at room temperature. Although it reacts with oxygen only at temperatures above 500°C, the graphite is very inert and can therefore operate in very corrosive or aggressive environments without degradation. The high surface porosity is otherwise an important issue for UHV environment, as it undergoes an initial out-gassing process which could causes a possible consequent particle contamination of the reactor chamber. By using pyrolytic graphite (PG) or pyrolytic boron nitrate (PBN) surface coatings, the problem of out-gassing can be overcome as they both have virtually zero surface porosity. The deposition of the PG coating is achieved by means of the pyrolysis of gaseous hydrocarbon which results in an aggregate of graphite crystallites with dimensions that may reach several hundred of nm and various degree of orientations. Depending on deposition

conditions, particle dimensions and orientations can be tuned so that either anisotropic or isotropic properties of the coating are obtained. This coating process not only fills the open pores of the HD graphite, but also improves the density, strength and corrosion resistance. The use of PBN coating instead best fits for applications in which an efficient protection against oxidation at temperature over 800°C is mandatory.

The heater under study has a mender shape which form a series of parallel 5.2 x 4 mm coil rod spaced each other by 1.2 mm and a overall circular shape with a diameter of about 125 mm. The temperature of the graphite element is controlled by modulating the current density through the coils, with a maximum value of 93 A, and can operate at temperatures as high as 1273 K. The two power terminals spaced 155 mm acts also as holding element of the graphite mender. In order to withstand to the high temperatures, protective elements made by refractory metals such as molybdenum or tantalum are included in the hot zone in contact with the heater mender as they ensure high performances at high temperatures. The graphite element is half enclosed in a refractory metal case and it is held in such as the upper surface is about 3 mm from the top edge of the metal enclosure. A further refractory metal foil is placed under the heating element at 15 mm from the top edge of the enclosure as a heat shield. This configuration ensure not only a heat protection for the remains elements within the reactor chamber, but also acts a homogenizer of the radiative power emitted from the graphite element by reflecting the radiation emitted in direction opposite to the substrate.

On the other hand, the wafer is held by a 4 mm thick, toroidal shaped subsceptor which has been made of Suprasil® 1 quartz in order to withstand the severe temperature gradients experienced during heating and cooling processes. The inner diameter is designed in such a way that the subsceptor is in contact with the wafer by a circular area section with radius of 2.25 mm, while the outer diameter . Three pin-point sustains made of refractory metals hold the subsceptor 1 mm far from the top edge of the heater element enclosure, in order to avoid thermal conduction. In the case of reverse deposition stage configuration whereas, the distance increase up to about 30 mm.

5.2 Experimental Temperature Measurements

5.2.1 Pyrometer measurements

A first set steady-state and transient temperature measurement have been carried out using optical pyrometer technique. In Fig. (5.2) is shown a schematic representation of the measurement set up, while in Tabel I are summarized several technical features of the SensorTherm® M09 pyrometer employed in measurements. The silicon sensor operates in the near-infrared region analyzing the radiative power emissions centered at $\lambda_p = 0.95$ μm within a spectral band of $\Delta\lambda = 50$ nm. As described in Section 4.2.1, this particular spectral range ensures an accurate measurements within the temperature range typical for silicon-germanium epitaxial deposition, i.e. between 400° and 1000°C, while minimizing the incidence of measurements errors. Within this range also, both highly and lightly doped silicon are opaque to radiation and the emissivity variation within the same temperature range of 400°C and 1000°C is about $\Delta\varepsilon/\varepsilon = 2.9\%$, which result using Eq. (4.11) in a maximum temperature mismatch $\Delta T = \pm 1.85$°C. The incoming radiation is focused onto the silicon sensor by an optical system which can detect the radiative emission with a maximum spatial resolution of 1.3 mm at the minimum focusable distance of 402 mm. This value results comparable with the minimum scale length at which significant temperature non-uniformities, i.e. greater than 1°C, can be expected along a silicon wafer surface [3.8]. The pyrometer has been fastened to a Spectrosil® 2000 quartz vacuum viewport which have a transmissivity of 95% at $\lambda_p = 0.95$ μm in case of normal incidence. Variations of the transmissivity for small angle deviations from the normal incidence have been neglected as evaluated being less than 1%.

Optical measurements have been performed first on the graphite heater element without the influence of the subsceptor and the wafer. Both steady-state and transient temperature data have been gathered in order to characterize thermal properties of materials and as further validation of the FE simulations. An graphite emissivity of 0.8, retrieved from literature data [5.3], and a time response of 10 ms have been set for measurements. Transient measurements have been performed centering the pyrometer spot on the middle point of the heater element's centre coils, while modulating the input current from a value of 28.1 A to a value of 11.3 A. Since a maximum temperature increase $\Delta T_{ch} = 90$°C of the chamber walls have been measured in case of extended use of powered heating element, the initial equilibrium temperature of the chamber has been set to 100°C

by a pre-baking process of the chamber. This ensures a time-constant and spatially uniform emission contribution of the chamber walls on the heating stage elements. Afterwards, an input current of 28.1A has been imposed to the graphite element until a quasi steady-state equilibrium temperature have been reached. The quasi steady-state have been then measured for different values of input currents until the read temperature reach the minimum value measurable of 400°C. In Fig. (5.3)a are presented the transient curves of the heating element for different current densities. The power is represented as a percentage of the maximum current allowed by the heating stage. The cooling rate obviously diminishes as the temperature decreases because of the reduction by T^4 of the total emitted power, ranging from 0.7°C/s to 0.1°C/s.

The steady-state measurement otherwise have been performed by evaluating the temperature in two different positions along the heater element after the quasi steady-state equilibrium have been reached. The pyrometer focus spot have been centered first on the first and then on the second coil of the heater, as a higher temperature gradient is expected in this region. Assuming that the temperature of the central region of the heater element is nearly independent from the thermal conductivity value, it is then possible to find out the value of the thermal conductivity by adjusting the finite element model thermal conductivity parameter as to fit the experimental measurements. This assumption can be reasonably considered as a good approximation thanks to several particular aspects of the graphite element and it has been also confirmed by FEA results. This aspect will be discuss in detail in Section 5.4.1. The measured temperature gradient have been used as an fitting parameter for finite element thermal conductivity value, which have been tuned in order to fit the measured data. The resulting thermal conductivity data found using FEA simulations have been than fitted using a third-order polynomial function

$$k_g = 2.964x10^{-8}\,T^3 + 1.76x10^{-4}\,T^2 + 0.3149\,T + 278.03 \qquad (5.1)$$

The subsequent measurement regard the temperature assessment of the heater configuration in which the subsceptor and the wafer are included. Temperature data are referred to the centre position of the wafer. A 4" *p*-doped, 6° off-cutted silicon wafer with high dopant concentration > 10^{19} cm^{-3} have been used for measurement. In order to get rid of temperature reading errors due to the presence of silicon dioxide on the surface, the wafer have been treated with a HF 2.5% solution for 5 min before loading into the reactor chamber. The surfaces of the subsceptor have been previously coated with a few hundred

of *nm* thick layer of germanium as to reproduce the operative conditions during the epitaxial growth deposition processes. Even in this case, an initial equilibrium temperature of the chamber have been set to 100°C by a pre-baking process of the chamber walls. Measurements also regards the *standard heating stage configuration*, i.e. with the subsceptor suspended 1 mm far from the upper edge of the refractory metal enclosure and the radiation emitted from the heater element impinges on the rough surface of the wafer. Finally, the transient behavior of the whole stage, which is presented in Fig. (5.3)b, have been characterized as a function of the input power using a modulating scheme equivalent to that of the transient heater measurements.

5.2.2 Instrumented Wafer measurements

The second set of steady-state temperature assessment have been carried out using a contact technique. In Fig. (5.4) is shown a schematic configuration of the ThermoElectric® instrumented wafer in which is indicated the position of the embedded thermocouples. Three type 'K' thermocouples have been employed as they can ensure high reliability and an accuracy of about 1.1°C over the temperature range of 30°C and 1000°C. Due to high temperature regimes and harsh condition experienced inside the reactor chamber, the TC junction have been laser welded to the wafer surface so that no bonding agents are not employed. This method is not only reliable for high temperature regimes but also eliminates the possibility of out-gassing in UHV environments. Furthermore, an accurate response time of the TC temperature reading is expected as the collateral thermal masses introduced by this welding process are minimized. By welding the junction upon the wafer surface and not within the bulk, the measurements reflects better the temperature profile of the very upper region of the wafer where the most relevant processes occur during epitaxial depositions. The instrumented wafer used in this work consists of a high *p*-type doped 4" silicon substrate with a 1 μm thick germanium layer deposited using the LEPECVD reactor, with the three TC junction have been welded on the Germanium layer. This configuration allow to understand the thermal behavior of the wafer as the deposition process is ongoing. This measurements regards the *inversed heating stage configuration*, i.e. with the subsceptor suspended 27 mm far from the upper edge of the refractory metal enclosure and the radiation emitted from the heater element impinges on the rough surface of the wafer. The temperature measurement results read by each TC are presented in Tabel II as a function of the input power. The temperature mismatch between the center and the outer TC increases proportionally with the input power,

ranging from 1°C at 5% of input power to 58.6°C as the 45% power has been reached. This trend also does not correspond to the maximum temperature gradient experienced by the wafer. This aspect will be addressed to Section 5.4.

5.3 Wafer radiative properties calculation

The dependence of the wafer optical properties from several physical aspect such as temperature, dopant concentration and thickness of the wafer have been calculated and imposed as a radiative boundary condition within the FE model of the heating stage. These effects indeed play a determinant role on the transient and steady-state thermal behavior of the wafer during the deposition process as found by Merchant *et al.* [5.6]. First, an assessment of the radiative properties along the wavelength spectrum range of 0.3 μm and 20 μm is performed using the theoretical approach describe in Section 5.3.1. Afterwards, the quantities are mediated and integrated over the wavelength spectrum using Eq. (4.4) and Eq. (4.5) in order to obtain the effective value which reflects the particular radiative conditions. Due to semitransparent behavior of the silicon, the calculation have been also performed for both bare silicon wafer and Ge/Si heterostructures.

5.3.1 Lightly doped Silicon wafer

In order to assess the effect of dopant concentration and temperature on silicon radiative properties, several calculation using non-coherent formulation of the thin film optics and the Drude optical model have been performed considering a single crystal silicon wafer with thickness of 390 μm. The wafer is opaque when the radiation penetration depth is much smaller than its thickness, i.e. $\lambda/4\pi\kappa_s \ll d$ where d is the thickness of the wafer. This case is valid for wavelengths which are shorter than that corresponding to the band gap or when the temperature is enough. In such a situation, the reflectance is the intrinsic reflectivity at the air-silicon interface and can be calculated form Fresnel's law coefficients, while the emissivity can be evaluated using the Kirchhoff's law of radiation. On the other hand, in the spectral region in which silicon is absorbing but not opaque, the results of non-coherent formulation, expressed by Eq. (4.29) and Eq. (4.30) should be used. In Fig. (5.6), several calculations performed in the wavelength ranges of 0.3 and 10 μm for lightly p-type doped silicon wafer with a dopant concentration less than 10^{15} cm^{-3} and different temperature valued are presented. The results are calculated supposing the

radiation impinges normally to the wafer surface. For wavelength longer to that correspondent to the absorption edge, a wafer with lower dopant concentration experiences a severe decrease of the absorption due to a low free-carrier absorption at low temperature. In this spectral region, the wafer results transparent to radiative power while the reflectivity is sensibly enhanced by multiple reflection inside the bulk. As the temperature increases, the carrier concentration also increases and the wafer absorptivity rise almost linearly with the wavelength value. Consequently, the spectral range of the transmissivity value shrink monolithically, until it become negligible at temperature over 1073 K. The shift of the bang gap towards longer wavelengths as the temperature increases can be clearly seen from Fig. (5.6). Furthermore, the small perturbation which is clearly visible for the 300 – 473 K curves for wavelengths longer than about 6 μm correspond to the absorption process due to weak phonon-photons interactions. As described in Section 4.3, this particular absorption process have an small impact on overall absorption coefficient and it is only visible in lightly doped silicon wafer for temperatures lower than about 673 K, after which the free-carrier absorption dominates.

5.3.2 Heavily doped Silicon wafer

For higher dopant concentration instead, the sensibility of the radiative properties to the temperature variations is drastically reduced. In Fig. (5.7) are presented the optical properties calculation results for silicon wafer *p*-doped wafers with Boron dopant concentration of 10^{19} cm^{-3} as a function of the temperature. Even at this high doping level, at room temperature the wafer results semitransparent to radiation emitted within the spectral range of about 1.1 – 5 μm, which cause a reflectivity enhancing due to multi-reflection processes within the wafer. Differently from the lightly doped case-study, the effects of the lattice absorption are not visible even at room temperature, mainly due to the high free-carrier concentration generated by the dopants. As the temperature increases, the semitransparent spectral range shrinks monolithically, until the wafer become opaque along the whole wavelength spectrum for temperatures over 1073 K.

5.3.3 Integrated Optical properties

The variations of the wafer spectral radiative properties inducted by the temperature and dopant concentration, are implemented into the numerical model using the integrated optical properties method, which can take into account the optical properties spectral

distribution of both the material considered and the impinging radiation. Once the radiative properties are calculated for a fixed dopant concentration value and different temperatures ranging from 300 K to 1273 K, these are mediated over the wavelength range of 0.4 – 20 μm using the black body spectral distribution emission at a temperature T_b which, in this case represents the temperature of the graphite element. During the ramp up and cool down processes however, both the heater element and the wafer vary their temperature and so in turn the optical properties. In these condition it is thus difficult to define a unique integrated optical property which is valid over the useful temperature range for epitaxial deposition, as the temperature over which the optical properties are mediated also changes. In order to assess the influence of the mediating temperature T_b , the optical properties have been calculate as function of the dopant concentration, the mediating temperature T_b and the temperature of the wafer. In Fig.(5.8) are presented the results of reflectivity value for a lightly p-type wafer. As expected, the optical properties for a low dopant concentration change drastically over the mediating temperature T_b range. As the temperature of the wafer increases, the sensibility of the wafer optical properties to the mediating temperature diminishes and ideally for high wafer temperatures, it became nearly independent from the wafer temperature. As described in detail infact in chapter 4, an increase in temperature generate more free electrons in the conduction band and thus the free-carrier absorption mechanisms are enhanced. At these temperature the wafer become nearly opaque to the incoming radiation. On the other hand, the radiative properties of heavely doped wafer results almost independent from the mediating temperature in the range of interest. In this case the free-electron absorption is enhanced by the donor or acceptor species which increase the density of free carrier in the conduction band, or valence band for holes. Thus, in the case of heavily doped wafer or for high wafer temperature, the optical properties are integrated for a temperature value and then assumed being constant with good approximation over the temperature range of 300 K to 1273 K. On the other hand, for light doped wafers it is necessary to maintain constant the mediating temperature, i.e. the temperature of the heating element. This means that in simulations the initial temperature of the graphite meander are imposed as the same experienced after the equilibrium for a particular value of input power. This operation conditions are not so far from the real operative conditions experienced during epitaxial processing of several wafers, as the generally the wafer are introduced into the UHV chamber after the heating element has just reached the quasi-equilibrium temperature.

5.4 Numerical Model

The first step is represented by modeling and validation of the heating stage model in case the wafer and the subsceptor are not considered. This modeling step is of paramount importance in order to achieve a detailed finite element (FE) model of the radiative power distribution impinging onto the wafer independently from the various physical and radiative substrate properties. Afterwards, the wafer and the subsceptor are included into the finite element model in order to assess the thermal behavior of the entire stage as a function of the radiative properties of the particular substrate considered.

All the finite element analysis in this work have been performed using the commercially available software ADINA 8.7. The software is indeed capable of solving highly non-linear problems in which the radiative, thermal and electrical properties of the materials also change as a function of the temperature. The radiative heat exchange between surface elements is included into the finite element model by applying particular boundary conditions (BCs) which define the portions $\bar{s}$, $\bar{d}$ and $\bar{t}$ of the incoming radiation that is specularly and diffusely reflected, and trasmitted respectively. It is thus assumed that radiative absorption is localized in the surface region. In case of the silicon wafer, the thermal resistance evaluated between the upper and lower surfaces is sufficiently low to employ this assumption as a good approximation. The three parameters $\bar{s}$, $\bar{d}$ and $\bar{t}$ can be constant, time-dependent or temperature dependent. The emissivity value ε is then calculated using the Kirchhoff's law of radiation. The transmitted energy could be lost to the environment and not traced in the solution, or could arrive at the next radiative boundary and be reflected again. In addition, the specularly reflected energy is calculated in the solution algorithm by tracing the reflected ray of energy. The radiative exchange for all the surfaces involved is then solved by using the *radiosity algorithm* [5.1]. Detailed description of the numerical algoritm can be found in Ref [5.2]. The rate R of outgoing radiant energy per unit area can be expressed balancing the energy absorbed or emitted from the environment, and the transmitted and diffusely reflected energy

$$R = \varepsilon R_e + \bar{t}\bar{f}R_t + \bar{d}G \tag{5.2}$$

where R_e and R_t are the energy from an external radiation source and the energy transmitted into the environment respectively, G is the rate of all incoming radiant energy per unit area, $\bar{f}$ is the shape factor which depend both on the radiative properties of the

material and the geometrical configuration evaluated at each node. The rate of incoming energy G evaluated at the boundary element k can be expressed as the sum of all rates of outgoing radiant energies from all radiation boundary elements

$$G_k = \sum_l \int_{S_l} F_{kl} R_l dS \tag{5.3}$$

where S_l is the area of the boundary element l and F_{lk} are the view factor matrices which are calculated using the ray tracing technique based on Lambert's law and can be expressed as Eq. (3.6). This matrix have thus dimension equal to the number of radiative boundary conditions involved in the radiative heat exchange. By substituting Eq. (5.2) into Eq. (5.1) and applying the discretizing Galerkin method, it is possible to obtain the finite element radiosity equation governing R

$$\int_S h^\theta (\ R - \varepsilon R_e - \bar{t}\bar{f} R_t - \bar{d} G) dS = 0 \tag{5.4}$$

where the Eq. (5.1) is weighted by the term h^θ which is the virtual temperature quantity on the boundary. After the R value is known and G has been calculated using Eq. (5.2), the heat flux load can be found balancing the energy on the surface as $Q_n = \int h^\theta \big(\varepsilon(G - RtdS$.

5.4.1 Heating element FE model

A detailed 3D geometrical representation of the graphite element have been first developed within the FE environment. The two electrodes and the refractory metals protective elements have been discarded from the FE model as no thermal data regarding the behavior in the vacuum environment during the heating process can be retrieved. Due to UHV conditions infact, the thermal contact resistance can play a decisive role on the thermal behavior of joined components by changing drastically the temperature profile that would be expected in atmospherical conditions. The heater thus is then considered floating, so no heat dissipation by thermal conduction have been considered, while the influence of the two electrodes on the temperature profile of the heater mender is evaluated by the steady-state gradient measurements described in Section 5.2.1. This means that the simulated relative temperature drop between the center and the edge of

the heater element will reflect the real conditions, while the absolute temperature that is found by FEA is expected to be higher respect to the measurements. For the same reasons, also the refractory metal enclosure have been modeled as a thermally floating element which exchange heat with the other elements only by radiative processes. Finally, the chamber walls have been included into the numerical model by adding a closed cave cylinder enclosure which contains both the graphite element and the refractory metal enclosure. The height of 100 mm and the radius of 150 mm have been set by evaluating the minimum dimensions which have influence on numerical results.

In order to simulate a constant temperature wall which is independent from the inside thermal condition, a Dirichlet boundary condition with temperature $T_w = 373$ K have been imposed on the inner surface of the chamber while the outer ones have been considered as adiabatic. Further, a radiative boundary condition consisting of $\bar{s} = 0.4$, $\bar{d} = 0.4$, and $\bar{t} = 0$ has been applied to the inner surfaces of the chambers. The self heating due to the Joule heating process is included into the numerical model by adding the Joule term $(\boldsymbol{J} \cdot \boldsymbol{J})/\sigma_h$ to the heat generation term of the heat transfer equation, where $\boldsymbol{J}$ is the applied current density and σ_h is the electrical conductivity, while the electric potential φ is found by using the *steady-current conduction analysis* which solve the Poisson's equation in the form

$$\nabla \cdot (\sigma_h \nabla \varphi) = \nabla \cdot \boldsymbol{J} \tag{5.5}$$

A constant current density $\boldsymbol{J}$ which is related to the input power is applied as a boundary condition to surfaces which correspond to the position of one electrode, while a constant potential of $\varphi = 0$ have been applied on the other electrode. The radiative boundary condition which correspond to a diffuse reflectance of $\bar{d} = 0.2$ and zero transmissivity and specular reflection, have been applied to the upper, the lower, and to all the external sides surfaces of the heater element. The side surfaces which face the bights created by the coils has been instead considered adiabatic. The high aspect ratio between the spacing and the height of the coil, i.e. corresponding to about 1:4, allows to neglect the radiation emitted towards the environment, which is a small fraction of the total power emitted by the graphite element. The error caused by this approximation, assessed by finite element simulations, determine a temperature variation of the centre of the mender less than 1°C, which confirm the goodness of the approximation. On the other hand, a radiative boundary condition which consists of $\bar{s} = 0.9$ and $\bar{d} = \bar{t} = 0$, have been applied to all the

surfaces of the thermal shield due to high specular reflectance of the refractory metals surfaces.

The heater element have been then meshed using an unstructured mesh with 3D brick elements of the second order. A first grid independence study have been performed by evaluating the current density through the coils, resulting in a total amount of 7496 three-dimensional elements. Fine mesh refinements have been required for the coil bends and for the electrodes regions due to high current density gradients. Similar unstructured 3D mesh comprised of brick elements have been adopted for the thermal shield, which results in a total amount of 1675 three-dimensional elements after the grid independence study based on the evaluation of the maximum temperature reached in steady-state conditions. The reactor chamber enclosure instead, have been represented by using the *shell thermal conduction* formulation and thus they have been represented numerically with 2D triangular elements of the second order. Grid independence study have been performed by evaluating the variations in the mean temperature of the upper surface of the graphite mender. As a result, a mesh grid composed by 250 elements have been adopted.

The fitted thermal conductance k_h whom dependence on temperature is expressed by Eq. (5.1) have been applied to the heater element, while the specific heat capacity $c_{p,h}$ is an unknown parameter which will be fitted using the transient temperature measurements. The variation of the electrical conductance have been also taken into account by measuring the resistivity of the graphite heater in several steady-state conditions. The relative electrical conductance σ_h of the graphite material used in the heating stage have been fitted for each current density step, by matching the simulated voltage drop across the meander with the experimental measurements. Regarding the thermal shield, a typical thermal conductance $k_s = 135\ W/mK$ of the molybdenum have been used and is considered independent from the temperature, while the specific heat capacity $c_{p,s}$ is also an unknown parameter which is necessary to be fitted using the experimental measurements. By qualitatively analyzing the transient curves, two contributions due to either the heater element and the thermal shield can be identify along the temperature curve. In case of the 0 % - 30 % power transition curve, the first portion is expected to be due mainly to the graphite element as it experience the severe heat flux caused by the Joule heating process. In the same portion, the thermal shield absorbs a little portion of the radiation emitted by the graphite heater, and thus experiencing a slower temperature ramp up process. Furthermore, the thermal mass and the emissivity value of the thermal

shield are both too low to influence significantly the heating ramp of the mender and thus in this condition it acts as a reflector of the radiative power. After the heater have reached an equilibrium state, a further increase of the temperature is necessary due to the thermal shield which continue its ramp up process. As expected, the specific heat capacity $c_{p,h}$ have a strong influence on the first part of the curve by determining the slope of the curve while only after about 450 s the thermal shield begin to influence the heater temperature profile by creating a nearly constant slope which is directly linked to the $c_{p,s}$ parameter.

A fitting study of the two unknown parameters have been thus developed by evaluating the deviation of both the absolute and the derivate values from the experimental measurements. First, the thermal shield have been kept at fixed temperature $\bar{T} = 500$ K by imposing a Dirichlet boundary condition on the inner surfaces of the refractory metal enclosure, while the $c_{p,h}$ value has been tune in order to find the best fit with the experimental curve. The equilibrium temperature of the graphite mender reached in these condition is about 996 K. Using this approach, the constant value $c_{p,h} = 1.21\ J/g \cdot K$ give a maximum derivative deviation of about -0.077 °C/s and a maximum absolute temperature error of +3°C up to about 250 s. Due to this $c_{p,h}$ value, the heater element takes up to about 315 s to reach the 95 % of the equilibrium temperature. Afterwards, the $c_{p,s}$ values has been tune ranging from 0.1 $J/g \cdot K$ to 1.7 $J/g \cdot K$ in order to match the behavior of the last part of the transient curve. As described earlier, a negligible influence is assessed on the first portion of the curve, generating a maximum temperature variation of 0.3°C. At last, the specific heat capacity value $c_{p,s}$ = 1.5 $J/g \cdot K$ best fits the experimental curve, with a maximum derivative deviation from the experimental measurements of 0.06 °C/s up to 700 s.

The resulting finite element model is then capable of matching the experimental transient curve which regard the 0% - 30% power transition with a maximum error of +4°C. As expected, the numerical results are higher than the measured ones as the heat dissipation through the two electrodes have been neglected. The accuracy of the FE model have been then tested by extending the simulation time range in order to validate the numerical results for different current densities. In Fig (5.9) are presented several comparison between simulated and experimental measurements regarding absolute and derivative values. Even in this case, the simulated results well suit the experimental transient behavior within an absolute temperature deviation of ± 10 °C and thus can be considered as a good numerical approximation of the heater element. The deviation in particular

result larger as the current density diminishes, probably due to a variation of the chamber wall temperature during the pyrometer measurements.

5.4.2 Complete Heating Stage FE model

The 3D geometrical representation of the subsceptor and the wafer have been included into the heating element FE model. Due to the low contact surface between the subsceptor and the three pint-point sustains, the heat dissipation by thermal conduction through the sustains have been neglected, while the wafer is considered in contact with the subsceptor. The two element thus are considered thermally floating, and heat exchange with the other element within the chamber is only through radiative processes.

The radiative boundary conditions have been imposed supposing that amorphous germanium have been deposit on the subsceptor surface. Thus a temperature constant radiative condition composed by of $\bar{s} = 0$, $\bar{d} = 0.54$, and $\bar{t} = 0$ have been imposed on all the surfaces of the subsceptor. The data have been extracted from Ref. [5.4] while the transmitted radiation portion have been supposed being totally absorbed by the subsceptor so it have been included into the emissivity term. On the other hand, the radiative boundary conditions for the upper and the lower wafer surfaces have been calculated using Eq. (5.5) in which the absorption a_λ, reflection ρ_λ and transmission τ_λ terms have been evaluated using the optical properties calculation results described in section [5.3]. The quasi steady-state equilibrium have been simulated supposing that the initial temperature conditions of the graphite heater correspond to these experienced in the quasi steady-state equilibrium which has been found with FE model described in Section 5.4.1. The temperature of the meander reached in these conditions has been thus also used as the temperature T_b for which the radiative properties are mediated.

An unstructured mesh composed by 3D brick elements of the second order have been used for both the subsceptor and the wafer. Due to the high thermal resistance in the contact region of the wafer with the subsceptor, high thermal gradient are expected and thus a fine mesh refinements for this particular region is mandatory. A grind independence study have been performed on both elements by evaluating the peak and medium temperature, resulting in a total amounts of 742 and 570 three-dimensional elements for the wafer and the subsceptor respectively. The specific heat capacity $c_{p,sb}$ and the thermal conductivity k_{sb} of the subsceptor have been retrieved from the

Suprasil® 1 technical datasheet data [5.5] while the silicon thermal conductivity k_{Si} have been modeled as a function of temperature by interpolating the empirical data in the range of 20°C to 100°C

$$k_{Si} = 4.422 \times 10^6 \cdot T^{-1.856} + 28.94 \tag{5.6}$$

The value of the silicon heat capacity $c_{p,Si}$ instead experiences a relatively small variation within the same temperature range, thus a constant value of 830.7 $J/Kg \cdot K$ has been adopted. The thermal contact resistance have between the wafer and the subsceptor have been evaluated extrapolating the experimental data measured by Nishino *et al.* [5.7]. For 390 μm thick silicon wafer, the mean weight can be evaluated as 7.14 g, assuming a density of 2.33 g/cm^3 and a 4" silicon wafer. Due to deformations induced by temperature gradients, the calculation of the contact area instead is a tough task. Assuming a contact area which is half respect to the ideal one, i.e. a disk of 2 mm radius, the contact pressure value has been assessed below the value of 10^{-5} MPa, and thus the correspondent contact conductivity value has been estimated of about 1 W/(m^{2}K).

The complete numerical model have been first validated using the measurement data retrieved using the pyrometer. In Fig. (5.13) is plotted the transient behavior of the complete stage model in case an input power of 30% is applied to the heater element. The temperature have been retrieved from the centre of the wafer surface. The experimental data are well fitted by the numerical results, which deviate of about 18°C at 260 s from the experimental measurements while discrepancy diminishes as the time proceed. The positive sign of the error can be ascribe to the thermal contact resistance, which have been roughly estimated from literature. Due to the casual nature of the surface roughness, the contact resistance should be measured experimentally in order to obtain a very good agreement with real data. Real rough surfaces inface have general a contact area which is estimated less than 5%. Furthermore, within vacuum conditions, the lack of a thermal conductive gas exasperate the problem, as the heat can be exchange between solids only by conductive or radiative heating. At the end of the transient, the absolute error between the numerical data and the experimental measurements is about 9°C, while the derivative deviate from that of experimental transient curve of about +0.5 °C/s.

The numerical model highlights the weak aspects of the heating stage which is employed within the LEPECVD reactor. First, the temperature gradient along the heater element has been assessed being over 100 °C and increases as the input power increases. This have a

worsening effect on the induced temperature profile of the wafer, which also show a maximum temperature gradient of 50°C. This high gradient value can influence the epitaxial processes which occur onto the substrate surface. In Fig. (5.10) is shown the temperature profile simulated for the heating element in case an input power of 30% is applied. The presence of a region of the heating element near the electrodes which is not crossed by the current, worsen even more the effect as it acts as a heat sink. By this, a large temperature gradient is set up from the center of the mender toward the border. In the inverted heating stage furthermore, the effect of temperature unevenness on the heating element have a deep worsening effect on the temperature profile induced on the wafer, which also experiences a maximum temperature drop evaluated from the center to the edge of about 57 °C. This value is also confirmed by the experimental measurements conducted using the instrumented wafer. Thus, a re-engineering of the heating shape and configuration is thus mandatory in order to gain a better control and profile uniformity along the wafer surface. In particular, the regions near the two electrodes which are not crossed by the electric current, experience a lower temperature values as they act as a heat sink which dissipate the heating generated in the region nearest to the centre of the meander. By this FE model, thus it is possible to design the heating element and eventually the back reflector in order to modulate the spatial distribution of the radiative power impinging on the wafer surface in order to minimize the temperature gradients.

The simulation of the temperature profile along the wafer surface show also the that two different temperature gradients are present along the axis directions. In Fig. (5.11) is shown the temperature profile of a *p*-type silcon wafer in case of 30% power applied to the heating element. The simulated results are in good agreements with the experimental measurements with a maximum absolute discrepancy of ± 2 °C. In the case of inversed heating stage deposition, the temperature gradients are less severe and even more uniform along the two principal axis.

References

[5.1] J.P. Holman, *Heat Transfer,* 4th ed., McGraw-Hill, 1976

[5.2] ADINA R&D, Inc., *ADINA Theory and Modeling Guide*, May 2009.

[5.3] ' Report of the Ad Hoc Committee on Refractory Inorganic Nonmetallic Structural Materials ', *MAB Report,* 169-M, January 1961

[5.4] H. Madura, H. Polakowski, B. Wiecek, ' Spectral emissivity evaluation for material used in microelectronics ', *QIRT '96 Eurotherm Series 50,* 1997

[5.5] *Quartz Glass for Optics, Data and properties,* Heraeus Hoding GmbH.

[5.6] T.P. Merchant, J.V. Cole, K.L. Knutson, J.P. Hebb, K.F. Jensen, ' A systematic approach to simulating rapid thermal processing systems ', *J. Electrochem. Soc,* **vol.** 143 (1996), p. 2035

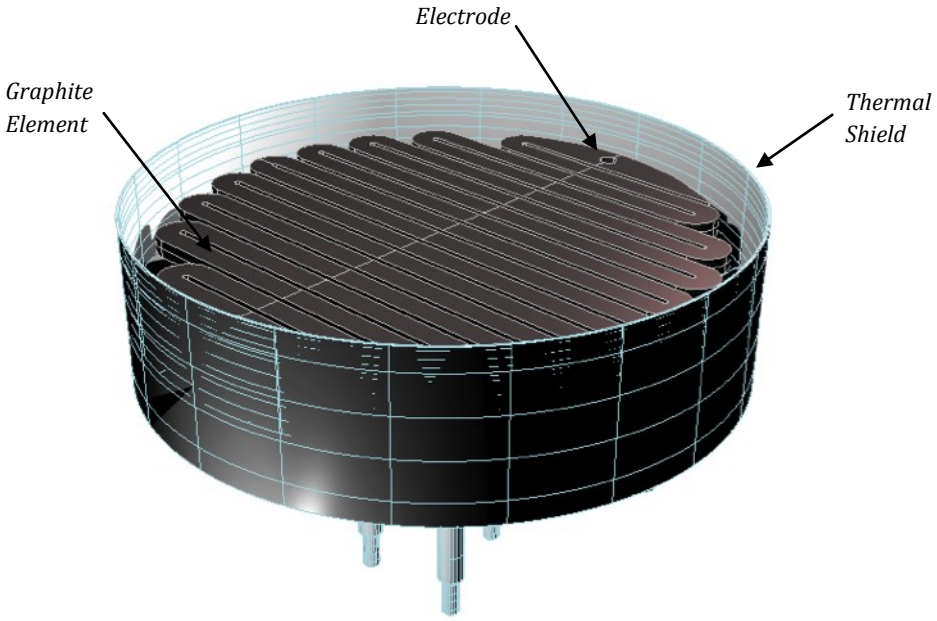

Fig. 5.1 Schematic 3D represantation of the Wafer Heating Stage of the LEPECVD reactor.

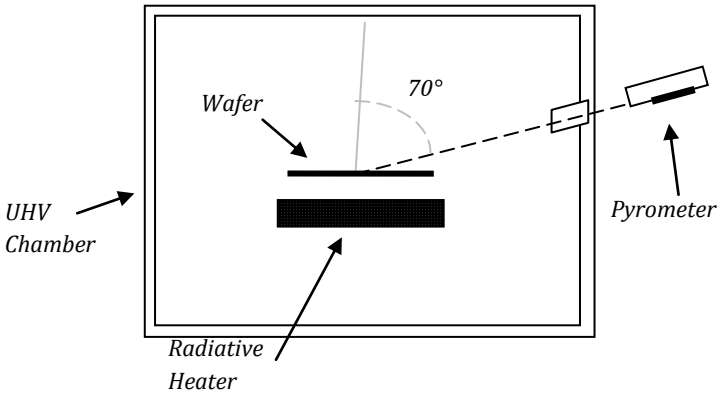

Fig. 5.2 Schematic representation of the experimental set up for wafer temperature optical measurement.

Metis M09 Digital Pyrometer Technical specifications	
Measuring wavelenght λ_p	*950 nm*
Temperature range	*400 – 1200 °C*
Spot size diameter	*1.30 mm*
Response time t_{90}	*< 1 ms, adjustable to 10 ms*
Temperature resolution	*< 0.1 % of adjustable temperature range*

Tabel I Summary of the technical properties of the Metis M09 pyrometer.

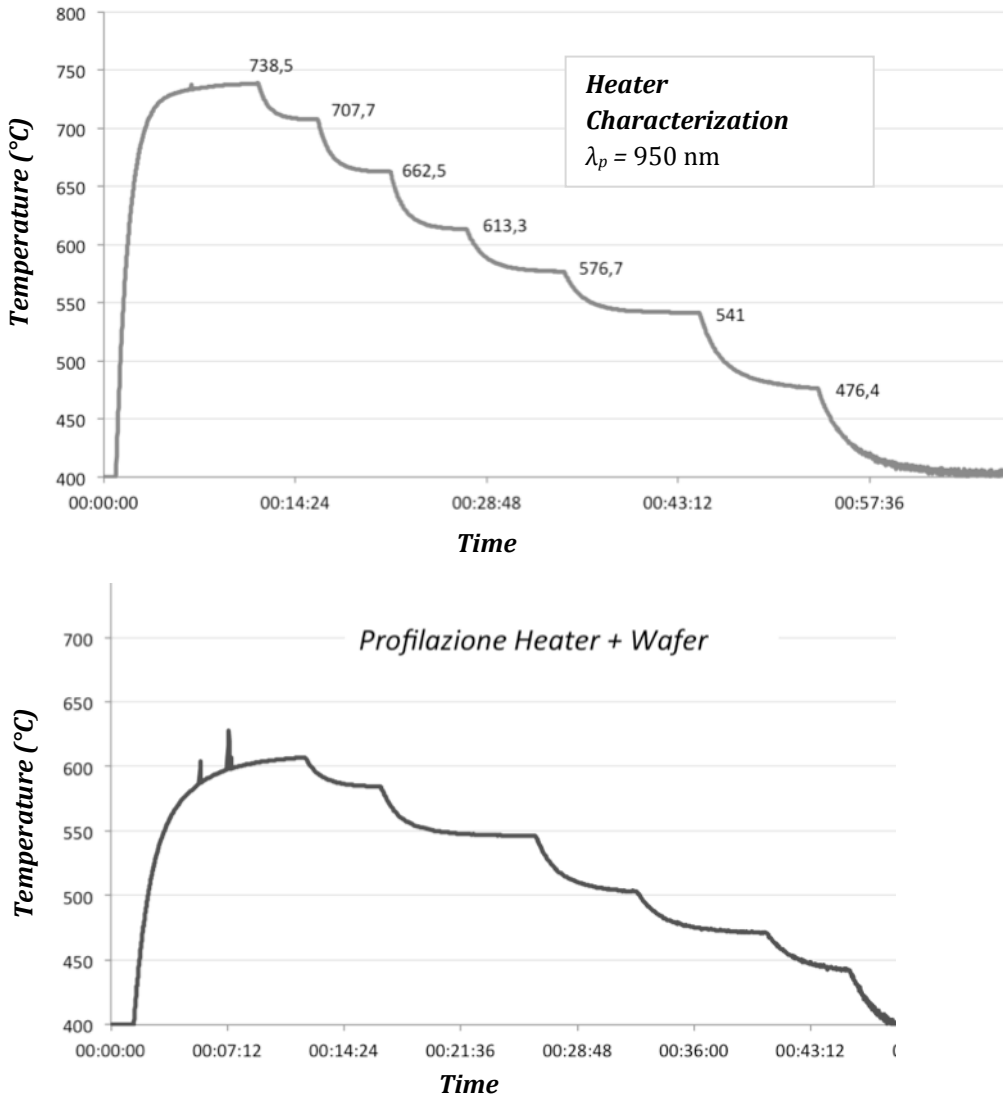

Fig. 5.3 Optical transient measurements of the graphite heating element (*above*) and the highly doped p-type silicon wafer (*below*) temperature.

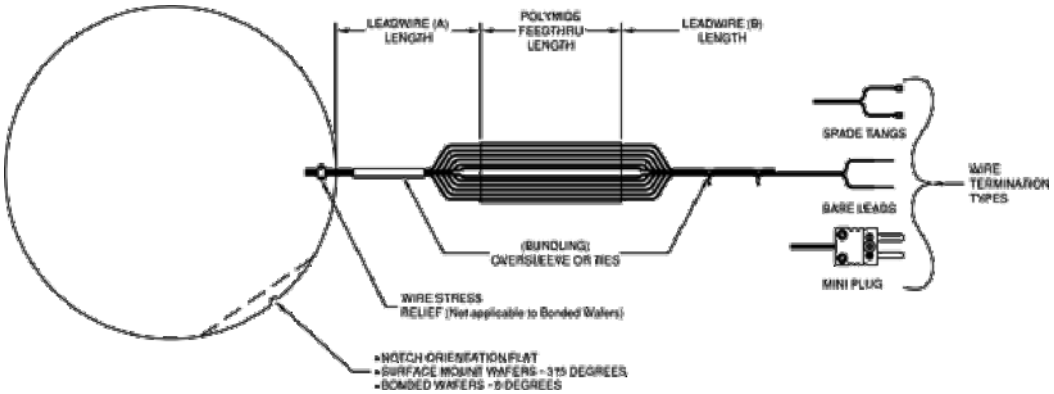

Fig. 5.4 Schematical representation of the instrumented wafer used for the temperature profile measurements (*Courtesy of ThermoElectric Company)*

Heater Power	Maximum temperature gradient	Heater Power	Maximum temperature gradient
10%	*6 ℃*	*25%*	*30 ℃*
15%	*15 ℃*	*30%*	*35 ℃*
20%	*25 ℃*	*40%*	*57 ℃*

Tabel II Summary of the temperature gradient measurements using the ThermoElectrical Company instrumented wafer. The temperature drop has been evaluated between the center and the edge of the wafer surface.

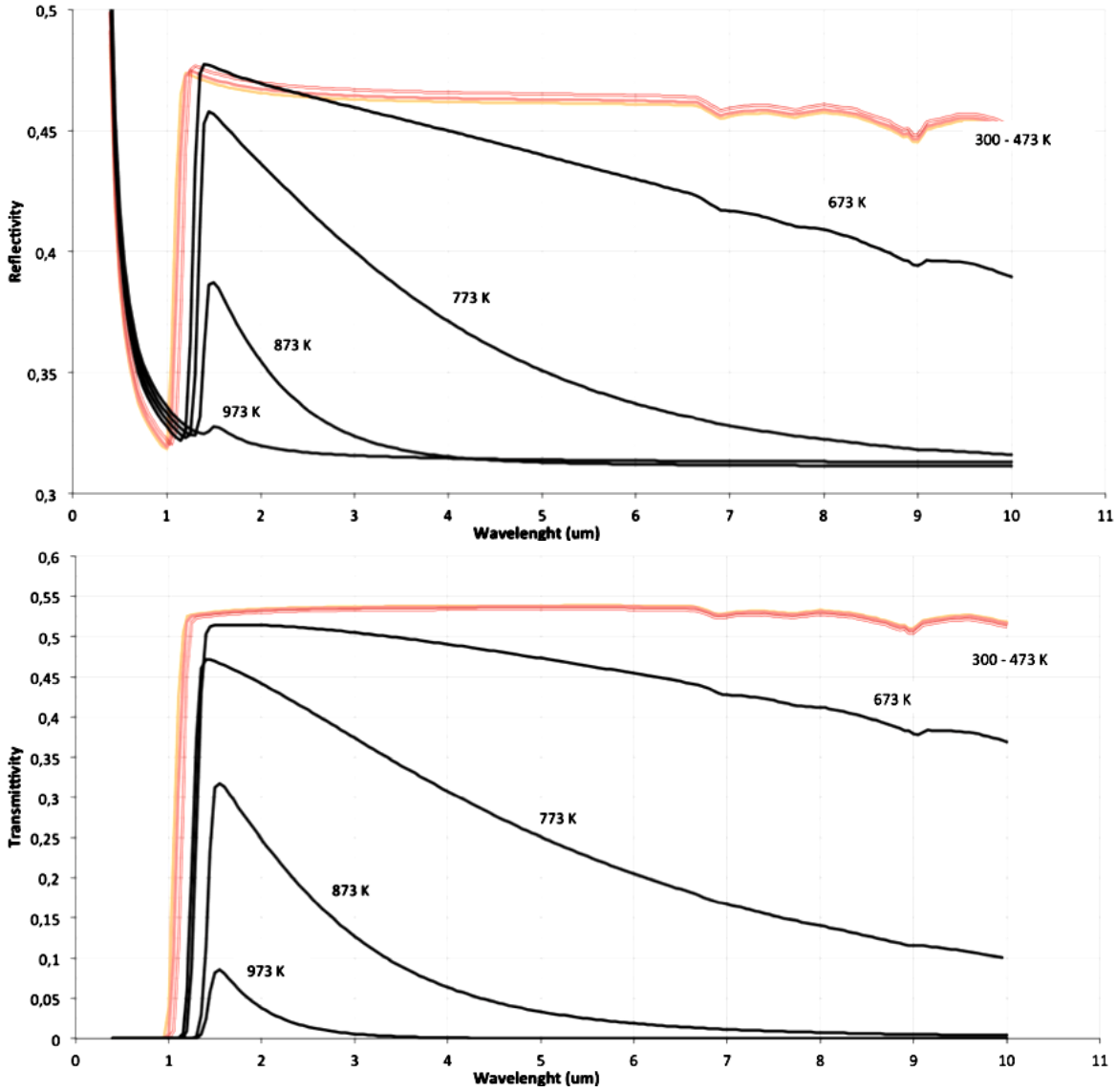

Fig. 5.6 Calculated Reflectivity and transmissivity values for a 390 $\boldsymbol{\mu m}$ thick lightly doped silicon wafer. A *p*-type wafer with dopant concentration of $\boldsymbol{N_A}$ = 10^{15} cm^{-3}. The calculations have been performed using the Drude model described in chapter 4.

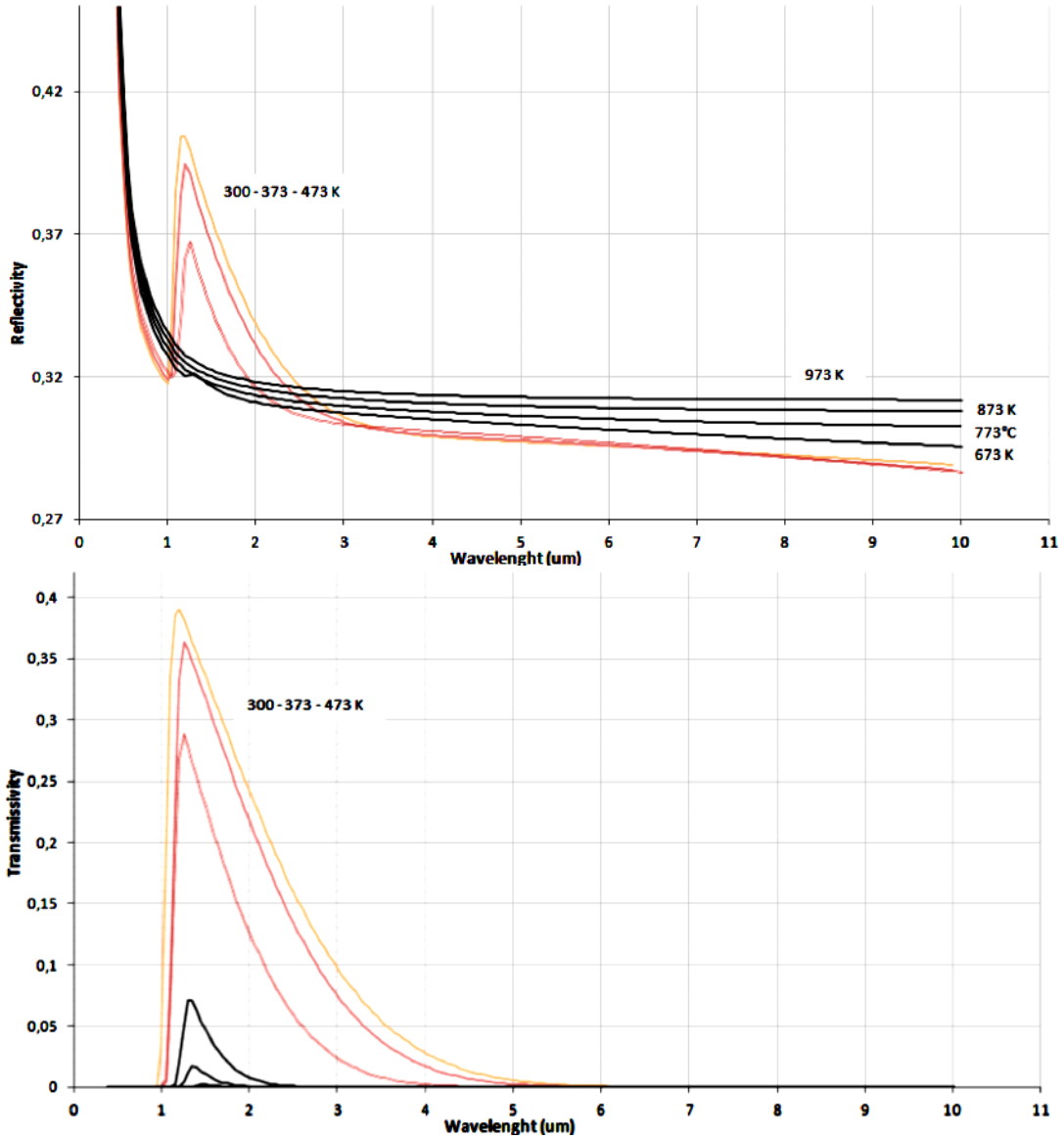

Fig. 5.7 Calculated reflectivity and transmissivity values for a 390 $\boldsymbol{\mu m}$ thick heavily doped silicon wafer. A *p*-type wafer with dopant concentration of $\boldsymbol{N_A}$ = 10^{19} cm^{-3}. The calculations have been performed using the Drude model described in chapter 4.

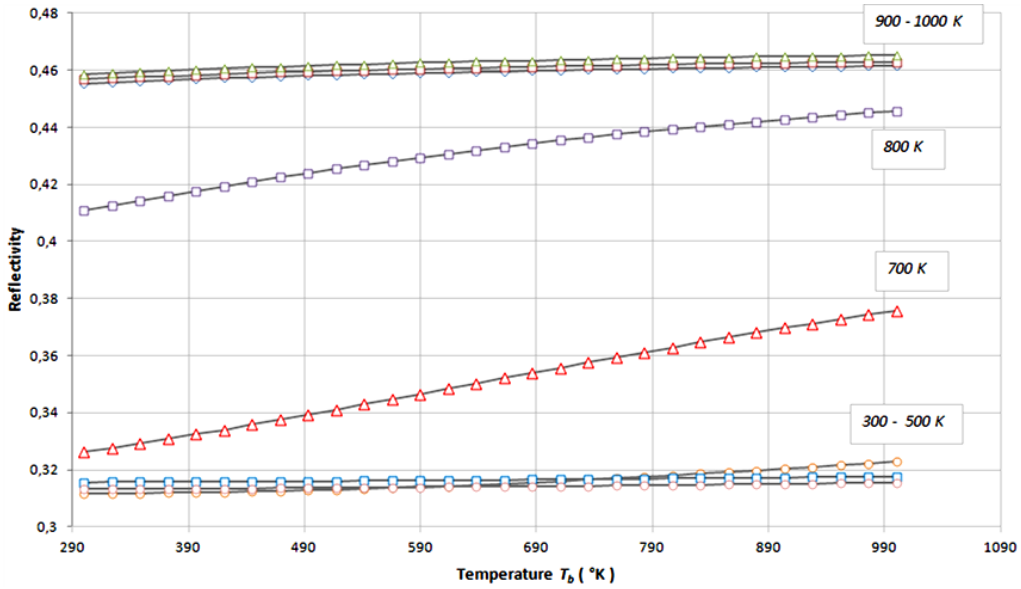

Fig. 5.8 (***above***) Calculated reflectivity integrated values plotted vs the value of the mediating temperature as a function of the substrate temperature for *p*-type silicon wafer with dopant concentration of $N_A = 10^{15}$ cm^{-3}. (***below***) The integrated reflectivities and transmissivities integrated values using the mediating temperature $T_b = 1000$ K. The values have been plotted as a function of the wafer temperature.

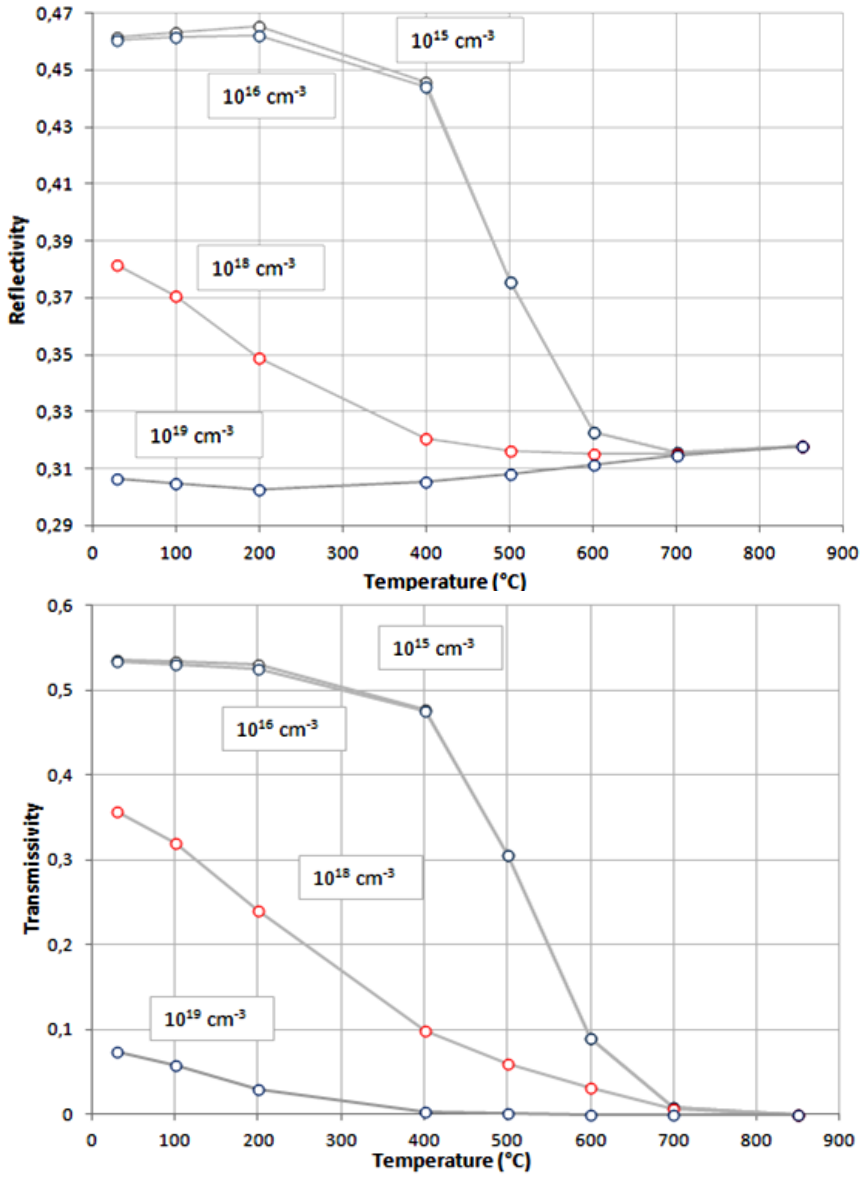

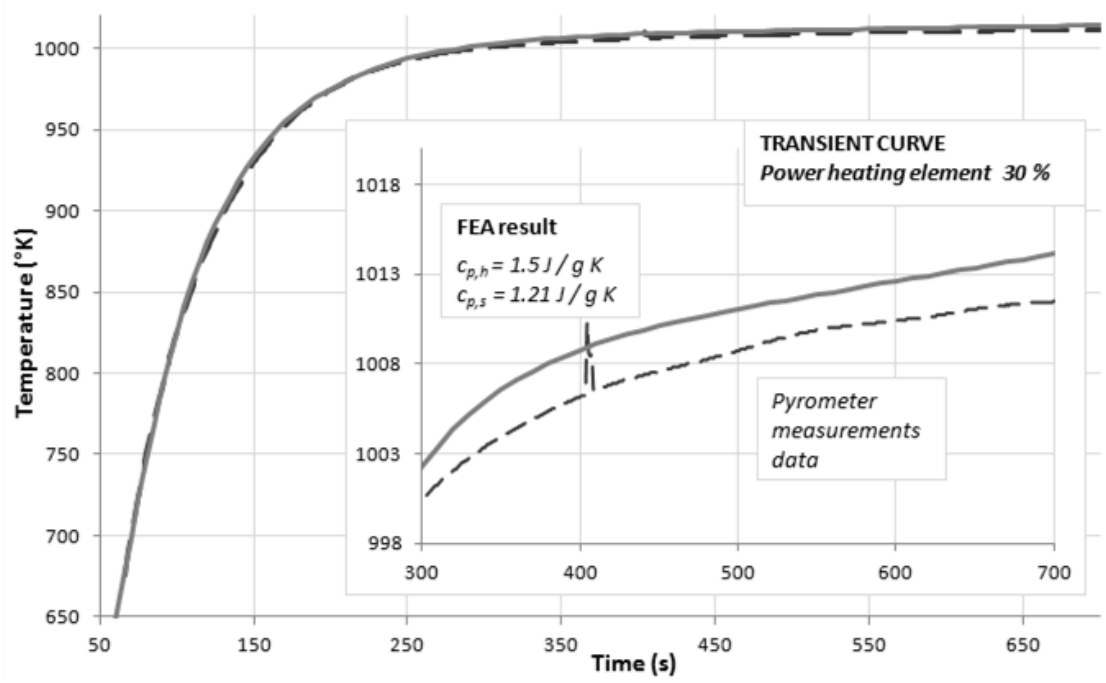

Fig. 5.9 Plot of the experimental measurements (red line) and the numerical results of the temperature transient profile of the heating element for different value of $c_{p,s}$ and $c_{p,h}$. The dotted line represent the temperature transient of the thermal shield.

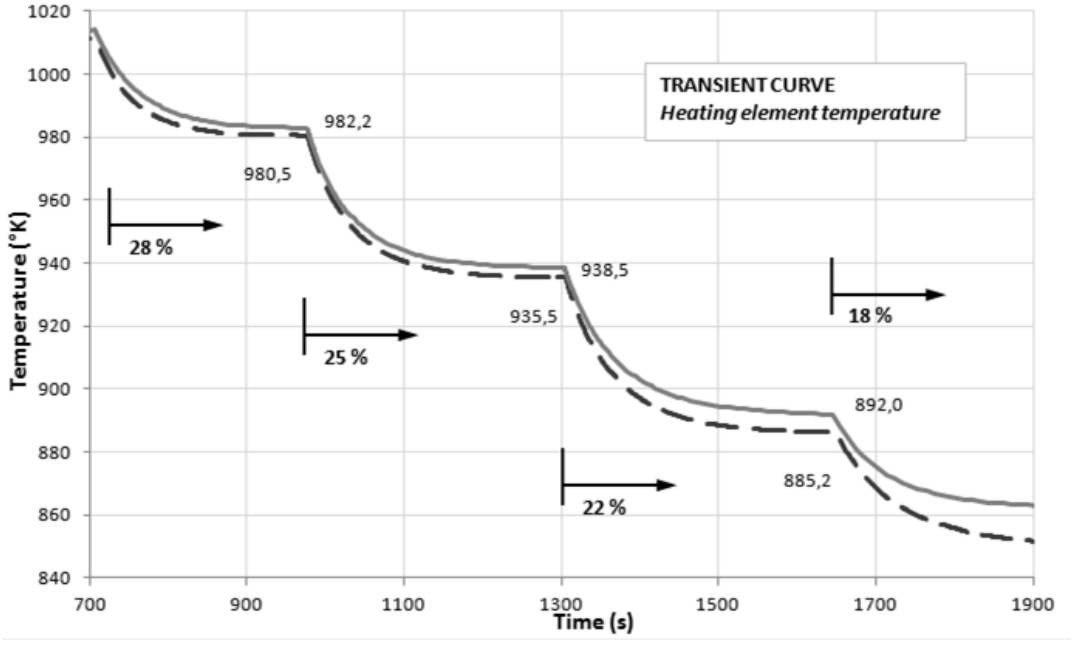

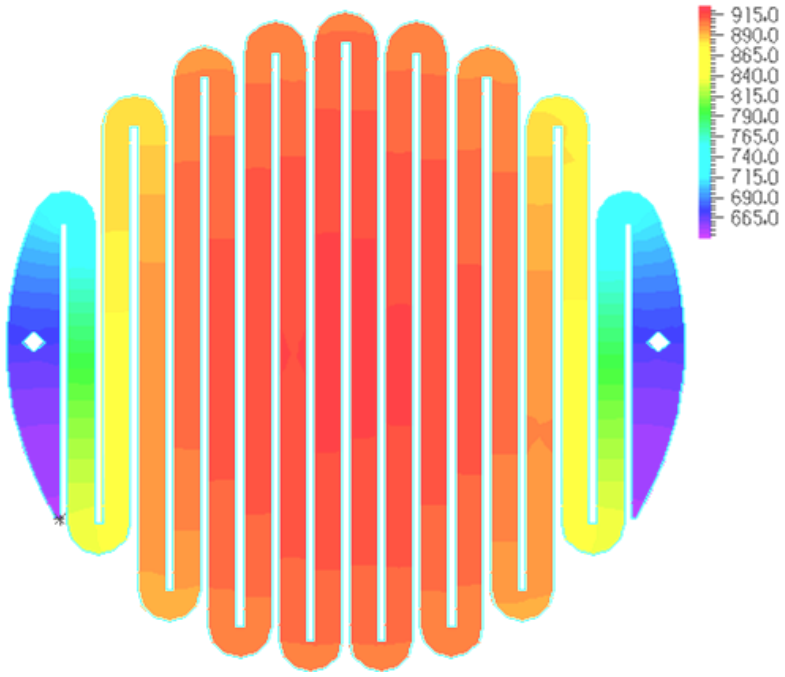

Fig. 5.10 Temperature profile for the graphite heating element during ramp up process for a 28.1 A current. The presence of a large regions near the electrondes which is not irrorated by electric current cause severe ovelall temperature drop between the center and the edge.

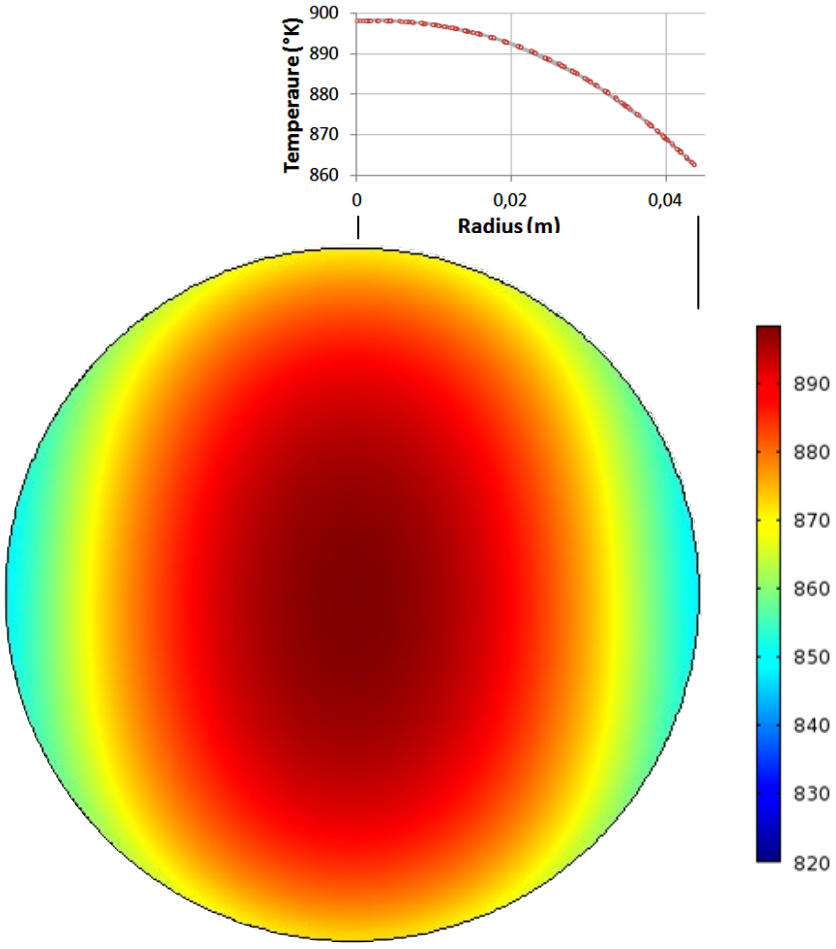

Fig. 5.11 Temperature profile map along the p-type wafer surface in case the graphite element is powered with 28.1 A. The dopant concentration is N_A = 10^{19} cm^{-3}. The radiative power unevenness cause an asymmetric temperature drop along the two axis.

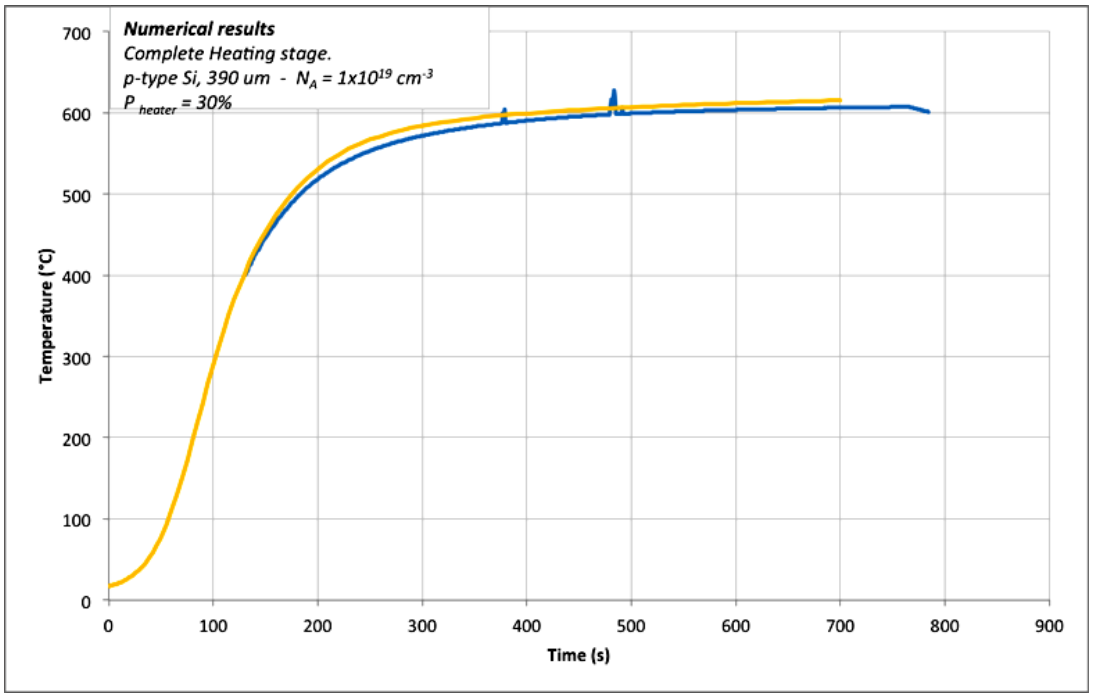

Fig. 5.12 Plot of the experimental measurements (blue line) and the numerical results of the temperature transient profile of a p-type wafer with a dopant concentration of $N_A = 10^{19}$ cm^{-3}. The heating power of the graphite element has been set to 30%.

CHAPTER 6
LEPECVD deposition results

6.1 Sample preparation

A wide range of epitaxial depositions, which consist of both hetero- and homoepitaxy depositions of Silicon and Germanium have been carried out in this work. Additionally to the plasma assisted LEPECVD technique, also several samples have been grown using the thermally driven UHVCVD technique in order to investigate the possibility to exploit different growth modes for the development of heterostructures which are not achievable using the plasma enhanced deposition. Thus, both monocrystalline Si and Ge wafers have been used as a substrates for epitaxial depositions.

For the Ge/Si heterostructures and Si homoepitaxy, 4" *p*-type Silicon (100) wafers with a 6° off-cutted surface toward the <111> planes have been used. The wafers are single polished surfaces and resistivity of 0.2 – 0.002 Ωcm, which result from a Boron dopant concentration of about 10^{19} cm^{-3}. Before loading into the reactor, the SiO_2 native oxide have been removed from the surface by means of a 1.5% HF dip. For 5 min. Before each deposition, a 75 nm Si buffer layer is grown at 600°C for surface contaminant suppression. On the other hand, epi-ready Ge (100) substrates have been used for Ge/Ge homoepitaxy depositions. After loaded into the load-lock module, the wafer are first heated at 200°C for 10 min using IR lamps in order to promote eventual water desorption. A subsequent annealing process at higher temperature have been performed in order to remove the hydrogen passivation layer adsorbed on the surface. After each deposition process, the chamber walls have been cleaned using Ar/CCl_4 gas mixture in order to avoid re-

deposition of the Si or Ge layer from the chamber wall onto the substrate during the subsequent epitaxial process.

6.2 LEPECVD characterization

A first set of depositions have been carried out in order to assess the influence of the tunable process parameters on the epitaxial process. These regards in particular the plasma glow discharge power P_W, the chamber pressure $\bar{p}_d$, the precursors and plasma activation gas inlet flow and the temperature of the substrate, which have strong influence on the behavior of the deposition processes. As described in Section [2.1] for example, a variation in the discharge power P_W and the chamber pressure $\bar{p}_d$ can result in a modulation of the electron energy distribution $f(E)$ within the plasma environment and the mean free path λ of the ions, which in turn may influence the energy of the ions bombarding the substrate, the dissociation rate of the gas species injected into the reactor, or alter the behavior of the adatoms nucleation and diffusion processes on the substrate surface. In this section, the different experimental condition investigation performed on the LEPECVD reactor are described and characterized.

The first set of measurement regards the influence of the deposition parameters on the growth rate of the epilayers film. In Fig. (6.1)a is plotted the variation of the growth rate as a function of the substrate temperature in the range of 300°C and 700°C, while keeping constant the chamber pressure and the precursor gas flow. An Ar flow of 25 sccm have been injected into the plasma source as to ignite the plasma glow discharge. As described also by other works in literature [6.1, 6.2, 6.3], the growth rate do not depend significantly on the temperature within the range useful for SiGe epitaxial deposition, i.e. 300°C to 800°C. This is mainly the results of the plasma dissociation processes of the precursors, which allows to unlink the substrate temperature variable to the dissociation rate of the precursor species. In this case, the maximum variation is of about 8.3 %, which results an order of magnitude less than the thermally activated CVD deposition processes. Thanks to this, it is thus possible to modulate the substrate temperature independently from the growth rate, in order to influence only the growth modes of the epilayers. Even if not at the maximum plasma power, the deposition rate of Ge onto Si is as high as $g_{Ge} = 50$ nm/min. This good results is the product of both the enhanced precursor dissociation and the efficient hydrogen desorption from the substrate surface [6.2]. The plasma enhance the mobility of the species adsorbed onto the wafer surface while the ions bombarding the

surface boost the desorption of the hydrogen atoms. The activation energy E_a calculated using the Arrhenius shown in Fig.(6.2) plot result of 9.64 $kcal \cdot mol^{-1}$, which is comparable with the diffusion activation energy for the GeH_4 precursor of 4.3 $kcal \cdot mol^{-1}$ [6.4]. This suggest that the process is mass transport limited. The constant activation energy also at temperatures as 350°C suggest also that the dissociation of precursor can be assumed independent from the substrate temperature. Compared to the results obtained with LPCVD technique [6.5] in the same temperature range, i.e. 7 nm/s at high temperatures, the growth rate obtained using the LEPECVD reactor is at least 5 time higher.

The greatest influence on the growth rate instead is represented by the precursor gas flow. In Fig. (6.1)b is represented the growth rate as a function of the precursor gas flux of silane and germane. Even if the MFCs allows to achieve precursor flow as high as 100 sccm, the characterization have been performed only up to 35 sccm as in the first configuration of the reactor we found that the employed scroll pump was not able to sustain high precursor flow rates. From the measurements results that in case of homoepitaxy of silicon, the growth rate is comparable with the Ge heteroepitaxy at the same conditions described earlier. An increment of the plasma glow discharge power P_W from 1 kW to 1.6 kW while keeping constant all the other parameters, give rise to a correspondent increase of the growth rate g_{Ge} from about 40 nm/min to 55 nm/min. On the other hand, for a fixed power P_W of 1.6 kW an increment of the GeH_4 gas flow to 30 sccm results in a growth rate $g_{Ge} = 72.2$ nm/min. This means that is possible to growth 1 μm thick layer of Ge onto a Silicon substrate in about 13 min. However, no considerations have been made on the crystal quality and surface roughness of the epilayers, which will be discuss in detail later. The slope with which the growth rate increases as a function of the precursor flow is smaller if a plasma discharge power of 1 kW respect to higher plasma power, mainly due to less denser plasma in the growth region. Furthermore, the linear dependence of the growth rate from the gas flow suggest that the deposition process is not reaction limited and the hydrogen desorption process from the growing surface is very efficient. This is also confirmed by the silicon homoepitaxy growth rate characterization which is generally strongly dependent from the hydrogen desorption due to stronger Si – H bond respect to that of germanium, which have a bond energy E_b of 43.3 $kcal \cdot mol^{-1}$ and 37.0 $kcal \cdot mol^{-1}$ respectively [6.4]. In case of our grown samples, a Silicon homoepitaxy have similar growth rate comparing to the Ge/Si heteropitaxial sample for equivalent growth conditions. The correlation between the growth rate and the precursor

gas flow also slight deviate from being linear only for flow above 35 sccm and a plasma glow discharge power P_W of 1.6 kW. This is consistent with experimental observation retrieved in other works [6.5, 6.6], in which is found that for high precursor flow rate the growth rate reach a saturation value mainly due to the inability of the glow discharge to decompose the precursor gas molecules.

On the other hand, an increasing of the plasma glow discharge ignition gas flux entails a reduction of the growth rate. In Fig.(6.3) are plotted the measured growth rate as a function of the Ar flux for different plasma discharge power P_W and precursor gas. Increasing the partial pressure of the neutral species in the plasma infact, the mean electron free path λ diminishes due to a correspondent enhancement of the electron-neutral collision frequency. This process lead to a shifting of the electron energy distribution function $f(E)$ towards lower energy values, which in turn lead to a reduction of the degree of ionization R_i as expressed by Eq.(3.6). Furthermore, the reduction of the growth rate result directly related to both the plasma discharge power and the precursor gas flow. In case the precursor flow is fixed, the reduction of the growth caused by the enhanced Ar flux results higher for lower plasma discharge power. For the Si homoepitaxy using a plasma discharge power $P_W = 1$ kW, an increasing of the Ar flux from give rise to a growth rate reduction of about 35%. In case the plasma discharge power is fixed, the reduction instead is directly proportional to the precursor flow.

On the other hand, the influence of the UHV chamber pressure have been also assessed on the growth rate both for Silicon and Germanium epitaxial deposition processes. In order to assess the influence of the pressure exclusively, the chamber pressure have been modulated by tuning the position of the gate vale, i.e. modulating the pumping capacitance of the turbomulecular pump. For both the cases, the influence have been found negligible in a useful pressure range of 10^{-4} – 10^{-2} mbar. Therefore, the main influence on the growth rate is caused by the increasing of the partial pressure in the region near the wafer surface, which can be generate using the dispersal ring. The UHV chamber has been used to reduce the energy of the ions. In Fig.(6.4) is plotted the energy of the ions as a function of the UHV chamber pressure. As described in Section 3.3, the ion bombarding the wafer surface can induce damage or defect in the Si bulk in case the impact energy is larger than 15 – 20 eV [6.7]. Using the ion energy curve plotted in Fig. (6.4), it can be inferred that a chamber pressure above the value of 10^{-3} mbar is mandatory in order to avoid substrate bulk damages.

6.3 Ge/Si virtual substrates (VSs)

The heteropitaxy of highly mismatched structures involve many physical aspects which influence the growth mode of the epilayer. As described in detail in Section 2.3, the different surface energies between the film and the substrate mainly determines the behavior of the growing film mode. The presence also of the elastic strain inducted by the lattice mismatch f and the kinetic processes involved during non-equilibrium epitaxial growth, cause the growth to deviate from ideal equilibrium conditions. In case of Ge/Si heteroepitaxy, the difference in thermal expansion coefficient α_T between Silicon (2.6 x 10^{-6} °C^{-1}) and Germanium (5.8 x 10^{-6} °C^{-1}) cause the wafer to bend and eventually cracks within the epilayer which can compromise the subsequent overgrowth of electronic devices onto the layer surface. This effect in particular is enhanced in thermally driven CVD epitaxial processes, in which high growth temperature are require in order to overcome the activation energy for precursor scission. Thus development of low temperature epitaxial processes are mandatory, in order to suppress temperature effects and kinetic growth processes and thereby obtain high-quality strain-relaxed epilayers with abrupt interfaces. The high effort in controlling the epi-growth of highly mismatched superlattice structures is justified by the huge potentiality which these structures can offer.

In the field of Silicon – Germanium compounds, one of these potential implications is represented by the creation of high-quality strain-relaxed intermediated Ge layers buffer which can accommodates the lattice mismatch between the underlying silicon substrate and the final epitaxial layer. The idea is to concentrate the MD consequent to plastic strain relaxation within the intermediate Ge epilayer, while suppressing the TDD at the surface. The goal is thus to create a buffer layer which exhibit structural properties closer to a bulk material, acting thus a virtual substrate (VS) for the subsequent film overgrowth. In the last few years. strain-relaxed $Si_{1-x}Ge_x$ VS have been employed into strain-engineered microelectronic devices (HFET, BiCMOS) in order to enhance the electrical transport properties of Si. The most important application for pure Ge VS is represented by a cost-effective integration of III-V alloys with silicon substrate. In the optoelectronics field this would allows for example the integration of complex optoelectronic devices onto single silicon chip enabling system-to-system communication. In the work of Liu *et al.* [6.8] a InAs/GaAs quantum dot laser diode grown monolithically onto a Ge VS, shows performances closer an equivalent homoepitaxial laser diode. On the other hand, this can

enable the integration of high-efficient III-V concentrator solar cell using low-cost silicon substrate for low-end application.

To be effective, the intermediate layer should exhibits several structural properties which can ensure high-quality film overgrowth. First, the buffer VS must be ideally fully strain-relaxed in order to match as closely as possible the lattice spacing of the overgrown film and avoid elastic strain which would eventually result in either plastic relaxation or surface corrugation. Furthermore, the TDD at the surface must be as low as possible in order to avoid the worsening effect of TD minority carrier recombination on the electrical performance of the device. As derived in Section 2.1.1, the electrical transport properties of overgrown GaAs film onto Ge substrate are not sensibly influenced below a threshold value which is a function of dopant concentration of the GaAs layer and generally has a value in the range 10^4 – 10^5 cm^{-2}. Finally, the VS buffer film should exhibit low surface roughness in order to achieve abrupt interface between the buffer layer and the overgrown film. Contrarily, the electron scattering and recombination at the interface can reduce the electrical performances of the overgrown device.

In this work, pure Ge VS buffer layer with thickness as high as 1.5 μm have been developed with very low TDD. The low temperature epitaxy growth enabled by the LEPECVD technique also, allows to reduce the effects of thermal expansion coefficients mismatch between Ge and Si, while maintaining a very high growth rate.

6.3.1 LT seed layer growth

One of most important parameter which have to take into account in order to achieve high quality VS buffer layer is the control of the TDD. As described in Section 2.4, the large lattice mismatch between the Ge and Si, which is about $|f| \cong 4.18\%$, causes in Ge/Si heterostructure an incontrollable plastic strain relaxation, which give rise to a large number of short misfit dislocation that, in turn generate an equivalent density of TD arms. In this case, the TD arms which penetrate through the Ge layer are sessile as the gliding processes along the <111> plane is clogged by other dislocation interaction. For that large mismatched heterostructures so the plastic relaxation mechanism should be induced using particular techniques explained in Section 2.4, which help to avoid uncontrolled dislocation generation. These consist in development of a network of artificially controlled defects which both suppress the generation and favor the glide of the TD arms in order to

yield longer MDs segments at the interface. Among the other techniques employed, the most reliable is the employment of the *seed layer*, i.e. a thin buffer layer grown at low temperature, typically 300 – 370 °C, which has a crystalline structure but an high density of vacancy point defects [6.9]. During the subsequent high temperature (HT) growth, these points defects diffuse and nucleates generating both prismatic dislocation loops which are confined within this layer and do not give rise to TD arms, and also interact with TD by pinning process which avoid the TD to propagate through the epilayer.

Using the LEPECVD technique, the formation and the properties of the Ge *seed layer* have been studied in this work. Several samples have been grown at different temperatures in a range of 250 – 400 °C in order to assess the influence of the substrate temperature on the crystal structure, surface roughness and strain relaxation of the low temperature (LT) buffer layer. The plasma discharge power was kept at $P_W < 500$ W for several reasons. First, the induced temperature rise of the wafer due to ions and electron collisions with the wafer surface are reduced, and thus the temperature is tuned almost exclusively using the radiative heater. Second, as reported by Bauer *et al.* [6.10], high deposition rates cause the layer to transit to amorphous as the temperature is not enough to promote effective surface adatom diffusion. However, the power must be enough to avoid the ICP source to work in capacitive mode. In Fig.(6.5) are presented the AFM surface scan for two samples grown at different temperatures. From the surface of the sample grown at 300°C, it is can be deduced that a 3D SK growth mode has developed. The low temperature is infact not high enough to promote the surface rearrangement and thus a 2D growth. The measured RMS is of 6.4 nm, with a maximum peak to valley value of 30 nm. Furthermore, a slight difference in the surface roughness and pattern have been found between the central and peripheral region of the wafer which show a RMS roughness of 3 nm. This difference is induced by the temperature gradients which have been discussed in chapter 5. As described in section 2.3.2, the combination of adatom flux F in not compensated by a sufficient temperature-induced adatom surface mobility, so the fraction of island which presents a second layer nucleation is high. The island thus do not coalescence but instead start to grow in clusters. As the substrate temperature increases, the adatom mobility also increases and the fraction island with dimension higher respect the critical island dimension R_C diminishes rapidely and the growth thus proceed as FM or 2D. The seed layer growth at higher temperature infact, exhibits a surface roughness which is clearly lower than the previous case.

In Fig.(6.6) is presented the HR-XRD $\theta/2\theta$ scan regarding the (400) symmetric reflection for a LT buffer layer grown at 350 °C. For comparison, the HR-XRD $\theta/2\theta$ scan for a buffer layer grown at the higher temperature of 410 °C are also presented. In the inset is presented the Gaussian fitted function and its related parameters. The experimental measured thickness is of 1514 nm. The out-of-plane lattice constant a_{out} can be calculated using the Bragg diffraction angle of the Ge peak $2\theta_B = 66.01°$ and the wavelength of the CuK_{α_1} peak of $\lambda_{CuK} = 1.540954$ Å

$$a_{out} = \frac{4\lambda}{2\sin\theta_b} = 5.6565 \text{ Å} \tag{6.1}$$

Then using Eq.(2.23) and employing a $a_{bulk} = 5.65785$ Å for Ge then the in-plane lattice constant result

$$a_{||} = \frac{1}{2c_{12}}\left(a_{bulk}(c_{11} + 2c_{12}) - d_{\theta_{400}}c_{11}\right) = 5.6583 \text{ Å} \tag{6.2}$$

As the resulted $a_{||}$ is larger than the a_{bulk} of Ge, then the layer experience a tensile strain. The correspondent relaxation factor R can be calculated employing a $a_{Si} = 5.43105$ Å

$$R = \frac{a_{||} - a_{Si}}{a_{bulk} - a_{Si}} = 100.31\ \% \tag{6.3}$$

The layer thus experience a slight tensile stress. As reported also by [6.11], the arising of a tensile in-plane stress can arise as a consequence of the difference in thermal expansion coefficients between the Ge and Si substrate, and thus this is the result of the accumulated strain energy during the cooling process after the deposition at high temperature. Furthermore, the peak broadening of the instrument results also slight asymmetric and thus it may cause an overstimation of the relaxation factor. The Ge peak can be also deconvoluted as the Eq. (2.27), in which each parameter is investigated. The curve fitting of the Ge peak with a Gaussian function results in a σ which can be used to determine the overall broadening of the sample

$$\beta_m = 2\sqrt{[2\ln 2]}\,\sigma = 872.8 \text{ arcsec} \tag{6.4}$$

First, the instrumental broadening β_d^2 is calculated indirectly by analyzing the Si diffraction peak. Supposing a standard dislocation density $D \approx 100$ cm^{-2} for the Si substrate, $|F_H| = 60$ for the (400) reflection for Si, and using the measured curvature radius of R = 35 m, then the β_d^2 is the only unknown parameter in the Eq.(2.27)

$$\beta_m = 2\sqrt{[2\ln 2]}\,\sigma = 2.75\ x\ 10^{-4}\ rad = \ 56.8\ arcsec \tag{6.5}$$

$$\beta_0 = \frac{2r_e\lambda^2[1+\cos(2\theta_B)]|F_H|}{\pi V\cdot\sin(2\theta_B)} = 2.05\ x\ 10^{-5}\ rad = 4.22\,\text{arcsec} \tag{6.6}$$

$$\beta_\alpha\ \approx \sqrt{(2\pi\ln 2)b^2D} = 8.014\ x\ 10^{-7}\ rad = 0.165\,\text{arcsec} \tag{6.7}$$

$$\beta_\varepsilon\ = \sqrt{0.09b^2D|\ln\left(2\text{x}10^{-7}[cm]\sqrt{\text{D}}\right)|\tan^2\theta_\text{B}}\ = 2.875\ x\ 10^{-7}\ rad \tag{6.8}$$

$$\beta_L\ \approx \sqrt{\left[\frac{4\ln 2}{\pi h^2}\right]\left(\frac{\lambda^2}{\cos^2\theta_B}\right)} = 4.51\ x\ 10^{-7}\ rad \tag{6.9}$$

$$\beta_R\ = \frac{W}{R\sin\theta_B} = 2.63\ x\ 10^{-4}\ rad \tag{6.10}$$

Using Eq.(2.27), the instrumental broadening result of $\beta_d\ = 7.9$ x 10^{-5} rad. Then the other components β_0^2, β_d^2, , β_R^2, and β_L^2 are then calculating using the Eq.(2.31) – (2.32). The measured thickness by means of gravimetric technique is $h = 1514$ nm, and the $|F_H| =$ 146 for Ge (400) reflection

$$\beta_L\ = 1.14x10^{-4}\ rad = 11.75\ arcsec \tag{6.11}$$

$$\beta_0 = 5.237\ x\ 10^{-5}\ rad = 10.80\,\text{arcsec} \tag{6.12}$$

$$\beta_R = 2.73\ x\ 10^{-4}\ rad = 56.31\,\text{arcsec} \tag{6.13}$$

By substituting Eqs.(6.11)-(6.13) into Eq.(2.27), while suing the instrumental broadening component β_d derived analyzing the Si peak, it is possible to derive the value of the unknown parameter $\beta_\alpha^2 + \beta_\varepsilon^2$ which depends on the dislocation density *D*

$$\beta_\alpha^2 + \beta_\varepsilon^2 = K_\alpha + K_\varepsilon \tan^2 \theta_B = 1.7\ x\ 10^{-5}\ rad \tag{6.14}$$

In order to find the two constants K_α and K_ε a set composed of at least two $(h_i k_i l_i)$ / $(h_j k_j l_j)$ rocking curve is mandatory. Otherwise, the K_ε component can be discarded as the $\tan^2 \theta_B = 0{,}422$ is relatively low. Thus, exploiting the K_ε equation expressed as Eq.(2.29), the dislocation density *D* can be derived

$$D = \frac{K_\alpha}{(2\pi \ln 2)\, b^2} = 2.4\ x\ 10^9\ cm^{-2} \tag{6.15}$$

The calculated value results extremely high respect but it worth to say that it have to be intent as the integration of all dislocation present within the epilayer and not a the TDD density at the surface. The incident beam infact penetrate into the heterostructure generally for several μm, and so the broadening of components of measured rocking is the summation of all non-idealities within the penetration depth t_p of the X-ray. This parameter can be expressed infact as the sum of two component, i.e. the extinction coefficient t_{ext} which takes into account the intensity losses due to energy transfer to diffracted beam assuming negligible absorption, and the absorption coefficient t_{abs} which instead take into account the absorption losses assuming negligible extinction coefficient. Both the terms depends on the angle of incidence of the X-ray beam through the cosine director of the incident and exit beam respect to the surface normal, the structure factor $|F_H|$ and the wavelength of the incident beam. Detail description of the two components can be found in Ref. Thus while the t_{abs} give an indication of the maximum penetration depth through the specimen, the extinction coefficient t_{ext} gives the maximum depth at which the diffracted beam is generated. The penetration depth is thus a combination of the two effects

$$t_p = \left(\frac{1}{t_{ext}} + \frac{1}{t_{abs}}\right)^{-1} \tag{6.16}$$

For example, in case of Si (100) symmetric (400) reflection using the CuK_{α_1} the maximum extinction coefficient is $t_{ext} = 34.3\ \mu m$ and the maximum absorption depth of $t_{abs} = 19.8\ \mu m$. Substituting into Eq.(6.16), a penetration depth of $t_p = 12.6\ \mu m$ results. This means that the diffracted beam is influenced by the all the defects encountered in a volume of high equal to the penetration depth t_p.

6.3.2 High temperature (HT) step growth

Once the LT seed layer has been grown, a subsequent overgrowth at higher temperature has been performed. As explained in Section 2.4.2, after the LT step which give rise to a supersaturation of vacancy point defects in the buffer seed layer, a subsequent high temperature (HT) overgrowth has been performed. The temperature rise promote the strain relaxation of the whole epilayer by plastic defect generation. While in a constant temperature epilayer growth the plastic relaxation of a highly mismatched heterostructure result in a uncontrolled generation of sessile MDs which in turn generate a high density of TD arms which penetrate through the film. During this growth step is extremely important to choose right substrate temperature window which can promote relaxation without compromising the surface flatness of the overgrown. In Fig.(6.7) is presented the HR-XRD $\theta/2\theta$ symmetric (400) scan of a sample in which a LT growth at $T_L = 350$ °C and subsequent growth at $T_H = 550$ °C has been performed. The total measured thickness using the gravimetric technique is of 773 nm, while the measured bent radius is 33.38 m. The evaluation of the in-plane lattice constant using Eq.(2.23)-(2.24) and the correspondent relaxation degree *R* result

$$a_{||} = 5.6652\ \text{Å} \tag{6.17}$$

$$R = \frac{a_{||} - a_{Si}}{a_{bulk} - a_{Si}} = 103.37\ \% \tag{6.18}$$

Even in this case the calculation of the in-plane strain reveal a tensile stress instead of a compressive one. In order to check the strain calculation, several asymmetric reflection scan along the (311) and (224) plane have been performed and the in-plane stress is calculated using the Eq.(2.25). In Fig.(6.7) are compared the three XRD rocking curves regard the symmetric (400) reflection, and the (311) and (224) asymmetric reflection in which the angular separation of the Si and Ge peak have been indicated. By coupling the (400) symmetric reflection with the alternatively the two asymmetric reflection, the derived in-plane stress results

$$\Delta\omega_{400} = 5366\,\text{arcsec} \quad , \quad \Delta\omega_{(311)A} = 4585 \qquad \varepsilon_{||} = -6.963\,x\,10^{-3} \tag{6.19}$$

$$\Delta\omega_{400} = 5366\,\text{arcsec} \quad , \quad \Delta\omega_{(224)A} = 8231 \qquad \varepsilon_{||} = -6.58\,x\,10^{-3} \tag{6.20}$$

$$\Delta\omega_{(224)A} = 8231\,\text{arcsec} \quad , \quad \Delta\omega_{(311)A} = 4585 \qquad \varepsilon_{||} = -4.92\,x\,10^{-3} \tag{6.21}$$

The values of in-plane stress calculated using different combinations of asymmetric and symmetric diffraction reflection are in good agreement, with a maximum absolute and relative error between the (400)/(224)A and the (400)/(311)A of $\overline{\Delta\varepsilon_{||}} = 3.8$ x 10^{-4} and $\Delta\varepsilon_{||,r} = 5.7\%$ respectively. Using a mean value of the in-plane stress of 6.15 x 10^{-3}, the degree of relaxation can be calculated as

$$a_{||} = a_{Ge}\left(1 + \varepsilon_{||}\right) = 5.6230\ \text{Å} \tag{6.22}$$

$$R = \frac{a_{||} - a_{Si}}{a_{bulk} - a_{Si}} = 85\ \% \tag{6.23}$$

Using Eq.(2.25) a compressive in-plane stress have been thus found, with an high degree of relaxation. Even for this sample, the evaluation of the dislocation density D through the deconvolution of the XRD rocking curve have been performed. Below are summarized the values of the broadening components and the resulting threading dislocation density

$$\beta_L = 2.23\,x\,10^{-4}\,rad = 45.99\,arcsec \tag{6.24}$$

$$\beta_0 = 5.22\ x\ 10^{-5}\ rad = 10.76\,\text{arcsec} \tag{6.25}$$

$$\beta_R = 1.23\ x\ 10^{-4}\ rad = 25.37\,\text{arcsec} \tag{6.26}$$

$$\beta_\alpha^2 + \beta_\varepsilon^2 = 2.17\ x\ 10^{-5} \quad \rightarrow \quad D = 1.79\ x\ 10^{9}\ cm^{-2} \tag{6.27}$$

As in the previous case, the dislocation density D calculated is extremely high, but this value takes into account also of the dislocation network which is generated by the plastic relaxation of the layer. The evaluation of the TDD at the free surface by means of the EPD technique, results in a threading dislocation density of 3.23 x 10^6 cm^{-2}. The AFM scan of the surface is shown in Fig.(6.8). The measured RMS roughness is about 3.1 nm, with a maximum peak-to-valley of 5 nm. The high temperature thus promoted the strain relaxation that has been evaluated being about 85%, while favoring the TD gliding process and the suppression of the TDD at the epilayer surface. Therefore, the LT-HT steps growth process are thus an effective technique for controlling the plastic relaxation of highly mismatched heterostructures, while offering an reliable and cost effective methods to growth high quality virtual substrates.

However, the quality of the results are strictly tight with the temperature accuracy of the substrate temperature. As reported by Bauer *et al.* [6.10], the process window is infact narrow both for the LT and HT step growths. If the temperature is too low during the LT growth step, the induced density of point defect are so high that the epilayer transient from crystalline to amorphous. Otherwise, if the temperature is too high the epilayer relax the elastic strain though an incontrollable generation of defects, which lead to an high TDD value. Furthermore, over a threshold temperature value, the atoms at the interface have enough energy to overcome the activation barrier for Ge -Si interdiffusion. The result is the generation of a SiGe layer with random composition, which help to relieve the mismatch-induced elastic strain, while having however a worsening effect on the surface roughness of the epilayer. In Fig. (6.9) are presented two (400) symmetric rocking curves of two samples grown at 570 °C and 600°C respectively. The generation of an intermediate diffraction peak between the Ge and Si suggest the generation of the intermediate SiGe layer. The Bragg angle of the peak has been evaluated as $2\theta_B = 67.59°$. Assuming a negligible in-plane strain for this layer, the composition of the SiGe alloy can be derived employing the Eq.(2.0) relation between the lattice constant and the alloy composition

$$a_{SiGe} = \frac{4\lambda}{2\sin\theta_b} = 5.5408\text{Å} \tag{6.28}$$

$$x = 0.48 \tag{6.29}$$

The comparison between the two XRD rocking curve show that an abrupt threshold exist for the activation of the Ge-Si interdiffusion, as the two samples have been grown with a temperature difference of about 30°C. The rocking curve for the sample grown at 600°C shows a drastic reduction of the intensity of the diffraction peak, while it can be still nearly visible.

Pure Germanium virtual substrate (VSs) buffer layer have been growth using the LEPECVD technique. The reactor developed at the University of Ferrara, have been proved allowing high quality epitaxial growth, while maintaining an outstanding growth rate over the temperature range useful for the Si and Ge epitaxial deposition. The grown Ge epilayers shows an high degree of relaxation and TDD as low as $8.3\text{x}10^{-5}$ cm^{-2}, while an surface RMS roughness of less than 3 nm at thickness up to 2 μm. This put the basis for a real cost-effective integration of the III-V compounds onto a low cost silicon wafers.

References

[6.1] C. Rosenblad, H.R. Deller, T. Graf, E. M*ü*ller, H. von Kaenel, *J. Crystal Growth,* **vol.** 188 (1998), pp. 125-130

[6.2] C. Rosenblad, T. Graf, J. Stangl, Y. Zhuang, G. Bauer, J. Schulze, H. von Kaenel, *Thin Solid Films,* **vol.** 336 (1998), pp. 89-91

[6.3] D. Chrastina, G. Isella, B. R[o]ssner, M. Bollani, E. M*ü*ller, T. Kackbarth, H. von Kaenel, *Thin Solid Films,* **vol.** 459 (2004), pp. 37-40

[6.4] J.M. Hartmann, V. Loup, G. Rolland, P. Hollinger, F. Laugier, C. Vannufel, M.N. Semeria, *J. Crystal Growth,* **vol.** 236 (2002), p. 10

[6.5] O.O. Olubuyide, D.T. Danielson, L.C. Kimerling, J.L. Hoyt, *Thin Solid Films,* **vol.** 508 (2006), pp. 14-19

[6.6] G. Pin, O. Kermarrec, G. Chabanne, Y. Campidelli, J.-B. Chevrier, T. Billon, D. Bensahel, *J. Crystal Growth,* **vol.** 286 (2006), pp. 11-17

[6.8] Y. Chen, J.W. MacKay, *Phil. Mag.,* **vol.** 19 (1969), p. 357

[6.8] H. Liu, T. Wang, Q. Jiang, R. Hogg, F. Tutu, F. Pozzi, A. Seeds, *Nature Photonics,* **vol.** 5 (2011), pp. 416-419

[6.9] K. Lyutovich, E. Kasper, F. Ernst, M. Bauer, M. Oehme, *Mat. Sci. Engin. B*, **vol.** 71 (2000), pp. 14-19

[6.10] M. Bauer, K. Lyutovich, M. Oheme, E. Kasper, H.-J. Herzog, F. Ernst, *Thin Solid Films,* **vol.** 369 (2000), pp. 152-156

[6.11] J.E. Ayers, *Heteropitaxy of Semiconductors. Theory, Growth and Characterization,* CRC Press, 2007

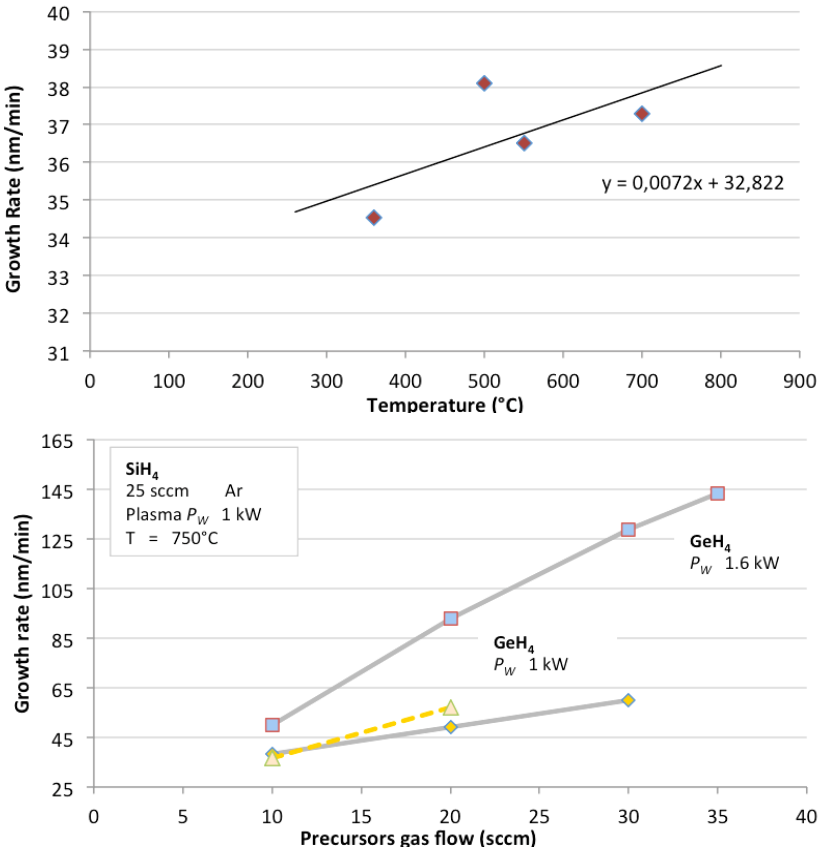

Fig. 6.1 (*a*). Growth rate using GeH_4 as a function of the substrate temperature (*b*). Growth rate for SiH_4 and GeH_4 as a function of the plasma discharge power $\boldsymbol{P_W}$. (*Courtesy of Dichroic Cell* ®)

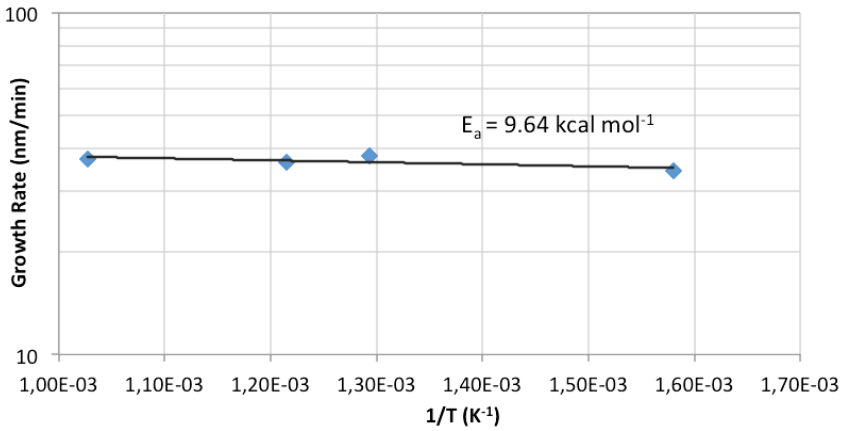

Fig. 6.2 Arrhenius plot of the growth rate for Ge/Si heteroepitaxy using LEPECVD reactor. The derived activation energy $\boldsymbol{E_a}$ suggest that the deposition process is diffusion limited. (*Courtesy of Dichroic Cell* ®)

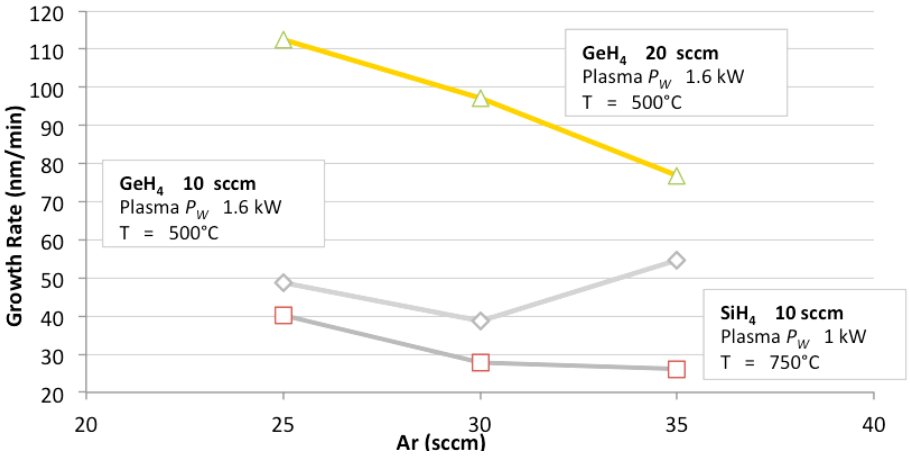

Fig. 6.3 Growth rate for Ge/Si heteropitaxy as a function of the Ar flux. (*Courtesy of Dichroic Cell* ®)

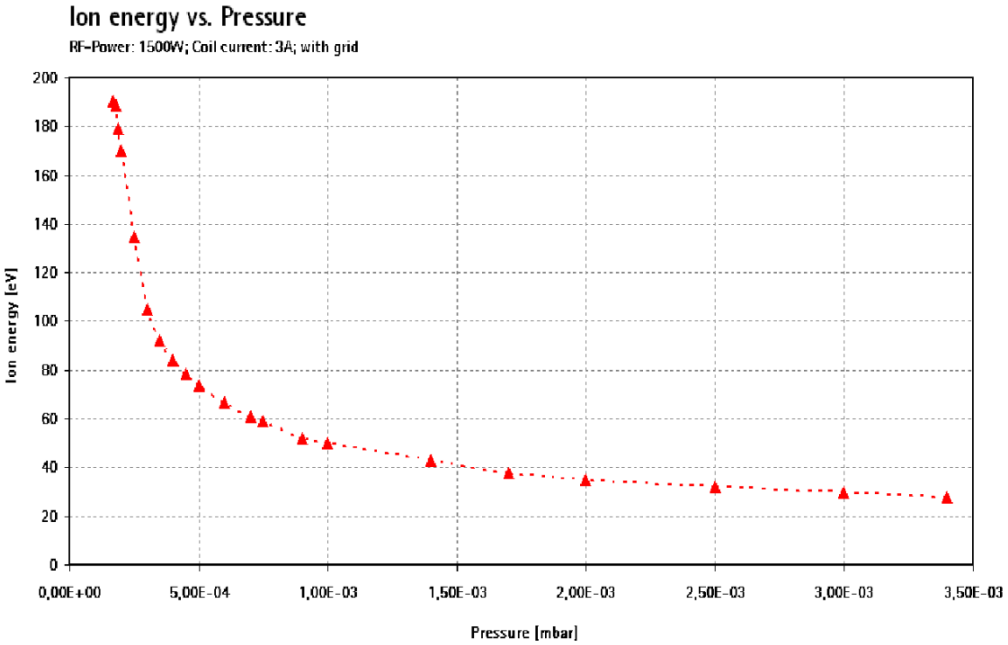

Fig. 6.4 The ion energy for an ICP plasma glow discharge as a function of the pressure

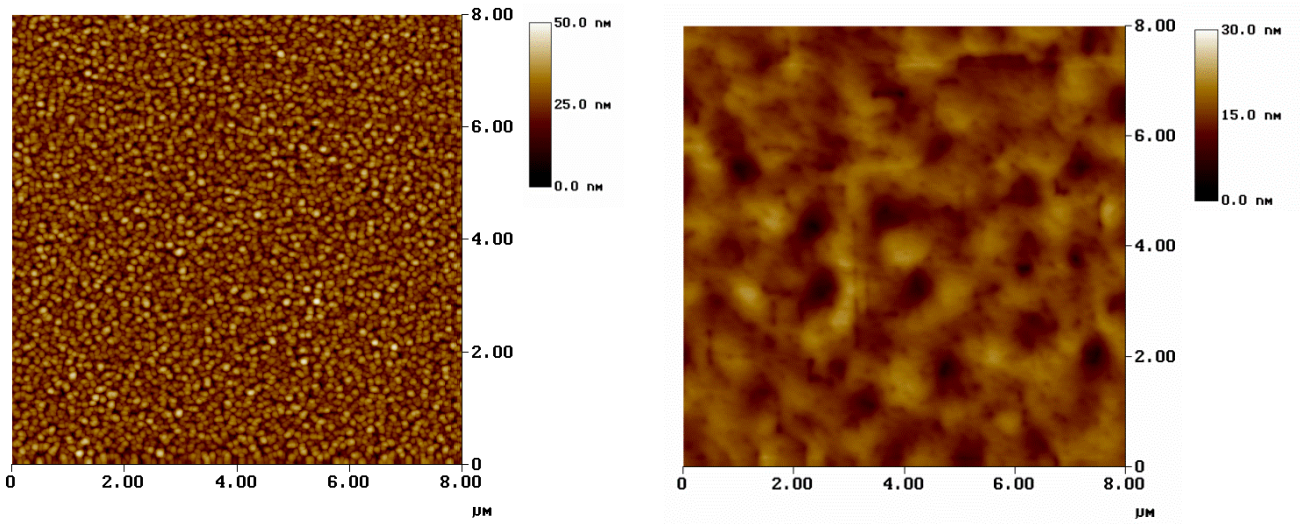

Fig. 6.5 AFM 8 x 8 $\boldsymbol{\mu m^2}$ scan images for LT buffer layers grown at 300 °C (*left)* and 550°C (*right*). (*Courtesy of Dichroic Cell* ®)

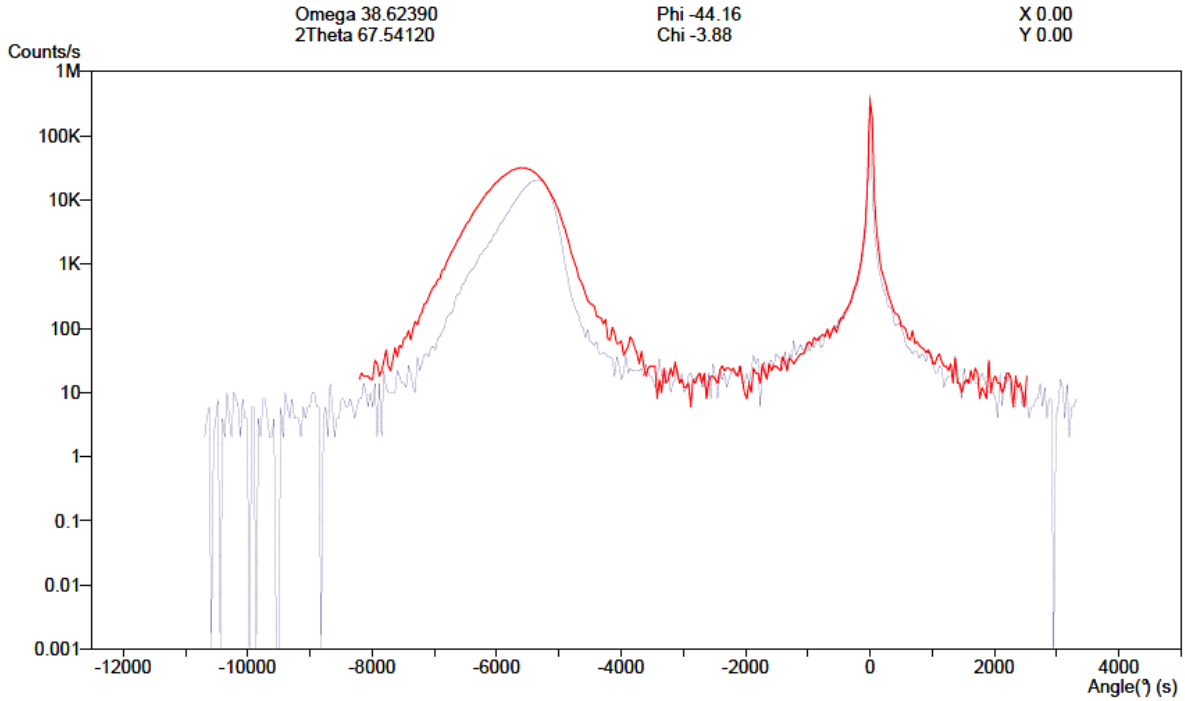

Fig. 6.6 HR-XRD $\boldsymbol{\theta/2\theta}$ scans of the (400) reflection for two samples grown at 350°C (*black*) and 410°C (*red*). (*Courtesy of Dichroic Cell* ®)

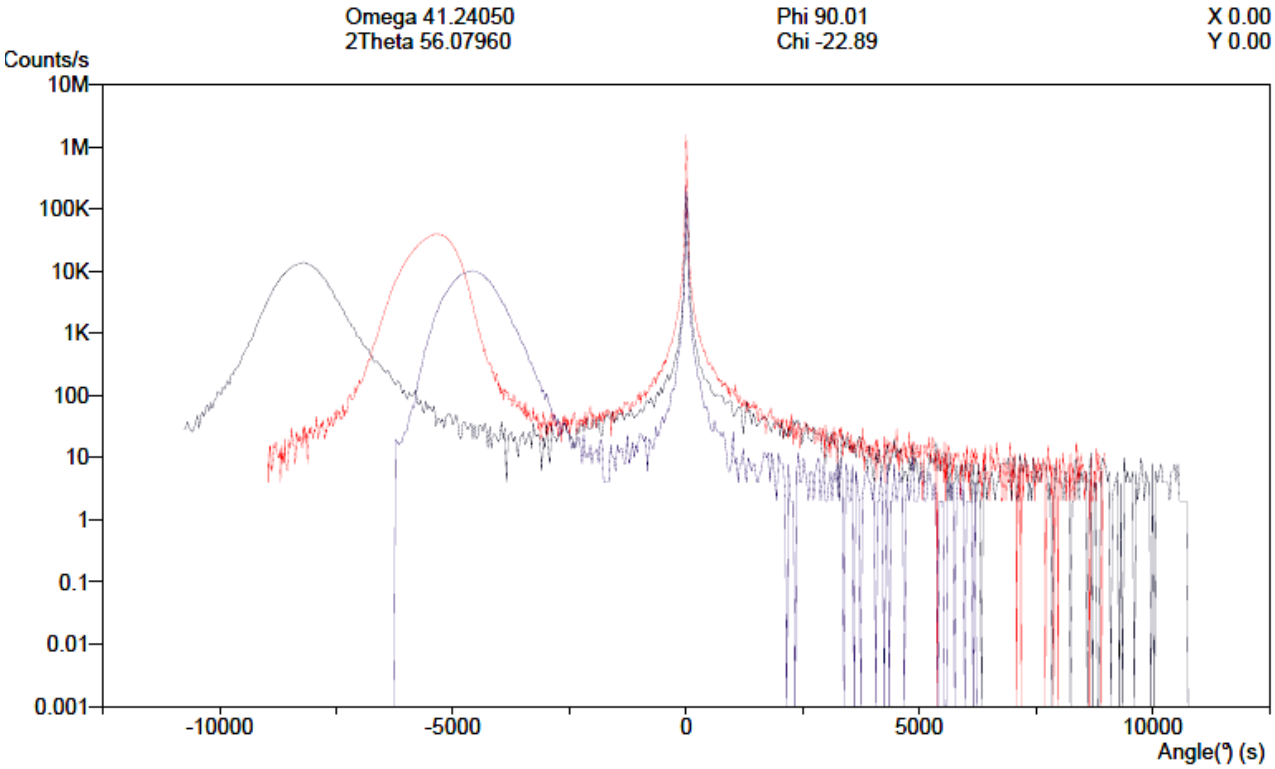

Fig. 6.7 HR-XRD $\boldsymbol{\theta/2\theta}$ scans of sample in which the two step LT-HT grown has been performed. The (400) reflections are plotted with red line, while the (311) and (224) asymmetric scan are represented by the blue and black line respectively. (*Courtesy of Dichroic Cell* ®)

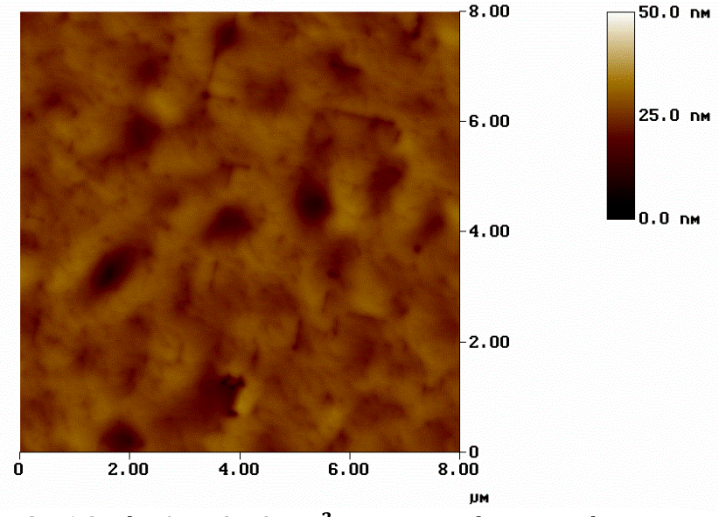

Fig. 6.8 The AFM 8 x 8 $\boldsymbol{\mu m^2}$ scan image for a sample grown with the LT-HT step processes. (*Courtesy of Dichroic Cell* ®)

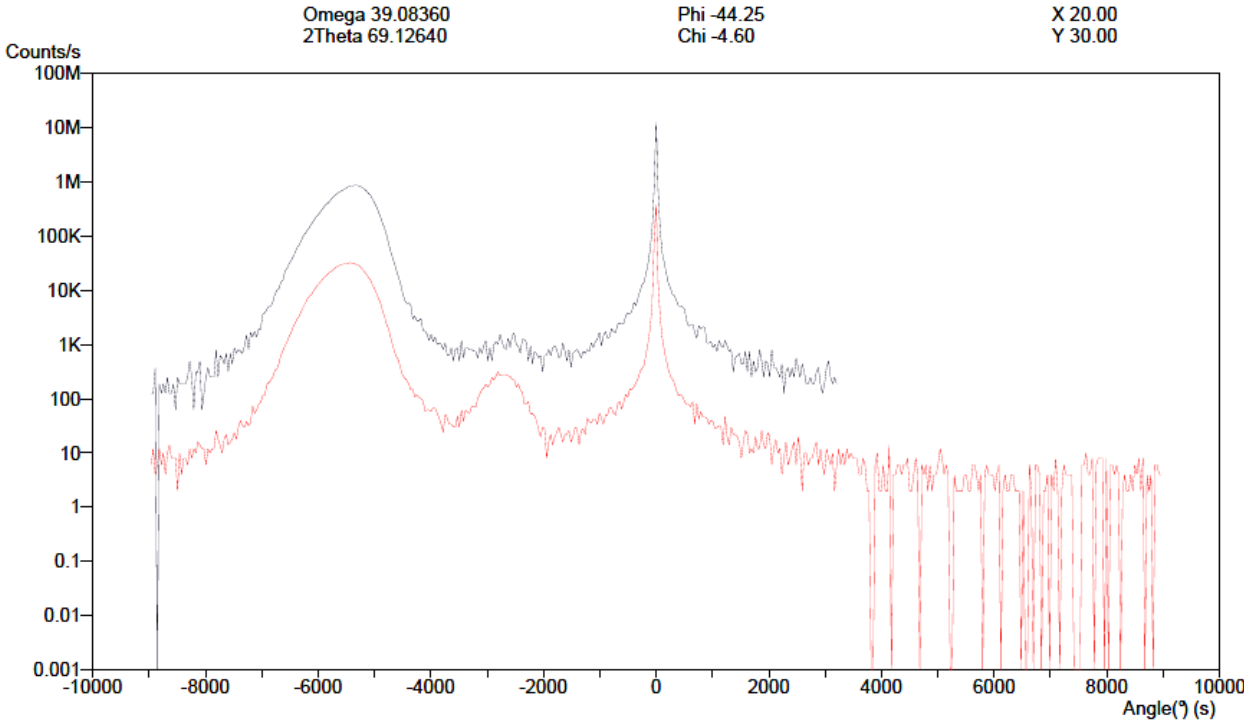

Fig. 6.9 HR-XRD $\boldsymbol{\theta/2\theta}$ scans of the (400) reflection for two samples in which the HT growth step has been performed at 600°C (red) and 570°C (black). (*Courtesy of Dichroic Cell* ®)

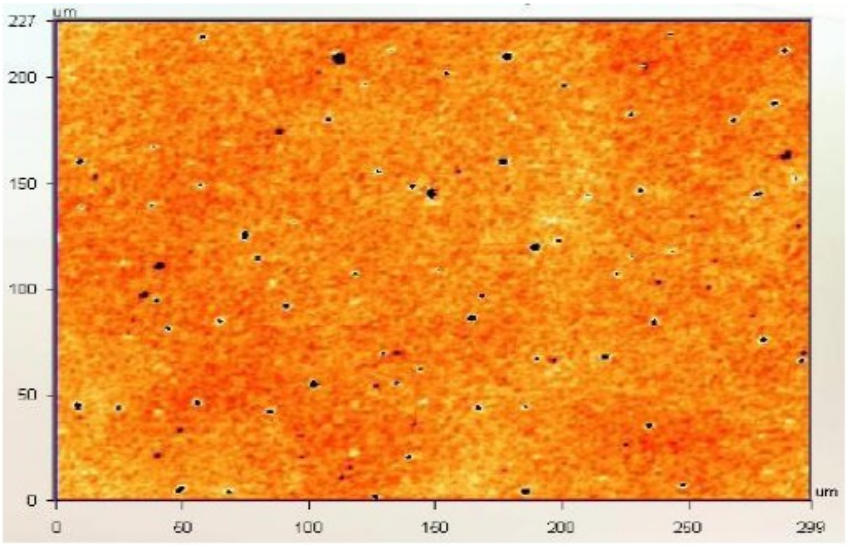

Fig. 6.10 SEM image scan for EDP measurements. The sample shows a TDD density of 3.1 x 10^5 cm^{-2}. (*Courtesy of Dichroic Cell* ®)

Conclusions

The epitaxial deposition processes of Silicon and Germanium using the innovative LEPECVD reactor have been investigated in this work. The reactor have been developed at the Physics Department of the University of Ferrara in collaboration with Dichroic Cell S.r.l. The reactor comprise of several innovative features comparing to the state-of-art deposition techniques which are subject of patent pending applications by Dichroic Cell S.r.l. The present technique enable infact high growth rate deposition even for low substrate temperature, while yielding to high quality epilayers. In particular, the employment of a ICP plasma source have been proved to solve many issue which arise if DC-arc glow discharges or capacitively coupled plasma (CCPs) sources are used. Comparing to other plasma technique infact, it is possible to increase the power of the glow discharge while maintaining the ions energy below the threshold value of 15 -20 eV above which bulk damages can be generated in the substrate by surface ion bombardment. Furthermore, an optimization of the reactor design have caused the growth rate to increase at values as high as 3 nm/s.

The critical aspect of the substrate temperature have been also investigated by finite element technique. During epitaxial depositions infact the temperature of the wafer influence several adatom mechanisms such as surface mobility or the hydrogen desorption. The radiative heating stage employed in the LEPECVD reactor have been thus modeled and simulated using the commercially available ADINA 8.7 software. Numerical results have been also validated using pyrometric and instrumented wafer experimental measurement. The results show that the wafer surface suffers of a temperature gradient of about 50°C from the center to the edge of the substrate maily due to radiative unevenness emission of the graphite element. The key aspects for design improvement

have been thus identified and analyzed for further design improvements. The influence of the different radiative properties of the substrate on the thermal behavior of the heating stage have been also studied.

Finally, several Silicon – Germanium hetero and homoepitaxial structures have been developed onto using LEPECVD technique. In particular, the deposition of strain-relaxed Ge virtual substrate (VSs) have been studied in this work. The employment of two step growth technique (LT – HT step growth) have proved to promote controlled strain relaxation of the layer while suppressing the generation of threading dislocation (TDs) defects which influence negatively the electric properties of the epilayers. The films grown show a TDD as low as 10^5 cm^{-2} and a relaxation degree which approach to 100%. These results combine combine to a low surface roughness lay the foundation for a real cost-effective integration of high efficient III-V alloys with a low cost silicon substrate.